

JAGIELLONIAN UNIVERSITY

DOCTORAL THESIS

**Biomedical applications of Positron
Annihilation Lifetime Spectroscopy:
nanostructural characterization of normal
and cancer cells and tissues**

Author:

Ewelina KUBICZ

Supervisor:

Prof. Paweł MOSKAL,

Prof. Ewa STĘPIEŃ

*A thesis submitted in fulfilment of the requirements
for the degree of Doctor of Philosophy in the*

Faculty of Physics, Astronomy and Applied Computer Science

July 15, 2020

Declaration

Wydział Fizyki, Astronomii i Informatyki Stosowanej
Uniwersytet Jagielloński

Oświadczenie

Ja niżej podpisana, Ewelina KUBICZ (nr indeksu: 1051798), doktorantka Wydziału Fizyki, Astronomii i Informatyki Stosowanej Uniwersytetu Jagiellońskiego oświadczam, że przedłożona przeze mnie rozprawa doktorska pt. *“Biomedical applications of Positron Annihilation Lifetime Spectroscopy: nanostructural characterization of normal and cancer cells and tissues”* jest oryginalna i przedstawia wyniki badań wykonanych przeze mnie osobiście, pod kierunkiem Prof. dr hab. Pawła Moskała oraz Dr hab. Ewy Stępień, prof. UJ. Pracę napisałam samodzielnie.

Oświadczam, że moja rozprawa doktorska została opracowana zgodnie z Ustawą o prawie autorskim i prawach pokrewnych z dnia 4 lutego 1994 r. (Dziennik Ustaw 1994 nr 24 poz. 83 wraz z późniejszymi zmianami).

Jestem świadoma, że niezgodność niniejszego oświadczenia z prawdą ujawniona w dowolnym czasie, niezależnie od skutków prawnych wynikających z ww. ustawy, może spowodować unieważnienie stopnia nabytego na podstawie tej rozprawy.

Podpis:

Kraków, dnia:

“Somewhere, something incredible is waiting to be known.”

Carl Sagan

“Ignorance more frequently begets confidence than does knowledge: it is those who know little, not those who know much, who so positively assert that this or that problem will never be solved by science.”

Charles Darwin

JAGIELLONIAN UNIVERSITY

ABSTRACT

Biomedical applications of Positron Annihilation Lifetime Spectroscopy: nanostructural characterization of normal and cancer cells and tissues

EWELINA KUBICZ

This thesis is devoted to examining a possible biomedical application of Positron Annihilation Lifetime Spectroscopy (PALS), for the characterisation of normal and cancer cells and tissues. PALS allows to study molecular structure at the nano- and subnanometer levels, by measurement of positronium properties in intra-molecular voids.

Studies conducted in the framework of this thesis aim to test the research hypothesis that positronium can be used as a novel biomarker for cancer diagnostics. The working hypothesis assumes that cancer cells differ from normal ones, in their nanostructure and molecular interactions. These changes are significant enough to affect positronium properties to a degree observable with the PALS technique. Correlations between the cellular organisation, its relation to the cell morphology and signalling with positronium are examined in connection with positronium properties to carcinogenesis and metastatic processes.

The proposed hypothesis is tested in two models: benign cardiac myxoma specimens and malignant melanoma cultured cell lines. In both cases, positronium properties are compared to an appropriate normal tissue and cell line. Studies are performed for both fixed and living cells and tissues to investigate the influence of water and cell viability on the PALS signal.

Obtained results show significant differences in positronium lifetime and its production intensity between cancer and normal cells and tissues in all studied cases, regardless of hydration and fixation of specimens. Therefore, obtained results validate the working hypothesis that positronium can be applied as a novel biomarker in cancer diagnostics.

UNIWERSYTET JAGIELLOŃSKI

STRESZCZENIE

Biomedyczne aplikacje spektroskopii czasów życia pozytonów: charakterystyka nanostruktury prawidłowych i nowotworowych komórek i tkanek

EWELINA KUBICZ

Prezentowana praca doktorska poświęcona jest badaniu zastosowań biomedycznych spektroskopii czasów życia pozytonów (PALS) w celu charakterystyki normalnych i nowotworowych komórek i tkanek. Technika ta pozwala badać strukturę molekularną na poziomie nano- i subnanometrowym, poprzez wykorzystanie właściwości pułapkowania pozytonium w przestrzeniach międzycząsteczkowych.

Badania przeprowadzone w ramach tej pracy, mają na celu zweryfikowanie perspektywy zastosowania pozytonium jako nowego biomarkera w diagnostyce nowotworów. Hipoteza badawcza zakłada, że komórki nowotworowe różnią się w swojej nanostrukturze od komórek prawidłowych, oraz że zmiany te wpływają na właściwości pozytonium w stopniu możliwym do zaobserwowania za pomocą techniki PALS. Badane są korelacje pomiędzy organizacją komórkową, a jej związkiem z morfologią komórki i sygnalizacją za pomocą pozytonium, w kontekście związku właściwości pozytonium z procesem nowotworzenia i powstawaniem przerzutów.

Proponowana hipoteza jest testowana na dwóch modelach: śluzaka serca jako łagodnego guza oraz hodowli linii komórkowych czerniaka jako przykład złośliwego nowotworu. W obu przypadkach właściwości pozytonium porównuje się z odpowiednią prawidłową tkanką i linią komórkową. Przeprowadzane są pomiary zarówno dla utrwalonych, jak i żywych komórek i tkanek, w celu zbadania wpływu wody oraz żywotności komórek na sygnał PALS.

Uzyskane wyniki wskazują na znaczące różnice w czasie życia i intensywności produkcji pozytonium pomiędzy nowotworowymi a normalnymi komórkami i tkankami we wszystkich badanych przypadkach, niezależnie od uwodnienia, czy utrwalenia próbek. Uzyskane wyniki pozwalają na potwierdzenie hipotezy badawczej, że pozytonium można zastosować jako nowy biomarker w diagnostyce nowotworów.

Acknowledgements

I want to express my highest gratitude to all people without whom completing this thesis would not have been possible.

First and foremost, I thank Prof. Paweł Moskal for the opportunity to work in his research group, valuable help, lots of hints and suggestions, but above all for understanding, enormous patience and support in my all academic endeavours. I am also greatly indebted to Prof. Ewa Stępień for her guidance in the biomedical studies, patience, help and lots of tips and tricks during all my experiments. To both my supervisors, I wanted to thank for correcting this manuscript and me, whenever I was wrong, and for simply explaining the most complex things.

I also thank my Colleagues from the J-PET collaboration for a friendly atmosphere, many great and not only scientific advice. Many thanks are to dr Aleksander Gajos, dr Daria Kisielewska, dr Grzegorz Korcyl and dr Michał Silarski for help in setting up the detectors and data acquisition systems. Mostly, I would like to offer my gratitude to Kamil Dulski for his support in experiments, analysis and corrections of this thesis. I could always count on your factual and relevant comments. Thank you.

Special thanks to my Colleagues: Anna Drożdż, dr Agnieszka Kamińska and Monika Szczepanek for the scientific contribution, lots of help in the lab and the great time spend together.

I am sincerely grateful to Prof. Hubert Harańczyk and Karol Kubat for the opportunity of conducting NMR studies and help with them. I also wish to thank Prof. Martyna Elas, dr Anna Kozińska and Krystian Mokrzyński for the possibility of performing EPR studies and many helpful suggestions.

I would also like to extend my enormous gratitude to Prof. Józef K. Mościcki for his guidance, help, invaluable advice and constant motivation since the early beginning of my studies.

A huge thank you, to all and each of my friends, for lots of fun, great time spent together, but mostly for patient and support. Without you, my life would be so ordinary and boring. Special thanks to Ania for help and corrections to this manuscript, as it usually is for me, at the last minute.

Here I especially want to thank Bartek for love, support, cheerfulness and constant motivation to finish this thesis. It would go on for the next 'million years' without you.

Dziękuję także moim Rodzicom, Kamilowi, Michałowi i Oli za pomoc, wyrozumiałość, ogrom cierpliwości, a przede wszystkim, że zawsze mogłam na was liczyć.

Pracę tę dedykuję mojej Mamie. Dziękuję Ci Mamo, że zawsze we mnie wierzyłaś.

This work was supported by the Polish National Science Centre through grant no. 2017/25/N/NZ1/00861, and by the Foundation for Polish Science through the TEAM POIR.04.04.00-00-4204/17 programme.

Contents

Declaration	i
Abstract	iii
Streszczenie	iv
Acknowledgements	v
1 Introduction	1
I Theoretical Background	4
2 Positron Annihilation Lifetime Spectroscopy	5
2.1 Positronium	5
2.2 Positronium Annihilation	7
2.3 Tao-Eldrup Model	9
3 Carcinogenesis	11
3.1 Cancer - its origin and development	11
3.2 Differences between normal and cancer cells	16
3.3 Melanocytes and melanoma	17
3.4 Cardiac Myxoma	20
II Material and Methods	22
4 PALS technique	23
4.1 Source of positron	23
4.2 PAL spectrometer	24

4.3	Holder and chambers for biological samples	25
4.4	Data analysis	27
4.4.1	Amplitude and charge calculation	27
4.4.2	Lifetime distribution	30
4.4.3	Positronium mean lifetime estimation	31
4.5	Setup optimization and calibration	32
4.5.1	Gain calibration	33
4.5.2	Time resolution determination	37
5	Preparation and characterisation of cell lines and tissue	39
5.1	Tissue specimens	39
5.1.1	Study group	39
5.1.2	PALS - tissue preparation	39
5.2	Cell lines	41
5.3	Cell culture	42
5.3.1	WM115 and WM266-4	42
5.3.2	HEMa-LP	43
5.3.3	Cardiac Myxoma	43
5.4	Cell lines preparation for PALS	44
5.4.1	Freeze-drying	44
5.4.2	Rehydration	46
5.4.3	Living cells preparation	46
5.5	Optical and confocal microscopy	47
5.6	Nuclear Magnetic Resonance	49
5.7	Electron Paramagnetic Resonance	49
III	Experimental Results	52
6	Cardiac Myxoma	53
6.1	Clinical characteristics of study group	53
6.2	Fixed tissues studies	56
6.3	Comparison of cardiac myxoma vs normal tissue	58
6.4	Cardiac Myxoma cell culture	61

7 Melanocytes and melanoma cell culture	66
7.1 Freeze-dried cells	66
7.1.1 PALS	66
7.1.2 Rehydration	70
7.1.3 NMR - cells hydration	72
7.2 Living cells measurements	75
7.2.1 Cell culture and viability	75
7.2.2 PALS experiment	77
7.2.3 EPR - melanin concentration	82
IV Discussion	84
8 Discussion	85
8.1 Cardiac myxoma	85
8.2 Melanoma and melanocytes	88
8.2.1 Freeze-dried cells - the influence of water on positronium life- time	88
8.2.2 Positronium biomarker in living cells	90
9 Conclusions	92
Bibliography	94

List of Abbreviations

CM	cardiac myxoma
DMSO	dimethylsulfoxide
DNA	deoxyribonucleic acid
ECHO	echocardiography
FBS	fetal bovine serum
HBV	hepatitis B virus
HCV	hepatitis C virus
HPV	human papilloma virus
IL-6	interleukin 6
KGF	keratinocyte growth factor
L-DOPA	dihydroxyphenylalanine
o-Ps	ortho-Positronium
PALS	positron annihilation lifetime spectroscopy
PBS	phosphate buffer saline
PDGF	platelet-derived growth factor
PMT	photomultiplier
p-Ps	para-Positronium
Ps	positronium atom
PRKAR1A	cAMP-dependent protein kinase type I-alpha regulatory subunit
pRb	retinoblastoma protein
PROH	1,2 -propanediol
ROS	reactive oxygen species
TNF-α	tumour necrosis factor α

Chapter 1

Introduction

Positron Annihilation Lifetime Spectroscopy (PALS) is a technique, which allows studying matter at nano and sub-nanometer levels until recently used mostly in material studies, while its potential in the biomedical application was not thoroughly employed and researched. Studies presented in this thesis explored the possibility for application of positronium as a new biomarker in cancer diagnostics [1, 2]. Only a few works are demonstrating the application of PALS technique to study biological specimens. Jean and his group studied healthy and abnormal skin samples and observed that o-Ps lifetime is correlated with the level of skin damage. Both intensity and lifetime of o-Ps were found to be significantly lower in samples with basal cell carcinoma (BCC) and squamous cell carcinoma (SCC) than in normal skin samples. These studies were performed on fixed samples, as well as in ambient conditions [3–7]. Some differences in PALS parameters between normal and cancerous uterus tissues were also observed by Jasińska et al. [8, 9].

Next example of PALS application in studies of cell culture is the paper by Axpe et al. [10], where authors employed well defined colorectal cancer cell lines grown in the 3D matrix. Axpe et al. showed that the presence of transforming growth factor beta (TGF- β) induces changes at the atomic scale in the size of the free voids, due to the biological effects. These studies were carried out at 4°C and directed the new perspective to use PALS for living cells research. In addition, positron spectroscopy was used to study biopolymers like collagen [11] and cross-linked glucose-gelatin compound [12] - where the effects of swelling, which is also observed in cancer cells, are shown. Investigations of bio-membranes [13] and self-assembled bio-mimetic system [14] have shown that PALS can be used to study membrane dynamics, diffusion

and permeability at the nanoscale. To investigate the influence of water molecules on positronium lifetime, studies on model unicellular micro-organisms *Saccharomyces cerevisiae* were conducted. These studies allowed to observe dynamics of the water adsorption by a hydrophilic material – freeze-dried yeasts [15]. Results proved that PALS could be applied in studies of hydrated biological samples, though water gives a strong signal in this technique. Each of the aforementioned studies shows a possibility to apply PALS in biomedical research. However, the prospect of using positronium as a new biomarker in cancer diagnostics needs to be explored.

The working hypothesis investigated in this thesis assumes that, cancer cells differ in their sub-nanostructure and molecular interactions from normal and that these changes affect positronium properties to a degree observable with the PALS technique. Correlations between the cellular organisation and its relation to the cell morphology and signalling with positronium are examined, in view of the relation of positronium properties to carcinogenesis and metastatic processes.

Cells and tissues are very complex in their structure. The leading research in cell biology and biophysics aims to explain and understand how living processes, occurring on the cellular level are modulated in different spatial and temporal domains. The main challenge in these studies is that the living organisms are built of different molecular and cellular structures and chemical compounds, which function depend on many environmental and intracellular factors. Multiple studies were carried out in the macro and micro spatial distribution, but there were only a few of them that investigate the regulation of cellular processes in the context of changes at the nano- and sub-nanometer scale of the living objects.

This research brings advanced ideas from structural biology and biophysics together. The proposed investigations are unique and pioneering in many aspects, using a relatively new method (PALS) in biomedical applications for studies of biological specimens, like cells and tissues, in the determination of changes of biomechanical structure on the nanometer level. Such detailed research in this area has not been conducted so far.

Applying positronium as a novel biomarker has even more significant potential in cancer diagnostics by combining PET imaging and PALS investigations. Such imaging can be performed simultaneously with the Jagiellonian - Positron Emission

Tomograph (J-PET), which is a multi-purpose detector developed at the Jagiellonian University for investigations with positronium atoms in life-sciences, as well as for the development of medical diagnostics [16–21]. J-PET scanner is capable of imaging of properties of positronium produced inside the human body [2, 22–26].

This thesis is divided into nine chapters, in next two theoretical background regarding the Positron Annihilation Lifetime Spectroscopy and the carcinogenesis is described. Materials and methods applied for PALS measurement and setup calibration are presented in Chapter 4. In Chapter 5, a detailed description of cell culture, specimens preparation, as well as microscopic and spectroscopic techniques applied are featured. Chapter 6 is devoted to the results of the experiment with studied exemplary benign tumour - cardiac myxoma and contains obtained results for positronium parameters in both tumorous and normal tissues. In Chapter 7, the results of studies with cancer cell lines of cutaneous melanoma and normal cell line - melanocytes are presented. Chapter 8 contains a detailed discussion of all obtained results, and in Chapter 9 conclusion are included.

Part I

Theoretical Background

Chapter 2

Positron Annihilation Lifetime Spectroscopy

2.1 Positronium

Positronium (Ps) is a hydrogen-like atom and, at the same time, anti-atom. It is a bound state of an electron and its anti-particle positron.

Positrons are produced during several reactions for example: β^+ decay, $e^- - e^+$ pair production *via* electromagnetic interactions or muon decay [27]. In case of Positron Annihilation Lifetime Spectroscopy radioactive isotopes decaying via β^+ (Eq. 2.1) are used as a source of positrons.



where: A - mass number, Z - atomic number of the decaying nucleus, X - initial element, Y - final element, e^+ - positron, ν_e - neutrino.

The interpretation of biological results will be supported by existing models describing positron behaviour in the dense media, like spur model and its newer version - 'blob model' [28]. Positron, after its production in medium, loses its kinetic energy due to ionization and excitation of material molecules. As a result of these interactions, spherical ionization blobs are formed. With the increase in the probability of scattering of rapidly losing energy positron, the ionization path between blobs decreases until they will start to overlap, forming a cylindrical ionization column. When the positron energy decreases to less than 1 keV final terminal blob is created. Inside it, positron interacts *via* elastic scattering and the ionization of surrounding

molecules. Finally thermalized, positron can create a quasi-stable bound state with one of the intrablob electrons (e^-), so-called positronium (Ps) [29,30]. This thermalization process takes around 10 ps [31]. Schematic view of positronium formation in the blob model is presented in Fig. 2.1.

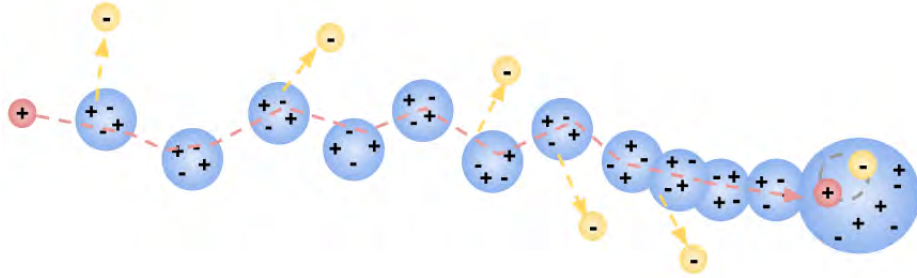


FIGURE 2.1: Schematic view of positronium formation in the blob model.

Positronium is an unstable hydrogen-like atom in which an electron and a positron orbit around a common centre of mass. The radius of positronium is twice the Bohr radius of hydrogen and is equal to 0.106 nm [32]. Its reduced mass is equal to half the mass of the reduced hydrogen atom. Therefore, the binding energy of the positronium atom is twice lower, than the binding energy of the hydrogen and equals to:

$$E_n(Ps) = -\frac{6.8}{n^2} eV, \quad (2.2)$$

where: n - denotes the principal quantum number of the positronium atom energy level.

Positronium can only be created in areas with low or zero electron density, so-called 'free volumes' or 'voids'. Therefore, it is unlikely to be created in dense materials, like metals. While the size of the electron-free space between molecules in some materials are tens and hundred thousand times larger, than the volume of positronium, thus in such substances positronium atoms can be produced. In fact, PALS technique allows observing structures down to the fraction of about 0.2 nm, which is limited by the size of the positronium atom [33].

Depending on the total spin, positronium can occur in two states. In a single state with total spin equal to zero as para-Positronium (p-Ps) or in triplet state with total spin equal to one as ortho-Positronium (o-Ps). Based on the spin statistic, the

probability for o-Ps creation is three times higher than for p-Ps. These states differ in mean lifetime and number of gamma quanta produced during its decay. p-Ps with a mean lifetime in vacuum equal to $\tau_{p-Ps} = 0.125$ ns decays into even number of gamma quanta, most probably two, each with the energy of 511 keV. While o-Ps is characterized by mean lifetime in a vacuum of $\tau_{o-Ps} = 142$ ns and decaying into an odd number of gamma quanta, three or more, while decay into three is the most probable [34].

Positronium can also be created in liquids such as water, which allows studying living cells and other biological specimens. In the spaces between molecules the lifetime of o-Ps decreases to a few nanoseconds. The average lifetime of o-Ps in pure liquid water amounts to about 1.8 ns [35]. Shortening of its lifetime, when embedded in the matter, can be used for studies of nanomorphology of cells and tissue.

2.2 Positronium Annihilation

Annihilation of positron and positronium can occur *via* different processes depending on surrounding matter, such as [36]:

- Intrinsic decay,
- Pick-off process,
- Ortho - para conversion,
- Positron direct annihilation.

In a vacuum, positronium decays intrinsically, where positron and electron in positronium atom annihilate with each other. Due to the parity conservation, positronium annihilates with the emission of even and odd number of gamma quanta for para- and ortho-Positronium, respectively. In Fig. 2.2 schematic view of positronium intrinsic decay is presented.

However, in the matter, the o-Ps mean lifetime can be shortened, due to 'pick-off' process, where positron annihilates with an electron from surrounding molecules. Mostly with the production of two gamma quanta with the energy of 511 keV each. Probability of this process increases with the decrease of the size of free volumes in between the molecules. Due to this process mean lifetime of positronium can

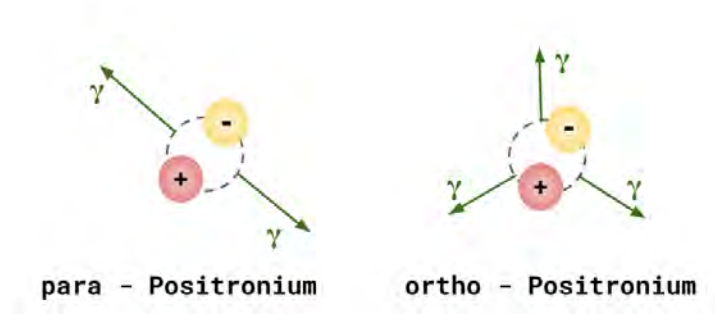


FIGURE 2.2: Schematic view of positronium intrinsic decay.

decrease to even a few nanoseconds. In Fig. 2.3 schematic view of pick-off decay is presented.

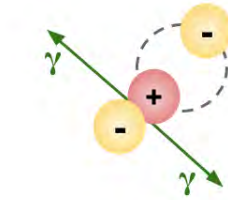
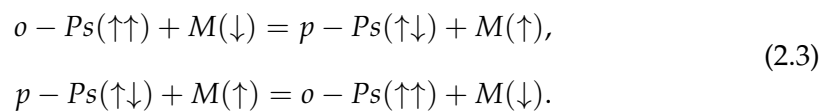


FIGURE 2.3: Schematic view of pick-off decay.

Positronium interactions with paramagnetic ions in the matter can cause the ortho-para conversion, due to spin-exchange with molecule's unpaired electron and the electron in positronium atoms, having opposite spin to each other. This process can occur in both way, there is ortho to para and para to ortho, which can reduce the mean lifetime of o-Ps and increase the mean lifetime of p-Ps in comparison to values in vacuum [37,38]. Process of exchanging spin with a molecule (M) can be described by Eq. 2.3:



Both pick-off process and ortho-para conversion are responsible for the shortening of a mean o-Ps lifetime. The ratio between these two processes depends on the material in which positronium is trapped. Recent studies have shown that in case of water, both these processes occur at a similar rate as opposed to other liquids, where ortho-para conversion is a dominant process [39].

In PALS, one more annihilation process is taken into account, not of positronium itself, but of a thermalized positron which did not create a bound state. If positronium was not formed, positron can diffuse in the matter for 100-500 ps depending on the electron density of the material and then directly annihilate with surrounding molecule's electron predominantly into two gamma quanta, each with the energy of 511 keV. Each of the aforementioned decays processes contributes to the positron lifetime spectrum.

2.3 Tao-Eldrup Model

Tao-Eldrup model describes positronium trapped in the region of lower electron density, called free volume or void. Assuming the void as a potential well, the void size with the mean lifetime value of annihilating o-Ps can be correlated.

The free volume in the material structure is treated as a well of finite depth potential. It is assumed that on the border, atom - free void, there is an infinite jump in the potential of V . Correlating mean o-Ps lifetime with the void size requires calculating the probability of finding positronium outside of the well, which would be difficult without any simplification. Such simplification was proposed by Tao, who described the volume as infinite spherical potential well with depth V and radius $R_0 = R + \Delta R$, where ΔR parameter represents the overlap of the positronium wave function with the medium wave functions [40]. This representation with potential well broadened by ΔR is presented in Fig. 2.4.

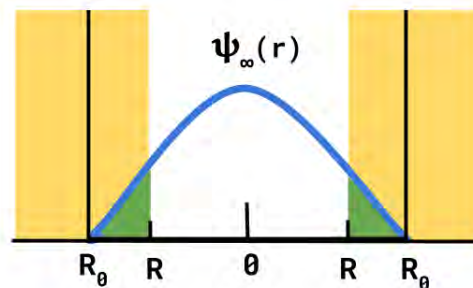


FIGURE 2.4: Broadened infinite potential well, where $R_0 = R + \Delta R$.

Positronium wave function outside the well is equal to zero. Therefore the probability of finding positronium outside the potential well with radius R will be equal

to the probability of finding it in a ΔR layer and can be estimated by Eq. 2.4.

$$P = 4\pi \int_R^\infty |\psi_{out}(r)|^2 r^2 dr = 4\pi \int_R^{R_0} |\psi_\infty(r)|^2 r^2 dr. \quad (2.4)$$

Later, Eldrup calculated the probability for the ground state of infinite potential well and therefore formulated the dependency of the mean lifetime value on the void radius Eq. 2.5 [41]:

$$\tau_{Ps} = \frac{1}{2} \left(1 - \frac{R}{R + \Delta R} + 2\pi \sin \left(\frac{2\pi R}{R + \Delta R} \right) \right)^{-1}. \quad (2.5)$$

where: τ_{Ps} - mean lifetime of positronium, R - radius of free void. Broadening parameter ΔR value was estimated empirically to 0.166 nm [42].

Tao-Eldrup model is well applied in spherical volumes with a radius between 0.2 - 2 nm, which corresponds to the lifetime of 1.2 to 40 ns, while the best correlation with the model is observed in range 1.8 - 6.2 ns [43]. Since values observed in the biological specimen are within this range, it is reasonable to apply this model for analysis.

Chapter 3

Carcinogenesis

3.1 Cancer - its origin and development

Neoplasm is a general term to describe a group of lesions, which are characterised by abnormal proliferation of the genetically modified cells, with an unusual metabolic activity, which influences the general state of the organism in various degrees. Such lesions are ongoing despite the loss of factor that caused it and did not react to natural regulatory mechanisms. Mainly neoplasms can be divided into two groups: benign tumours and malignant tumours (cancer).

Benign cells have a similarity to their stem cell and are well differentiated, and therefore tumours are progressing slowly as an encysted change and do not form metastases. Usually, this process is long and less invasive on the organism, although it depends strictly on tumour localisation, also recurrences after ablation are rare.

Cancer cells, on the other hand, are undifferentiated and manifest the ability to infiltrate throughout the blood vessels to distant places from the primary neoplasm, causing metastases. Malignant tumours are characterised by rapid proliferation and possible recurrences after surgery or other treatment, resulting in more frequent death of the affected subjects, than in case of benign tumours [44].

Cancer is the second leading cause of death globally after cardiovascular diseases and is responsible for an estimated 9.6 million deaths in 2018. Globally, about 1 in 6 deaths is due to cancer and over 18 million new cases were diagnosed in 2018 [45]. In Fig. 3.1 main types of newly diagnosed cancers in 2018 are presented.

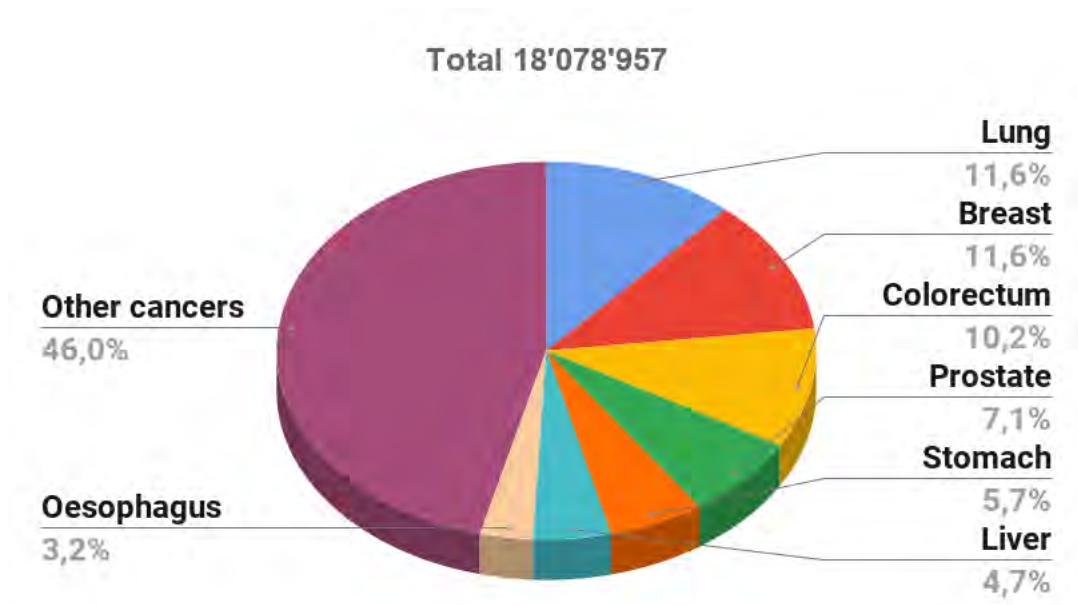


FIGURE 3.1: Estimated number of new cases of cancer, worldwide, in both sexes and all ages in 2018. Figure adapted from IARC <http://gco.iarc.fr/>.

Carcinogenesis is the process of cancer formation and progression due to DNA changes, including mutations, polymorphisms and viral transformations leading to DNA instability. Many superimposed factors, called carcinogens, are responsible for DNA mutations and can be divided into three groups: physical, chemical and biological. Main physical carcinogens are ionising (X- and γ) or UV radiation. According to the epidemiological studies with atomic bomb survivors, the dose-response relationship for risk of multiple solid cancers is observed in the range 0-100 mSv and for nuclear industry workers increased with the dosage risk of leukaemia and colon cancers is observed in the range of 0-300 mSv [46,47]. UV radiation is the main factor responsible for skin cancers, estimated to be the cause of melanoma in 160'000 people per year, which corresponds to over 75% cases of all diagnosed melanomas. [48].

Chemical carcinogens are various substances, such as nitrosamines (in cigarettes), benzene or asbestos. Tobacco causes over 20 different types of cancer and is the reason for 2.4 million people death per year [49]. Biological ones are genetic predisposition (inheritable or spontaneously created), hormonal factors or some viruses and bacterias such as HPVs, HBV, HCV and *Helicobacter pylori* – which alone were responsible for about 2 million cancer cases in 2018 [50]. Transforming retroviruses carry oncogenes derived from cellular genes, during their replication in cells. Some

oncoviruses can activate the expression of cellular proto-oncogenes in cells, while others target tumour suppressor genes, by impairing functions of tumour suppressor proteins, such as p53 or pRb. As a result, viral carcinogens modulate growth control pathways in cells, leading to cancer development [51].

Cancer usually starts from one genetically transformed cell. Such genetic transformation (mutation) is impairing basic functions of the cell, such as control of proliferation, differentiation etc. Regulation of the cell cycle includes the key elements of the cell control system, the detection and correction of genetic mutations as well as different surveillance systems to prevent uncontrolled cell division, and these are so-called 'checkpoints'. ATM and ATR serine/threonine-protein kinases, as well as so-called 'gatekeepers' (p53, pRb) are responsible for the proper functioning of cells. Therefore, one genetic transformation would not necessarily lead to the development of cancer in the organism [52,53].

The process of carcinogenesis is divided into three phases: (1) initiation – single mutation is created caused by a carcinogen influence, but can also occur spontaneously, (2) promotion – multistage development of cell colonies, containing the mutation acquired in the process of initiation, and (3) progression – irreversible stage leading to tumour formation by a succession of molecular alterations and changes in the karyotype. Schematic view of carcinogenesis is presented in Fig. 3.2.

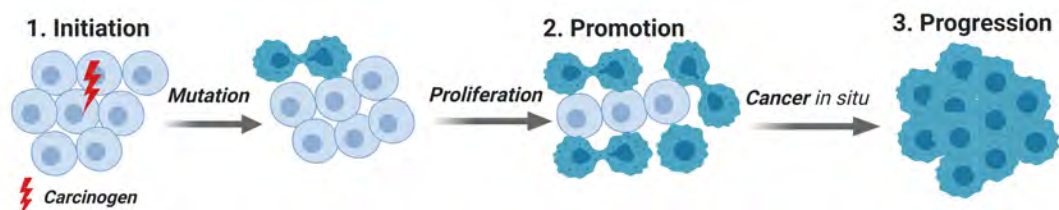


FIGURE 3.2: Schematic view of carcinogenesis process divided into three phases: initiation, promotion and progression. Created with BioRender.com

Mutation in the three main types of genes: proto-oncogenes, genome gatekeepers - suppressor genes and serine/threonine protein kinases - mutagenic genes, which are responsible for a cell control system, is what leads to the cancer formation [54].

The proto-oncogenes mutations disrupt the transmission of the growth signals. These genes are responsible for DNA synthesis and cell cycle, and mutations cause changes in the signal transduction and therefore, the unlimited ability to divide.

Impaired ability to recognise the growth control inhibitors is caused by mutation of suppressors genes (genome gatekeepers). Loss of ability to enter apoptosis or controlled protein phosphorylation, due to impaired functioning of p53 and pRB proteins, are the most significant causes leading to enhanced proliferation. These proteins are responsible for the transition from resting phases to DNA synthesis and division phases in cell cycle [55,56].

Defects in mutagenic genes, as one coding ATR and ATM serine/threonine-protein kinases, are the main cause of perturbation of DNA repair systems. Schematic view of disrupted functioning of main mutated gene types is presented in Fig. 3.3.

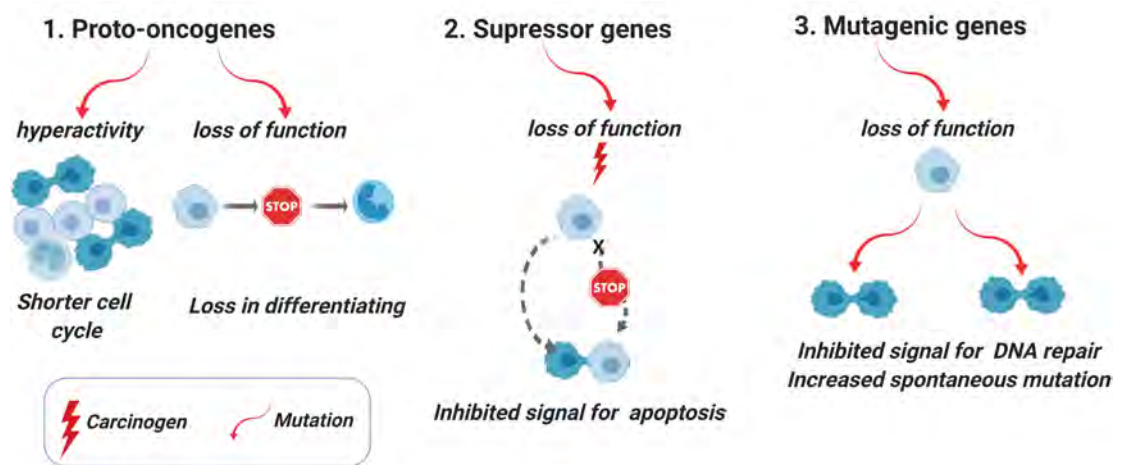


FIGURE 3.3: Schematic view of disrupted functioning of proto-oncogenes, suppressors and mutagenic genes leading to cancer development. Created with BioRender.com

Acquiring the capabilities for neoangiogenesis, infiltration, and metastases by cells, lead to fully developed cancer. Schematic view of differences in proliferation and cell arrangement in tissues of normal and tumorous cells, with a distinction between benign and malignant tumour characteristic, is presented in Fig. 3.4.

Cancer cells in the progression phase are characterised by a partial loss of adhesive properties, enhanced proliferation and proteolysis, which is causing the releasing of the tumour structure. Excessive proliferation is the main characteristic of cancer [57]. Cancer cells can grow and divide uncontrollably, while the number of normal cell's divisions is limited, the cancer cells can divide infinitely due to over-expression of telomerase [58]. Changes in the structure of the cell membrane, such as changes in proteins, receptors and ion channels presence on/in the phospholipid bilayer may cause the loss of functions, like cell-to-cell communication, reaction to

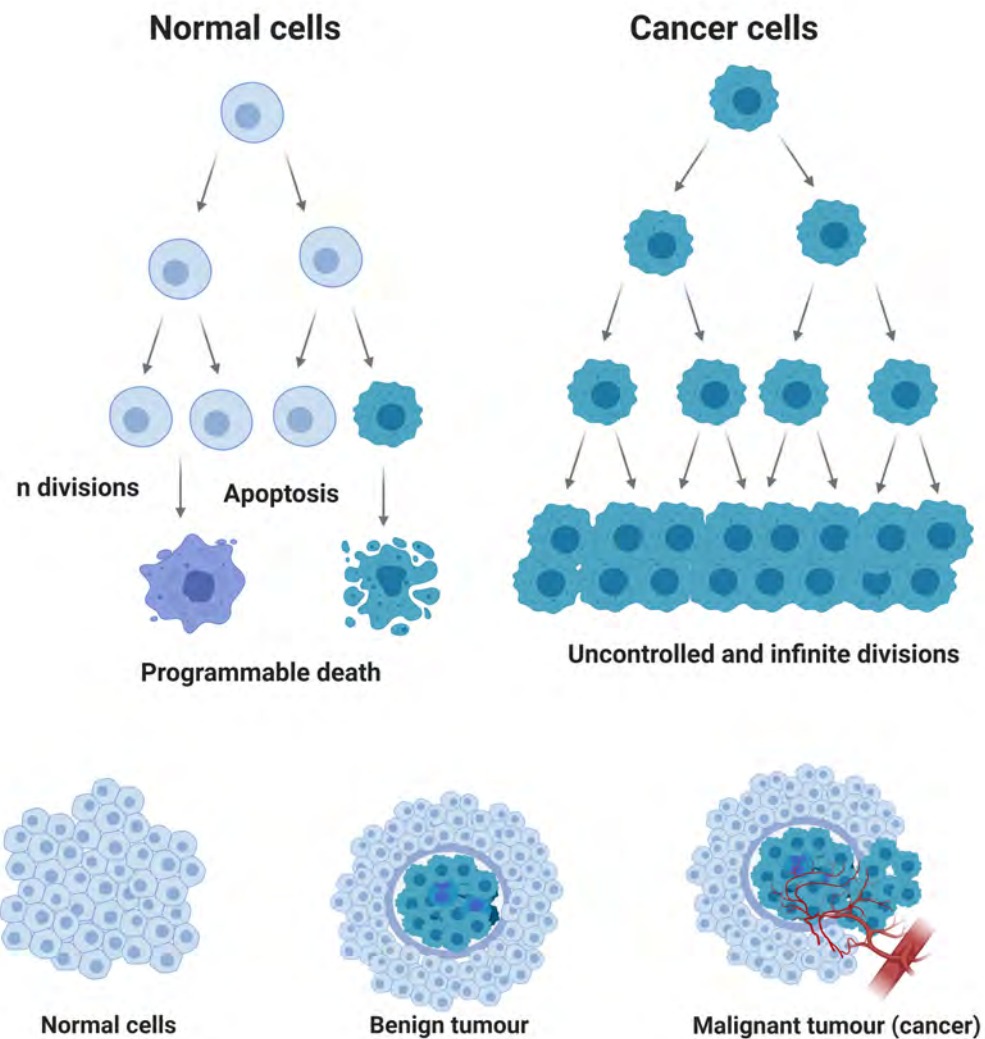


FIGURE 3.4: Differences in proliferation and spatial structuring of normal and tumorous cells. Created with BioRender.com

mechanical and chemical stimuli or cell-to-cell connections [59]. Such alterations are due to the calcium-dependent cell adherent receptors - cadherins. By losing contact inhibition, change in cell-to-cell interactions, tumour cells also acquire metabolic autonomy [60]. Inflammation and disrupted cytokines and chemokines balance, stimulate angiogenesis [61,62]. Then cells, which contain a lot of proteolytic enzymes, acquire the ability to destroy the basal membrane and therefore infiltrate the nearest blood or lymphatic vessels. Cells adhere to the endothelial wall, get outside and can be transported to the distant parts in the body, which leads to metastasis development [63]. Cancer development and progression are influenced by dynamically evolving extracellular matrix, changes in the cell milieu and are also accompanied

by the formation of extracellular vesicles (EVs) [64–66].

3.2 Differences between normal and cancer cells

Cancer cells show high variations in their genetic and biochemical parameters. Current research demonstrates that the mechanical and structural properties of the cytoskeleton, cellular environment and even the cell nucleus play a significant role in carcinogenesis and metastatic processes. Changes in the cellular membranes or cytoskeleton in the macro-scale strongly indicates changes in the micro-scale of the membrane and can be caused at an even smaller level - in nano or sub-nano scale [67].

Such differences can be recognised as morphological and functional differences. Morphologically, cancer cells are irregular in shape, have a reduced amount of cytoplasm, a more prominent and often aneuploid or multiplied nuclei and more coarse chromatin. Organelles, such as the Golgi apparatus, mitochondria or endoplasmic reticulum become reduced or have impaired function.

Increased aerobic glycolysis processes occur in mitochondrial membranes, known in the literature as the Warburg phenomenon, as well as higher reactive oxygen species (ROS) production is connected with the development of cancer [68,69]. Various biochemical and physiological oxidative processes produce ROS, as byproducts. Elevated ROS levels cause membrane or DNA damage to activate anti-tumourigenic signalling, resulting in cancer cells death due to oxidative stress. On the other hand, insufficient levels of ROS disrupt signalling processes and together with the antioxidant abilities of tumour cells drives to scavenge excessive ROS while maintaining pro-tumourigenic signalling and resistance to apoptosis [70,71]. In addition, increased ROS production leads to oxidative stress and genomic instability through mutations in mitochondrial DNA [72,73].

Altered functional characteristics of cancer cells are caused by changes in the activity of hormones, growth factors or lytic enzymes, which increase mobility and spreading of neoplastic cells. Significant differences in cell metabolism between cancer and normal cells are observed, especially in case of glucose, of which elevated levels cause a higher production of ROS as byproducts [74].

For the application of PALS technique in studies of differences between normal and cancer cells, these changing ROS levels can play a significant role since free radicals are highly reactive and can influence positronium lifetime and its production probability [75].

Main characteristics, which distinguish cancer cells from normal ones, are shown in Fig. 3.5.

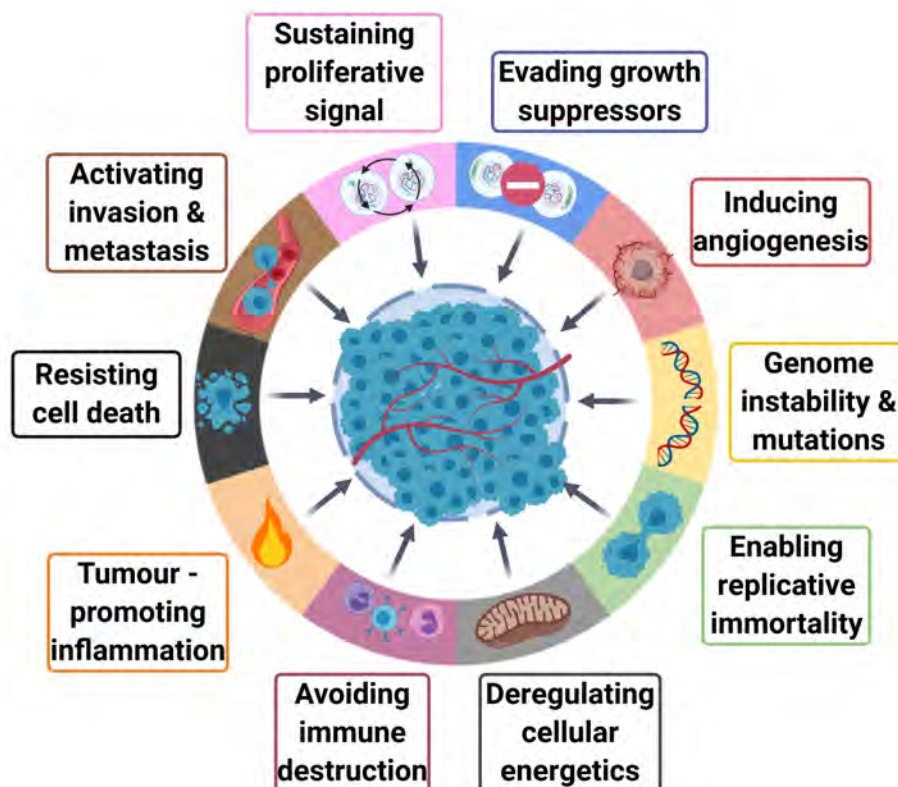


FIGURE 3.5: Main characteristics distinguishing cancer cells from normal cells. Figure adapted from D. Hanahan, R. A. Weinberg [63]. Created with BioRender.com

The sum of all aforementioned differences in both morphology and functionality between normal and cancer cells can influence positronium interaction in a given type of cells and therefore, can be a valuable new biomarker in cancer diagnostic.

3.3 Melanocytes and melanoma

Melanocytes originate from the neural crest cells and are located within the basal layer of the epidermis, hair follicles, eyes, ears and meninges. Its functioning depends on the expression of the tyrosine kinase receptor. It contains melanosomes in

which melanin biopolymers – eumelanin and pheomelanin – are formed from L - tyrosine in multistage oxidation and polymerisation process called melanogenesis. This process consists of several stages, firstly hydroxylation of tyrosine to L - DOPA and oxidation of L - DOPA to L - DOPAquinone, then depending on the presence or lack of cysteine, pheomelanin or eumelanin is formed respectively, through polymerisation. [76]. Synthesised melanin is transported *via* dendritic like tabs to keratinocytes in the upper layer of the epidermis, where it accumulates over cell nuclei, forming the so-called supranuclear caps that protect genetic material from the harmful effects of UV radiation [77]. Schematic view of the epidermis with melanocytes is presented in Fig. 3.6.

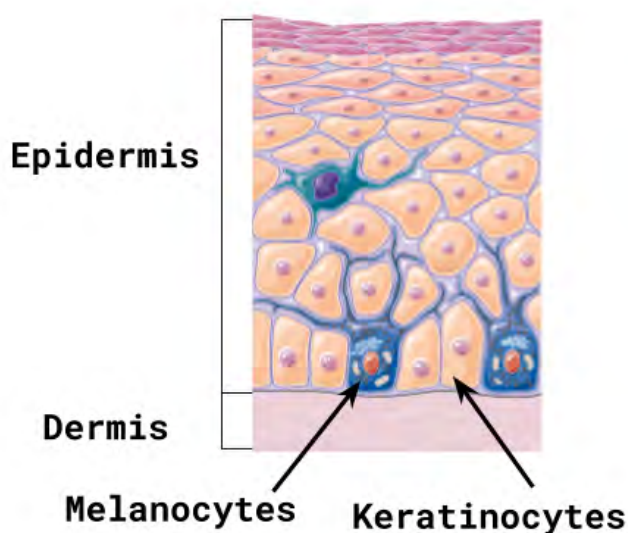


FIGURE 3.6: Schematic view of the epidermis with melanocytes. Figure adapted from Servier Medical Art [78].

Melanocytes are immunocompetent cells and serve as an essential element of the skin's immune system. Stimulated melanocytes can express antigens of the major histocompatibility complex (MHC). It is a complex process regulated by endogenous (autocrine, paracrine, and endocrine) and exogenous (UV radiation, drugs) factors. Additionally, melanin is an excellent free radical scavenger and therefore decreases ROS levels [79, 80].

The neoplastic transformation of melanocytes causes melanoma, and in 25% of cases, it derives from pre-existing nevi through a multi-step process regulated by a set of genes. Cells must acquire successive genetic mutations prior to forming melanoma tumours and metastases [81]. Differences in the level of production of

several growth factors and cytokines such as keratinocyte growth factor (KGF), tumour necrosis factor α (TNF- α), platelet-derived growth factor (PDGF), several interleukins and others, act as regulators of melanoma cell proliferation, differentiation, and motility [82]. In the development of melanoma, two main factors play a crucial role: environmental (UV radiation) and genetic predispositions. Also, the more present melanocytes nevis the higher risk for melanoma growth.

Melanoma is one of the highly mutating cancer, with the two most frequently recognised mutations, which are $BRAF^{V600E}$ and $NARS^{Q61}$, responsible for around 40% and 20% cases of all melanomas, respectively [83]. Protein - kinase B is a product resulting from a mutation in the BRAF gene and plays a vital role in cells growth and regulation of proliferation. Hence, it is the leading cause of uncontrolled proliferation and melanoma development.

Malignant melanoma is most common in people with blue eyes, pale complexion and fair or red hair. The highest cumulative incidents rate per country per 100k people in all ages and sex of melanoma is observed in Australia, North America, West Europe and Scandinavia, with over 5.4 incidents per 100k people [45].

Five stages of melanoma are described based on the development of cancer, as presented in Fig. 3.7.

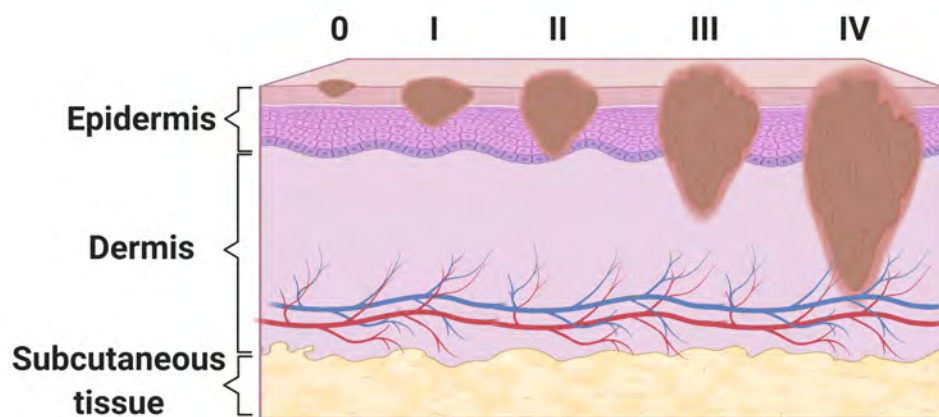


FIGURE 3.7: Schematic view of melanoma's stages. Created with BioRender.com

In stage zero, melanoma cells are contained within the epidermis, so-called melanoma in situ or nevi. In the first stage, the cancerous tumour has formed, but has a thickness below 1 mm, while in the second stage melanoma increases in depth up

to 2 mm. In the third stage, melanoma occurs with lymph nodes and have up to 4 mm depth. The fourth stage manifests itself by the possibility for metastasis and has over 4 mm depth [84, 85].

For described research, two melanoma cell lines derived from the same patient (primary and metastatic) were studied as an example of a malignant neoplasm. Both of these cell lines share a mutation in the $BRAF^{V600E}$ gene.

3.4 Cardiac Myxoma

Cardiac myxoma (CM) is a sporadic heart disease with an overall incidence of about 0.5 per million people per year. Still, it accounts for approximately 50-75% of benign and about half of the all primary cardiac neoplasms [86, 87]. CM occurs predominantly in adult women, although the cause for the discrepancy in occurrences to sex is unknown. The tumour usually arises from the endocardium into the cardiac chamber. About 75% of cardiac myxomas are located in the left atrium, 8-18% in the right atrium, 2-5% are in each ventricle and 1-6% the valves [87–89]. Schematic view of cardiac myxoma in the left atrium of the heart is presented in Fig. 3.8.

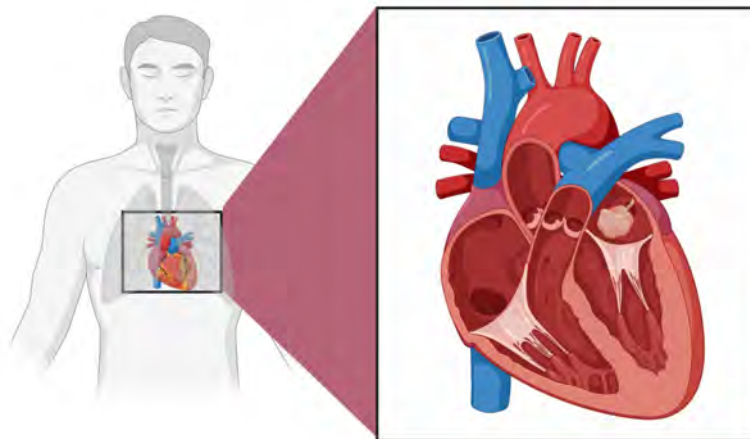


FIGURE 3.8: Schematic view of cardiac myxoma in the left atrium of the heart. Created with BioRender.com

Cardiac myxoma is described as a neoplasm composed of stellate to polygonal, cytologically bland, mesenchymal cells, usually singly arranged, in small clusters,

or rudimentary vascular formations in a myxoid stroma [90]. The precursor mesenchymal cells can differentiate into endothelial and epithelial cells, smooth muscle cells, angioblasts, fibroblasts, cartilage cells, and myoblasts forming myxoma tumour [91]. Around 7% of cardiac myxomas arise as components of a heritable disorder, so-called familial myxomas, with endocrinopathy and spotty pigmentation of the skin, which is referred to as a Carney complex [92, 93]. Familial myxomas are caused mostly due to mutations in the PRKAR1A gene on chromosome 17, but other clonal abnormalities, mostly on chromosome 2 and 12 also appear to be implicated with the myxoma formation [94, 95]. For sporadic (non-familial) myxomas, no specific recurrent chromosomal aberrations were found. However, karyotype aberrations (trisomy 21) and hematopoietic progenitor cells can play a role in the genesis of sporadic myxoma [96]. Even though myxoma is a benign tumour, there are some reports on its malignancy potential, which include: local relapse, local invasiveness, distant metastasis. There are some findings of sarcomas arising from myxoma recurrences or cerebral metastasis [87, 97].

Usually, myxoma can develop without any symptoms, although it strictly depends on the size of the tumour. Left atrial myxomas begin to show any symptoms, when they obstruct the mitral valve, embolism peripherally, or cause systemic effects. Most common symptoms found are dyspnea, valvular obstruction, systemic emboli and non-specific signs such as myalgia, muscle weakness, arthralgia, fever, weight loss, and fatigue [86]. Serologic and haematological abnormalities in tests, with elevated levels of IL-6, are observed in one-third of patients [98].

The gold standard in cardiac myxoma diagnosis is echocardiography (ECHO), both transthoracic and transesophageal. Myxomas are sometimes misdiagnosed since based on ECHO it is difficult to differentiate them from other intracardiac thrombus or cardiac tumours [99]. The only method of treatment of cardiac myxoma is radical surgical tumour excision using extracorporeal circulation [89]. Recurrences are reported from as soon as a few months to as long as 14 years after excision of the myxoma in 2-3% of patients [100].

Part II

Material and Methods

Chapter 4

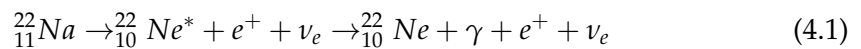
PALS technique

The main goal of this thesis is to apply the Positron Annihilation Lifetime Spectroscopy technique to study biological samples and to examine the potential of positronium as a new diagnostic biomarker. Applying PALS technique required numerous alterations in both spectrometer and chambers design, with respect to those typically used in material studies. The main challenge in studying biological samples is in performing statistically efficient measurement in a short time, without the increasing activity of the source. In addition, it was essential to incorporate similar analysis methods as developed by the J-PET collaboration, in order to apply the results of the thesis for diagnostic interpretation of positronium images [1, 2, 23–26, 101].

In this chapter, the final version of the setup and analysis is presented. All improvements and modernisation applied during tests allowed to reduce the time of a single measurement from around 20 to around 1 hour, and it was crucial for the success of this research.

4.1 Source of positron

As a source of positrons, an isotope of Sodium-22 was used in form of $^{22}\text{NaCl}$ solution, sealed between two sheets of 6 μm Kapton foil. This isotope, with half-life of 2.6 years, decays via β^+ decay to Neon-22 producing a positron (Eq. 4.1):



Sodium-22 isotope is commonly used in PALS research since, in addition to positron, it emits gamma quantum with energy of 1274 keV (deexcitation gamma

quantum) *via* decay chain described in Eq. 4.1 and indicated in Fig. 4.1. In particular, the gamma quantum is emitted by the excited $^{22}\text{Ne}^*$, on the average, 3.6 ps after the emission of positron [102]. Since the emission of deexcitation gamma quanta occurs in almost the same time as the production of a positron, it is taken as a start time of positronium creation.

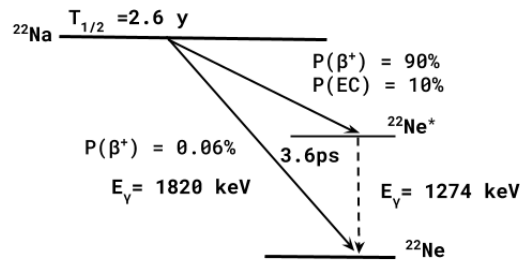


FIGURE 4.1: Sodium-22 decay scheme.

Source used for the measurement was prepared by the imposition of $^{22}\text{NaCl}$ solution in point marked on the foil, after evaporation of all liquid, both parts of Kapton foil were glued together. In this way, a sealed 'point-like' (with the dimensions of about 1 mm) sodium source, with the activity of about 1 MBq was created. Shape and dimensions of foils were adjusted to chambers used for given measured samples. Scheme and photograph of the source in the chamber are presented in Fig. 4.2.

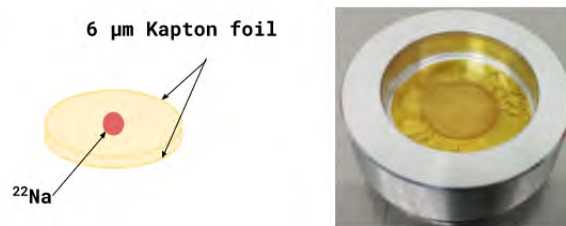


FIGURE 4.2: (left) Scheme and (right) photograph of Sodium-22 source sealed in Kapton foil, and inserted into the aluminium chamber.

4.2 PAL spectrometer

Studies presented in this thesis were performed by means of PAL spectrometer consisting of two H3378-51 Hamamatsu photomultipliers and BaF_2 cylindrical scintillators with 38 mm diameter and 25 mm height manufactured by Scionix, powered

by CAEN SY4527 high voltage (HV) power supply. Signals from photomultipliers were attenuated by 10 dB (indicated as A in Fig. 4.3) and delivered to LeCroy 608C constant fraction discriminator (CFD), where different thresholds were applied to signals from different detectors. On the first detector, high threshold is applied to register only 1274 keV gamma quantum from the deexcitation (START). For the second one, low threshold allows to register annihilation gamma quantum (STOP). Coincidence time window was set to 110 ns on LeCroy 622 coincidence module (CON). Data was acquired by digitised DRS4 evaluation board. Scheme of the setup is presented in Fig. 4.3.

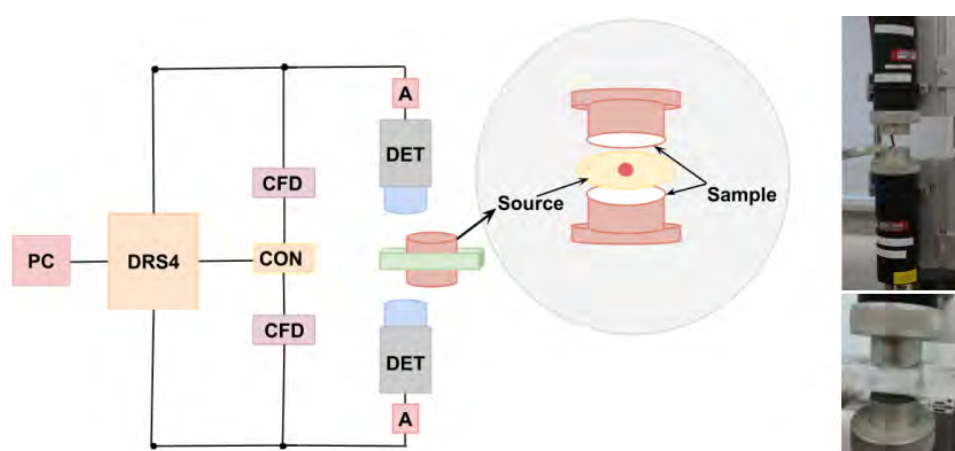


FIGURE 4.3: (left) Scheme of the detection system and chamber construction. (right) Photograph of detectors with holder between them.

Detectors were aligned parallelly (180°) allowing to register high statistic for both 511 keV and 1274 keV gamma quantum. In addition, the source was shifted from the centre axis between detectors by more than the radius of crystal scintillator, which geometrically prevents registration of 511 keV gamma quanta by both detectors, therefore allows only to register pairs of deexcitation and annihilation gamma quanta.

4.3 Holder and chambers for biological samples

Two types of samples were studied in this thesis: cultured cell lines and tissues sections from a patient. In both cases, samples were either fixed or living and therefore required different conditions for measurement and different chamber design (as in Fig. 4.3). All used chambers were made from aluminium and had a shape enabling

to sandwich the source between two parts of the sample. In order to perform repeatable and comparable measurements samples of the same kind (cells or tissues) were measured in the same chambers regardless of fixation state or type (cancer/normal).

Chambers design for cell culture measurement required additional holder providing temperature control, allowing to measure at 37°C. Depending on the volume of a sample, chambers with two inner dimension were used. One with a diameter of $d=1$ cm and height of $h=0.5$ cm, and other with dimensions $d=0.5$ cm and $h=0.3$ cm. Design of a chamber and a holder for culture cells measurements are presented in Fig. 4.4. In case of measurement of the fixed cells, the same chamber was used. However, the measurement was performed at room temperature.

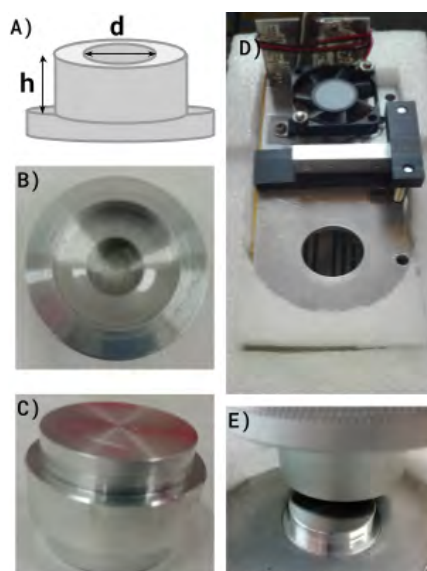


FIGURE 4.4: (A) Scheme of the chamber with marked inner dimensions d - diameter and h - height. (B) Photograph of one part of the chamber. (C) Closed chamber with sample and source. (D) Temperature controlled holder. (E) Chamber mounted in the holder between detectors.

Specimens from the patient's tissues were all measured at room temperature, regardless of the fixation state. The inner shape of the chamber was cylindrical, as for cells chamber but with different dimensions, depending on the sample size – the bigger one with $d=1$ cm and $h=1$ cm and smaller with dimensions of 0.5 cm and 1 cm, respectively. In the case of tissues, a controlled temperature holder was not required, and a plastic tube was used as one (Fig. 4.5).

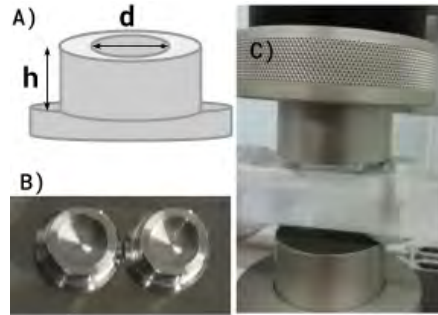


FIGURE 4.5: (A) Scheme of the chamber with marked inner dimensions d - diameter and h - height. (B) Photograph of both parts of the chamber. (C) Chamber mounted in the holder between detectors.

4.4 Data analysis

4.4.1 Amplitude and charge calculation

As a photomultiplier (PMT) converts photons from scintillations into an electrical signal, amplitude and charge, which are proportional to the deposited energy in the scintillator, are calculated. These values are essential for separating annihilation and deexcitation gamma quantum, and for determining the time difference between signals coming from two PMTs at a fixed fraction of the amplitude, and therefore the lifetime of positronium.

In Fig. 4.6 exemplary signal is presented (left) with the method of calculating amplitude and charge, (right) and pair of signals from both detectors with the presented method for the time at fraction calculation.

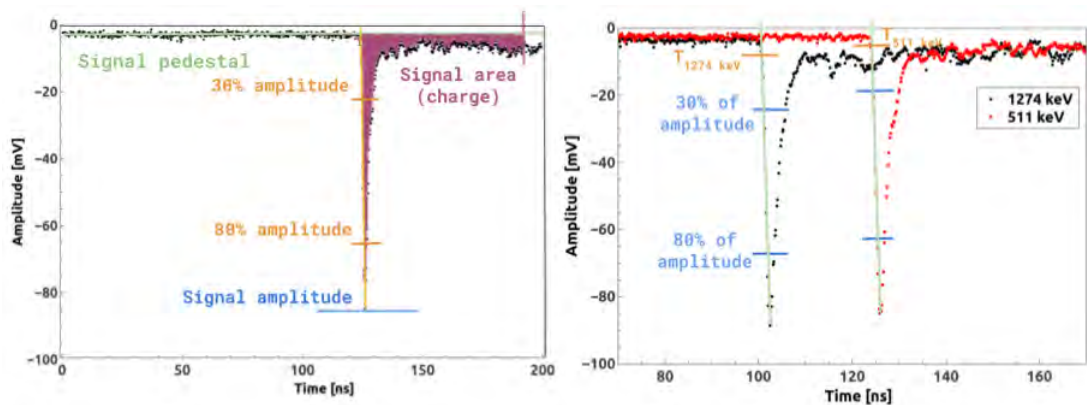


FIGURE 4.6: (left) Exemplary signal. The shaded area under the signal is used for the determination of the signal's charge. The blue line indicates the amplitude of the signal, while yellow lines show an exemplary height of the signal at 30% and 80% of the amplitude. (right) Pair of signals from both detectors with the presented method for the time at fraction calculation.

Signals are sampled in discrete points with 280 ps intervals. Pedestal (Ped) of a signal is calculated as a mean value for 10 points, omitting first 20 points on the left side of the spectrum. The amplitude (A) is calculated as a minimum value of the signal (Eq. 4.2). In order to estimate the time at a given voltage, linear function (Eq. 4.3) is fitted to the leading edge in the range 30% to 80% of amplitude. As presented in Fig. 4.6 (right) the time (t) is determined as a crossing of the fitted line with the voltage level corresponding to the 10% of the amplitude.

$$A = A_{min} - Pedestal, \quad (4.2)$$

$$U_{lin}(t) = a \cdot t + b. \quad (4.3)$$

Charge (Q) of the signal is given by the relation:

$$Q = \int \frac{U(t)dt}{R}, \quad (4.4)$$

where U(t) is a signal voltage, and R is the resistance of given channel on DRS4 board, which is constant for all measurements and equals to 50Ω. Value of $\int U(t)dt$ is estimated as an area under the signal, as it is indicated in the left panel of Fig. 4.6.

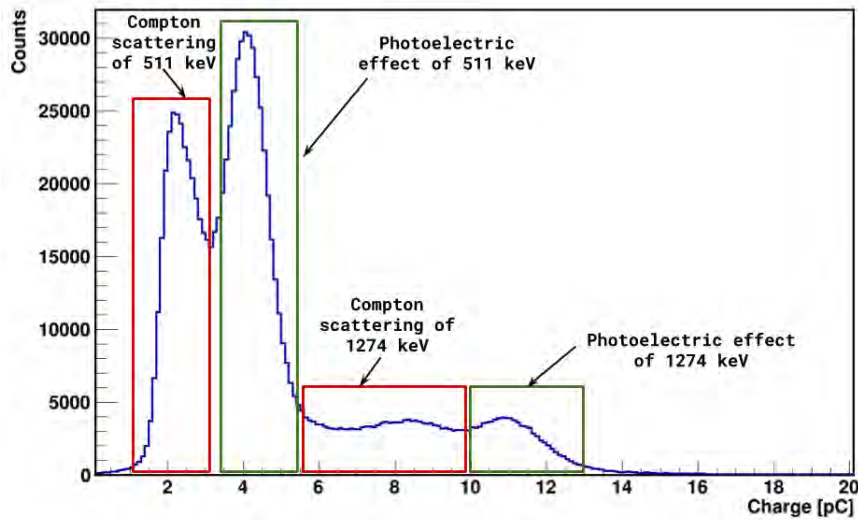


FIGURE 4.7: Energy spectrum for ^{22}Na isotope is presented with marked regions describing their physical origin.

As mentioned before, the charge of the signal is proportional to the energy deposited by gamma quantum in the detector. In Fig. 4.7 energy spectrum for ^{22}Na

isotope is presented, with marked regions describing different interactions of annihilation and deexcitation quanta in the scintillator. Such interactions in case of crystal scintillator are based on two physical phenomena: the Photoelectric effect and the Compton scattering.

In Fig. 4.8 exemplary spectra of (left) Amplitude and (right) Charge are presented, (up) before and (lower panel) after applying different trigger thresholds.

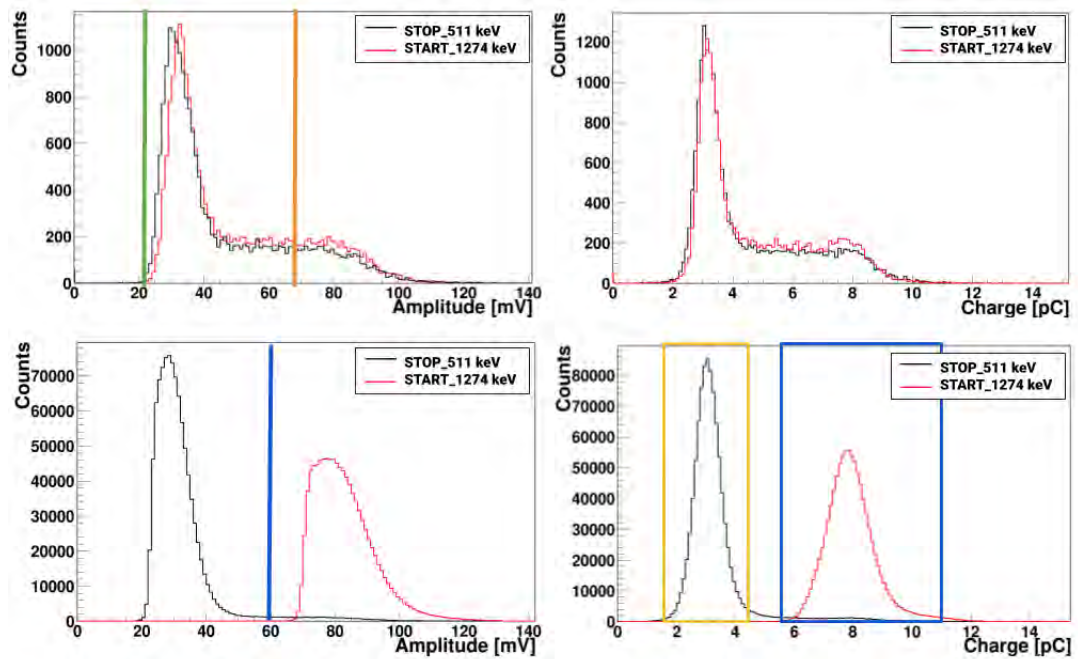


FIGURE 4.8: Exemplary spectra of signal's amplitude (left) and charge (right). (upper) Before applying different trigger thresholds, marked as a green line for gamma quanta with lower energy and yellow for gamma quanta with higher energy. (lower panel) Amplitude and charge spectra after applying the thresholds indicated in the left upper figure. Blue and yellow lines indicate the range of signal charge window taken for the analysis.

In order to increase statistic in the region of interest, therefore to collect only signals with energy in photoelectric peak window, for deexcitation (1274 keV) and annihilation (511 keV) gamma quantum, different trigger thresholds are applied. For detector assigned to register deexcitation gamma quantum, the threshold is set to -67 mV, and for other detector assigned for annihilation gamma quantum, the threshold is set to -22 mV. Thresholds values were experimentally estimated, based on the measurement of sodium spectra in full energy range, and are marked as green and yellow lines in Fig. 4.8 (upper left). Amplitude and charge spectra after applying two different thresholds are presented in the lower panel. To get rid of bias signals from scattering in the detectors, as well as, some incorrectly registered by the DRS4

board, additional cuts were applied for time difference calculation. As signals coming from annihilation, only those with charge between $1.5 - 4.5 \text{ pC}$ are accepted, and for signals originating from deexcitation it is required that charge is between $5.5 - 11 \text{ pC}$, and that amplitude is higher than $> 60 \text{ mV}$.

4.4.2 Lifetime distribution

Time difference ($\Delta T = T_{511\text{keV}} - T_{1274\text{keV}}$) is calculated for the pairs of signals fulfilling all criteria mentioned in 4.4.1 and registered in the same time window, which width is constant through all measurements and equal to 110 ns . $T_{511\text{keV}}$ and $T_{1274\text{keV}}$ are calculated at constant fraction at 10% of signal's amplitude using Eq. 4.3, as shown in Fig. 4.6 (right).

Exemplary lifetime distribution in both linear and logarithmic scale is presented in Fig. 4.9

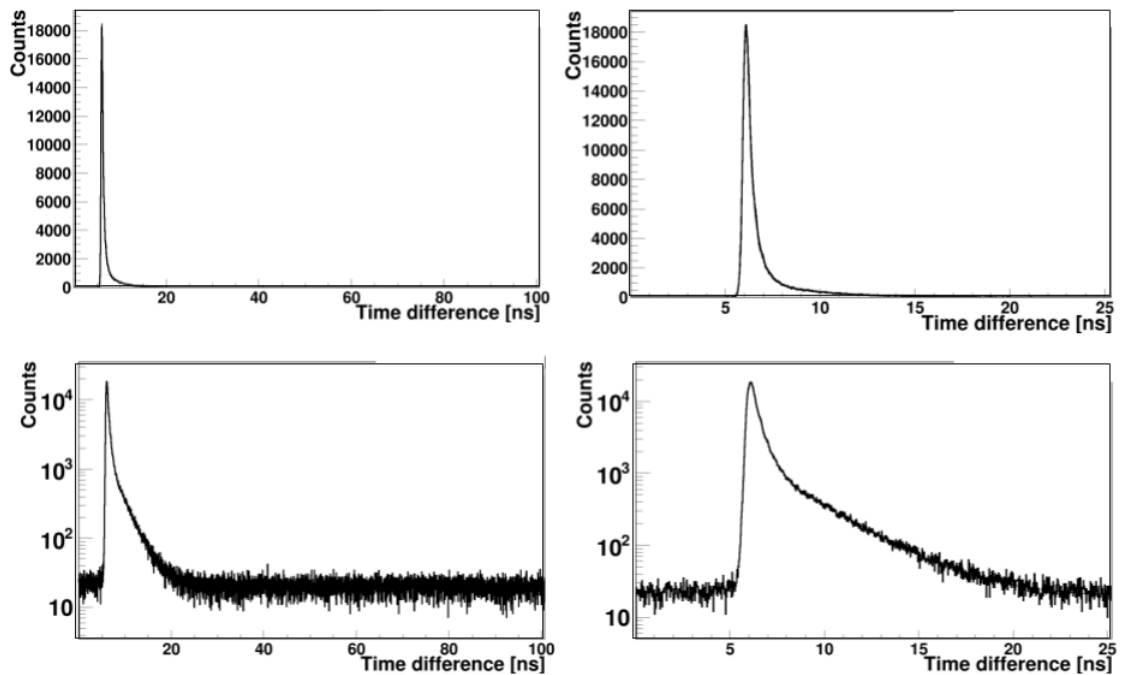


FIGURE 4.9: Exemplary spectra of positron lifetime distribution in (upper) linear and (lower panel) logarithmic scale, (left) in full-time window range and (right) zoomed.

4.4.3 Positronium mean lifetime estimation

The lifetime of positronium depends on the electron density of the material in which it is produced. The smaller are the so-called 'free volumes', the higher is the probability that positron from the positronium will annihilate with an electron from the material due to the 'pick-off' process or by ortho-para conversion, which are the main reasons for shortening positronium mean lifetime in the material.

Experimental distribution of the positronium lifetime spectrum, in case of a single mean lifetime component (τ), may be approximated by function [101]:

$$F(t; \tau, t_0, \sigma) = \frac{1}{2 \cdot \tau} \exp\left(\frac{\sigma^2}{2 \cdot \tau^2} - \frac{t - t_0}{\tau}\right) \left(\operatorname{erf}\left(\frac{t - t_0 - \frac{\sigma^2}{\tau}}{\sqrt{2} \cdot \sigma}\right) - \operatorname{erf}\left(\frac{-t_0 - \frac{\sigma^2}{\tau}}{\sqrt{2} \cdot \sigma}\right) \right), \quad (4.5)$$

where: t_0 - time offset of the detector, σ - resolution of the apparatus, t - time difference between detectors, τ - mean positron lifetime, and erf is an error function defined as in Eq. 4.6.

$$\operatorname{erf}(t) = \frac{2}{\sqrt{\pi}} \int_0^t \exp(-s^2) ds. \quad (4.6)$$

Positronium lifetime is analysed with *PALS Avalanche* program developed by K. Dulski for the J-PET collaboration [101, 103].

In order to determine the distribution of positronium mean lifetime, a discrete distribution of free volumes (hence the discrete contribution of mean lifetime components) is assumed and the following function is fitted:

$$f(t) = y_0 + \sum_{i=1}^{n_\tau} I_i \cdot F(t; \tau_i, t_0, \sigma), \quad (4.7)$$

where: y_0 - background level, n_τ - number of components, I_i - intensity of i-th component, τ_i - mean lifetime of i-th component and $F(t; \tau_i, t_0, \sigma)$ is a function given by Eq. 4.5.

In case of samples studied in this thesis, four components ($n_\tau = 4$) were fitted to the spectra corresponding to lifetime and intensity of:

- τ_1, I_1 - para-Positronium annihilation,

- τ_2, I_2 - free positron annihilation in the sample,
- τ_s, I_s - free positron annihilation in the source material (Kapton foil),
- τ_3, I_3 - ortho-Positronium annihilation,

where: source component lifetime and intensity (τ_s, I_s) were fixed in the analysis to 0.374 ns and 10%, respectively [104]. All other components were treated as free parameters in the fit of Eq. 4.7 to the experimental data.

In Fig. 4.10 exemplary lifetime spectra with fitted functions and determined mean lifetime, and intensity components are presented:

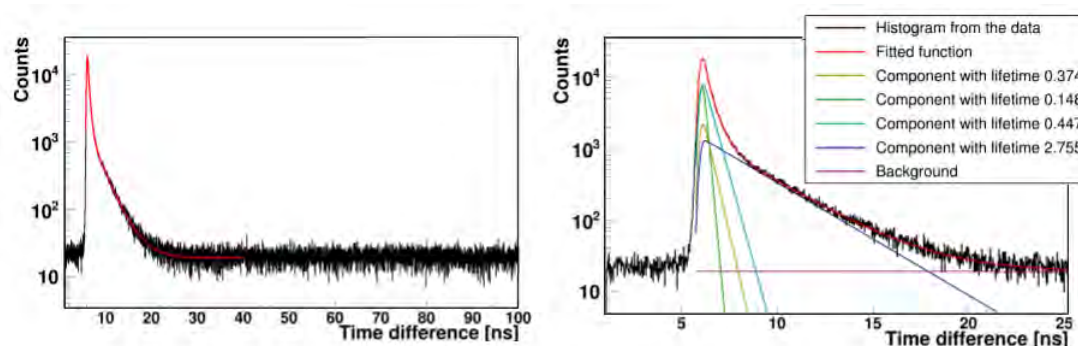


FIGURE 4.10: Exemplary positron lifetime spectrum in full (left) and extended scale (right). Superimposed lines indicate the distributions of particular components resulting from the fit of Eq. 4.7. The red line denotes the fitted function, green is p-Ps distribution, yellow - source material, turquoise - free positron annihilation, blue - o-Ps annihilation and purple background level. The spectra do not start at zero because of the different time offset between the detectors.

4.5 Setup optimization and calibration

Detection setup had to be optimised in order to shorten the time of measurement without increasing source activity. Therefore, before the main part of the measurement, different options of the setup were tested in order to find an optimal one. Main changes introduced to the setup since its assembly [103], were exchanging the Signal Data Analyser oscilloscope to the digitised DRS4 board and testing various external trigger options. Additionally, DRS4 software for saving signals was optimised to speed up the rate. All these changes were essential for performing high statistic measurement (with about 10^6 collected events), within around one hour since the time of measurement is crucial for studies of cell lines and non-fixed tissues.

Apart from changes mentioned before, in order to fully optimise the PALS setup, development of fast calibration procedures was necessary, in order to obtain the best possible resolution of the detection system.

4.5.1 Gain calibration

Even for the same type of photomultiplier, their gain can differ. Since positronium lifetime analysis strongly depends on the time and energy resolution, it is necessary to perform gain calibration for both PMTs in the setup.

Gain is a parameter describing how the detector is amplifying the electric signal, and it strongly depends on the applied voltage. Ideally, if two different PMTs of the same type have identical gain, then applying the same power voltage, would result in the same amplification of signals in both detectors. Unfortunately, typically this is not the case and performing gain calibration is required.

In Fig. 4.11, a scheme showing a secondary emission in PMT is presented. Firstly, a photon hits photocathode, release photoelectron, which is then accelerated in an electric field inside PMT, and after striking the first dynode, secondary electron emissions occur. This emission is repeated in all dynodes of the photomultiplier, causing amplification on the signal at the anode.

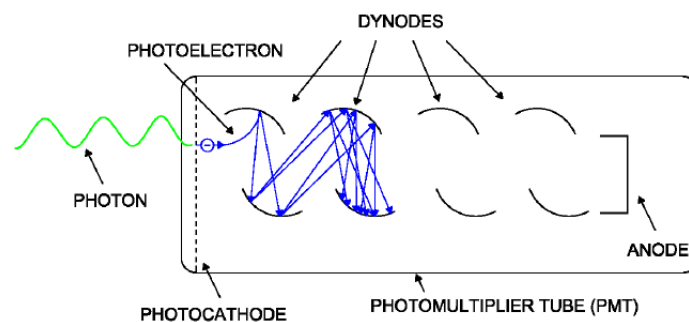


FIGURE 4.11: Scheme of secondary electron emissions in PMT. The figure is adapted from T. Bednarski et al. [105].

Therefore, the gain of the photomultiplier, depends on the number of dynodes n and secondary emission coefficient δ . Assuming that, there are n identical dynodes in PMT, gain g can be defined as:

$$g = \delta^n = k \cdot U^{n-a}, \quad (4.8)$$

where: k is a constant, a is a coefficient determined by the dynode material, and geometric structure and U is a supplied voltage. Signal's charge resultant from the same amount of light will be proportional to the gain of photomultiplier [105].

Based on Eq. 4.8 dependency of the gain on the applied voltage can be estimated by formula:

$$g(U) = \alpha \cdot U^b. \quad (4.9)$$

In order to calibrate gains of both detectors, α parameter has to be determined for each detector separately. Series of measurements, were performed by applying the same voltage on both detectors, in the range from 2000 V to 2500 V, with the step of 50 V. For accurate calculation of these parameters, charge values corresponding to both photoelectric peaks were estimated by Gaussian function. In Fig. 4.12 exemplary charge spectra for both detectors measured at the same voltage with fitted Gaussian distribution are presented.

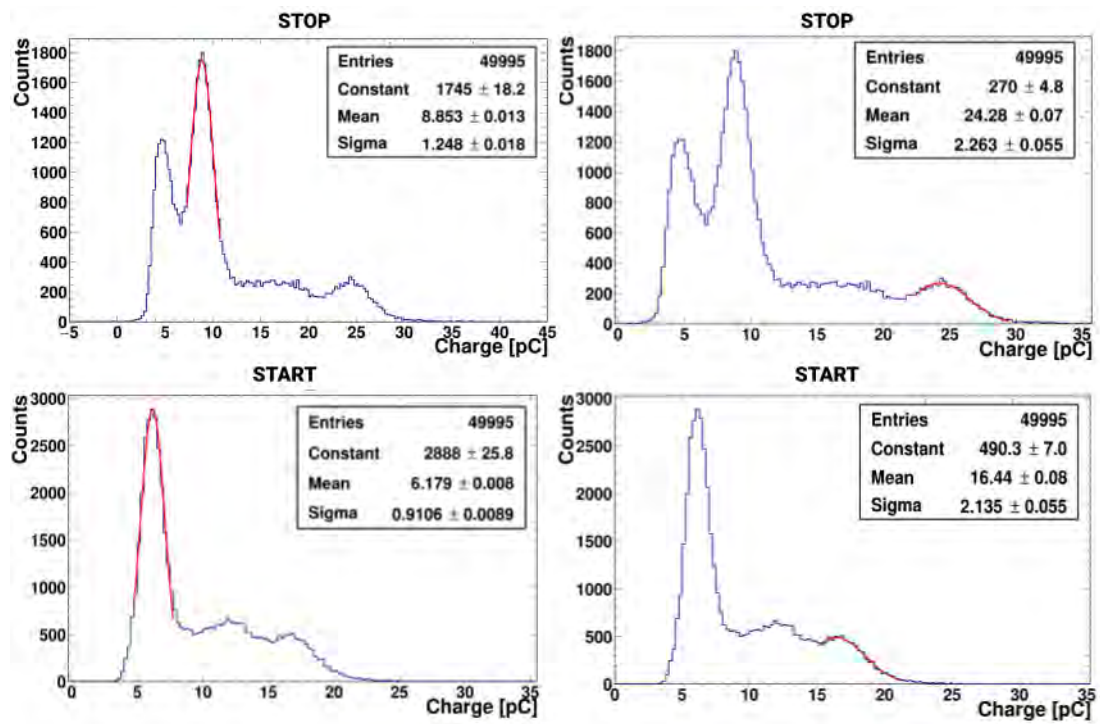


FIGURE 4.12: Exemplary spectra for both detectors represents the result obtained with the supplied voltage of 2350 V with fitted Gaussian distribution.

The dependence of the three following variables were studied as a function of the applied voltage:

- mean of the distribution for 511 keV photoelectric peak

- mean of the distribution for 1274 keV photoelectric peak
- difference between mean values of the distribution for 1274 keV and 511 keV peaks

Dependences of gain vs applied voltage determined for three methods mentioned before are presented in Fig. 4.13.

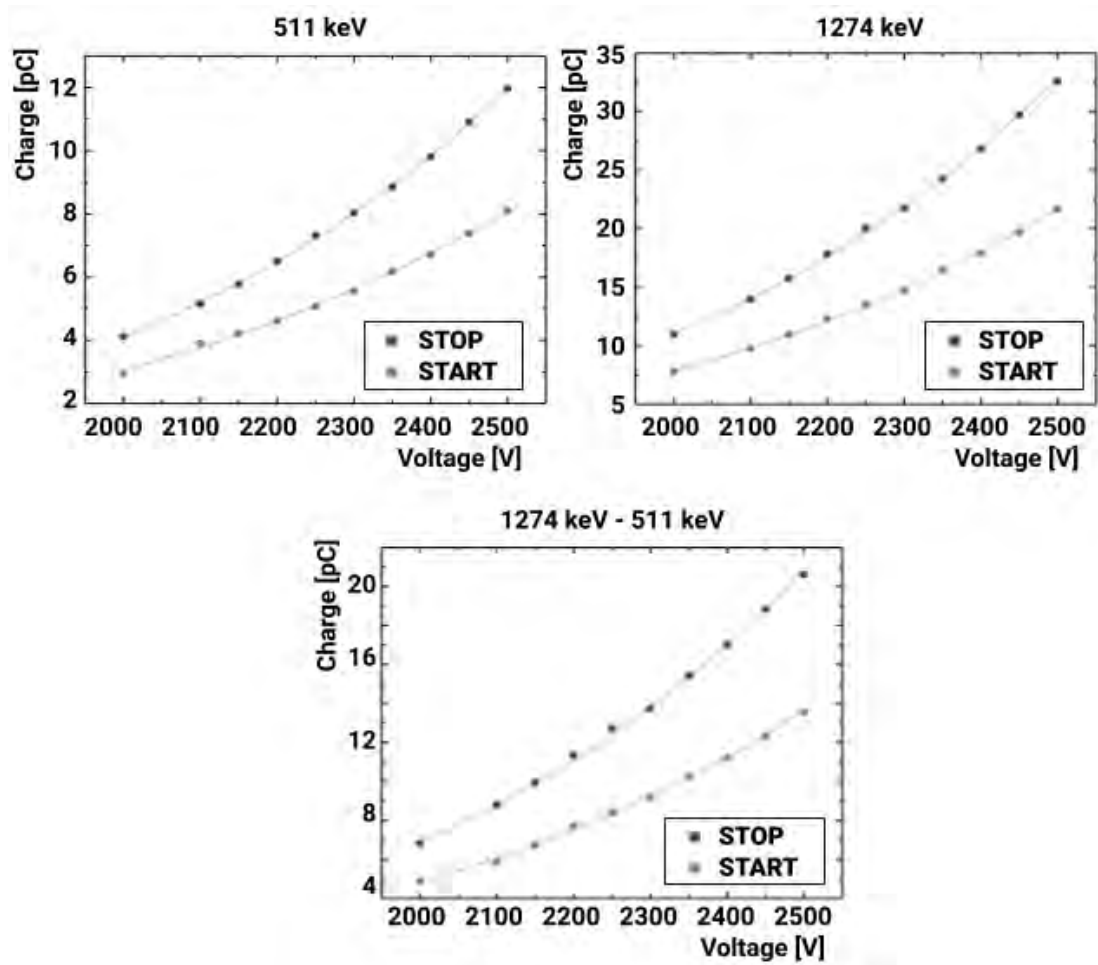


FIGURE 4.13: Dependence of the charge as a function of the applied voltage. Figures show charge at the photopeak corresponding to the 511 keV gamma (upper left), 1274 keV gamma (upper right) and the difference between these charges (lower figure). The superimposed lines indicate results of the fit of Eq.4.9.

Based on Eq. 4.9 voltage for one detector in relation to the other, when $g_1 = g_2$, can be determined as:

$$U_2 = \left(\frac{\alpha_1}{\alpha_2} (U_1)^{b_1} \right)^{\frac{1}{b_2}}. \quad (4.10)$$

As voltage U_1 value of 2300 V was chosen and value of U_2 was calculated as an average of three methods mentioned above.

Calculated values of α parameter, from each fit are presented in Tab. 4.1, together with values of determined supply voltage for both detectors based on Eq. 4.9.

TABLE 4.1: α parameter calculated from 511 keV, 1274 keV photoelectric peak and a difference between the aforementioned, as well as the estimated voltage for both detectors after gain calibration.

	$\alpha_{START} \left[\frac{pC}{V} \right]$	b_{START}	$\alpha_{STOP} \left[\frac{pC}{V} \right]$	b_{STOP}
511 keV	6.09(1.37)E-16	4.80(3)	1.09(93)E-14	4.38(11)
1274 keV	6.93(2.08)E-16	4.91(04)	2.83(1.33)E-15	4.68(06)
1274 keV - 511 keV	2.50(90)E-16	4.98(05)	4.37(3.54)E-16	4.86(10)
	$U_{START}[V]$		$U_{STOP}[V]$	
511 keV	2300		2495	
1274 keV	2300		2500	
1274 keV - 511 keV	2300		2502	
Average	2300		2499	

In Fig. 4.14 energy spectra before (left) and after (right) gain calibration are presented.

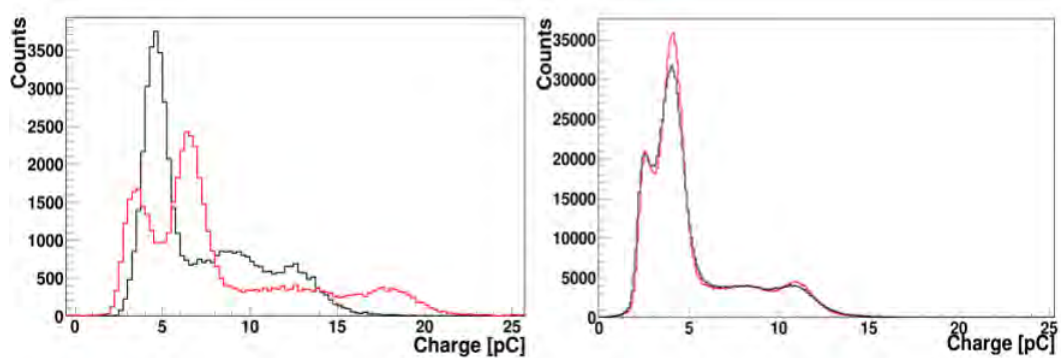


FIGURE 4.14: Charge spectra for both detectors (left) before and (right) after gain calibration.

Since the gain of the detector depends on temperature and can slightly vary in time, before each measurement of the sample, a check-up procedure was developed. Short measurement with the source was performed, and in case the gain of

one detector changed, the applied voltage was adjusted by 10-20 V.

4.5.2 Time resolution determination

In case of lifetime measurements, the time resolution of the detection setup is a crucial parameter, which gives us information about how precisely those lifetimes can be determined. Resolution of the detection setup was determined by measurement of silicon (Si) plates, since in semiconductors, as in metals o-Ps is not created, and only free positron annihilation component is observed [32, 106].

Silicon wafers used in the experiment were boron-doped p-type Si crystals with 0.3 mm thickness, purchased from Sigma Aldrich (Cat. no. 647705-1EA). Measurements were performed at room temperature with Si wafers placed on both sides of the ^{22}Na source in Kapton foil (same as used for other experiments), with polish plane towards the source. The resolution was determined as a sigma (σ) value of the fitted function Eq. 4.7, to the measured time difference spectra in silicon. For each measurement, 1 mln of events were collected. Three consecutive measurements were conducted, and detector resolution was calculated as a weighted mean.

Literature value of mean positron lifetime in pure silicon crystals vary in the range 220 – 260 ps, depending on the type and dopants [107, 108]. It can also be increased, due to the presence of defects and layer of SiO_2 on the wafer surface [109, 110].

In Fig. 4.15 exemplary positron lifetime spectrum of silicon wafers with the fitted model, and in Tab. 4.2 obtained mean lifetime, as well as the resolution of the detection system in sigma in all consecutive measurements, are presented.

TABLE 4.2: Mean positron lifetime for silica wafer and resolution of the detection system in sigma in all consecutive measurements with calculated average values.

Measurement	$\tau_1[ps]$	$\sigma[ps]$
I	280(1)	119(1)
II	280(1)	116(1)
III	277(1)	116(1)
Average	279(1)	117(2)

Obtained results are in agreement with the literature, though measurement was not performed in a vacuum, and silicon wafers were not annealed before the measurement. Determined resolution of the detector is equal to $\sigma = 117(2)$ ps.

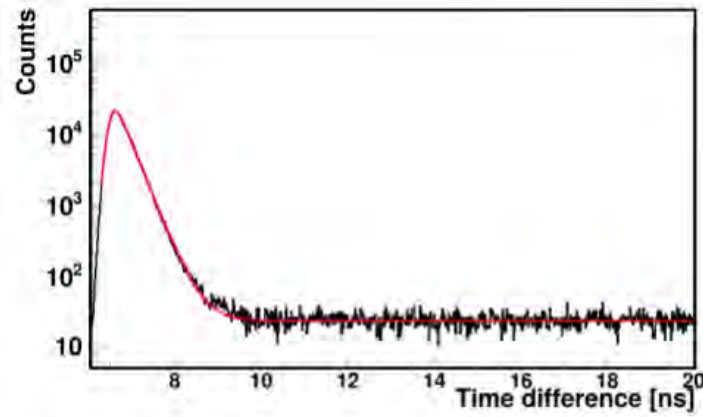


FIGURE 4.15: Exemplary positron lifetime spectrum of silicon wafers with a fitted model.

Chapter 5

Preparation and characterisation of cell lines and tissue

5.1 Tissue specimens

5.1.1 Study group

In case of this study, ten patients were examined. Cardiac myxoma tissues were sectioned and fixed in formalin directly after the surgery, from four patients only. In case of six patients, both myxoma and adipose tissues were sectioned, and these tissues were measure without fixation. Perioperative specimens were obtained from John Paul II Hospital in Kraków with the collaboration of Grzegorz Grudzień, MD. For each patient, a screening interview, laboratory testing (blood counts, metabolic panel, urine test, etc.) and electrocardiogram were completed. Afterwards, the histopathological examination of the extracted tumour was performed. This study was approved by the Bioethical Commission of Jagiellonian University, approval number 1072.6120.123.2017.

5.1.2 PALS - tissue preparation

During surgery, an extracted tumour was aseptically cut into two sections. First one was sent for histopathology examination, the second was placed in a sterile plastic container, filled with formalin (for the fixed specimens) or cell culture medium DMEM, high glucose (Cat. No. 61965026 Gibco™ Paisley, UK) with 10% Foetal Bovine Serum (Cat. No. 10500064 Gibco™ Paisley, UK) and 100 U/mL Penicillin, 100 µg/mL Streptomycin (Cat. No. 15140122 Gibco™ Paisley, UK), 0.25 µg/mL

Amphotericin B (Cat. No. 15290026 Gibco™ Paisley, UK) for non-fixed specimens. After surgery, the samples were transported to the PALS laboratory at the Institute of Physics. Non-fixed tissues were transported and measured within 4 hours after the extraction, and fixed in 10% formalin myxomas were transported and investigated within 48 hours.

Fixed specimens were cut into few pieces, of the same thickness, around 2 mm. The number of fixed samples measured per each patient is presented in Tab 5.1.

TABLE 5.1: The number of fixed samples measured per each patient.

Patient ID	No. of samples per patient	Sample ID
1	6	1-6
2	1	7
3	3	8-10
4	3	11-13

Non-fixed, both myxoma and adipose tissue were cut into two pieces. Photographs of each sample are presented in Fig. 5.1.

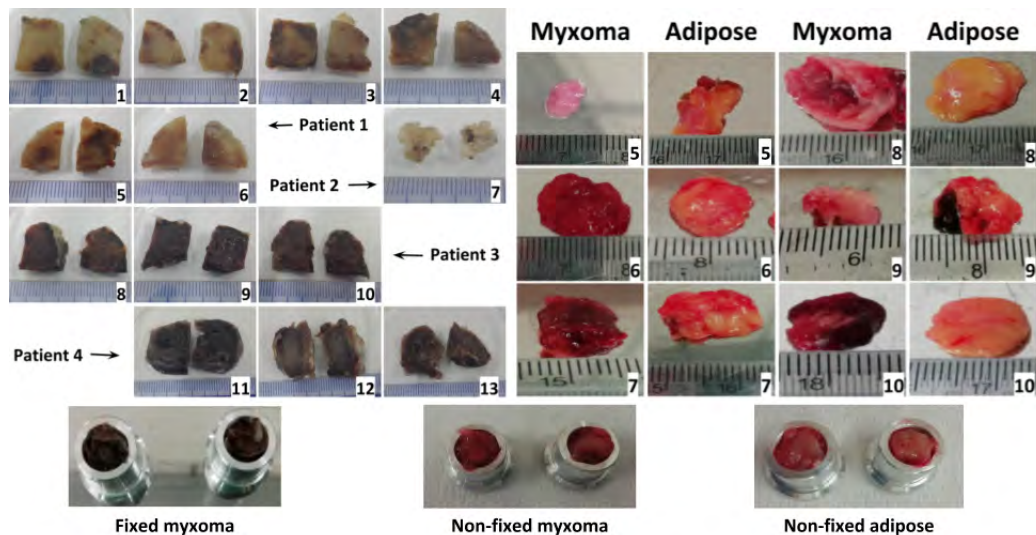


FIGURE 5.1: (upper left) Photographs of fixed Myxoma samples, number on picture indicate sample ID, as in Tab.5.1. Patient ID is given in the white box. (upper right) Photos of non-fixed myxoma and adipose tissue sample, number on picture indicate Patient ID. Ruler below each sample has 1 mm division. (lower panel) Sectioned samples placed in the measurement chamber.

Each sample measured on PALS consisted of two pieces with sodium-22 source between them. All measurements were performed in room temperature. In Fig. 5.2 scheme presenting a workflow of tissue preparation procedure and PALS measurement is shown.

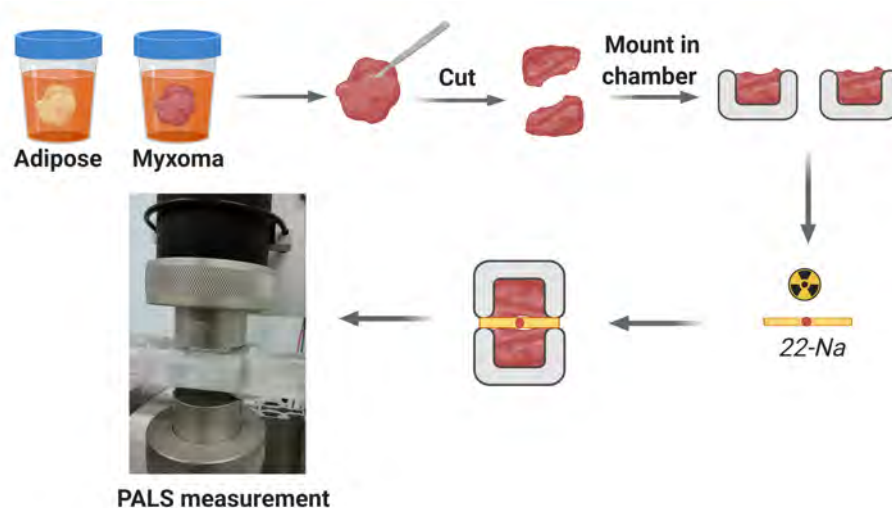


FIGURE 5.2: The workflow of tissue preparation procedure and PALS measurement. Created with BioRender.com

5.2 Cell lines

Research presented in this thesis was conducted on three commercially available cell lines. Two cell lines of melanoma (WM115, WM266-4, obtained from the Department of Glycoconjugate Biochemistry, Institute of Zoology and Biomedical Research of the Jagiellonian University in Kraków [111]) were used as cancerous samples. Line of melanocytes (HEMa-LP obtained from Life Technologies, Paisley, UK) was used as a control. Additionally, cardiac myxoma cells were isolated from perioperative tumours by the enzymatic (Collagenase) digestion method, as a benign tumour sample.

Melanoma WM115 is a primary cell line locally invading with metastatic potential; it is Radial/Vector Growth Phase (RGP/VGP). It was established from a metastatic site (right anterior leg) in a 55-year-old female with superficial spreading melanoma [112]. This cell line features the specific V600D (Val600Asp) mutation at codon 600 in the BRAF gene, a most common mutation responsible for melanoma transformation [76].

Melanoma WM266-4 is a metastatic cell line with epithelial morphology, it is in VGP and was obtained from lymph node metastasis. This line derives from the same patient as WM115, and also features the same mutation in the BRAF gene. This cell line is enriched with $\alpha 5\beta 1$ glycoprotein and has a higher level of $\alpha 2,3$ -linked sialic acid residues. Therefore, it migrates faster and has higher adhesion efficiencies than WM115 [113].

HEMa-LP cell line is human epidermal melanocytes isolated from lightly pigmented (LP) 36-year-old women skin. Melanocytes are present in epidermis and hair follicles are producing melanin (the dark pigment responsible for skin colour) and origin from neural crest cells [79].

Cardiac myxoma cell lines were derived from two patients, 57-year-old men and 59-year-old women. This cells most probably originate from mesenchymal cells capable of endothelial differentiation [88].

5.3 Cell culture

5.3.1 WM115 and WM266-4

Both melanoma cell lines were cultured in RPMI 1640 medium (Cat. No. 21875091 Gibco™ Paisley, UK) supplemented with 10% with Fetal Bovine Serum (Cat. No. 10500064 Gibco™ Paisley, UK), 2mM L-Glutamine (Cat. No. 25030081 Gibco™ Paisley, UK), 100 U/mL Penicillin and 100 $\mu\text{g}/\text{mL}$ Streptomycin (Cat. No. 15140122 Gibco™) and seeded into T75cm² dish and cultured at 37°C and 5% CO₂ atmosphere. Cells were observed daily under a microscope and passaged upon reaching around 80% confluence, by washing flask three times with PBS w/o Ca²⁺, Mg²⁺ (Cat. No. 10010015 Gibco™ Paisley, UK), then incubated with 0.25% Trypsin – EDTA (Cat. No. 25200072 Gibco™ Paisley, UK) for 10 min, inactivated in medium with serum and transferred to a conical tube and centrifuged in 260g for 10 min. Pellet was then suspended in fresh medium, cells were counted with Trypan Blue dye by Automatic Cell Counter LUNA II and seeded to new flasks at an appropriate density.

5.3.2 HEMa-LP

The melanocyte cell line was cultured in M254 medium (Cat. No. M254500 Gibco™ Paisley, UK) with Human Melanocyte Growth Supplement-2 (Cat. No. S0165 Gibco™ Paisley, UK), 100 U/mL Penicillin and 100 µg/mL Streptomycin (Cat. No. 15140122 Gibco™) and seeded into T75cm² dish and cultured at 37°C and 5% CO₂ atmosphere. Cells were observed daily under a microscope and passaged upon reaching around 80% confluence, by incubation with 0.025% Trypsin – EDTA (Cat. No. R-001-100 Gibco™ Paisley, UK) for 3 min, inactivated with Trypsin Neutralizer solution (Cat. No. R-002-100 Gibco™ Paisley, UK) transferred to a conical tube and centrifuged at 180g for 7 min. Pellet was then suspended in fresh medium, cells were counted with Trypan Blue dye by Automatic Cell Counter LUNA II and seeded to new flasks at appropriate density $5 * 10^4 \text{cells/cm}^2$.

5.3.3 Cardiac Myxoma

In case of non-fixed samples of cardiac myxoma from two of them, which were sufficiently large, cell cultures were derived. Tissue was aseptically dissected, and part designated for cell isolation was placed in a petri dish in medium DMEM, high glucose (Cat. No. 61965026 Gibco™ Paisley, UK) with 10% FBS (Cat. No. 10500064 Gibco™, Paisley, UK), 2mM L-Glutamine (Cat. No. 25030081 Gibco™ Paisley, UK), 100 U/mL Penicillin and 100 µg/mL Streptomycin (Cat. No. 15140122 Gibco™, Paisley, UK), 0.25 µg/mL Amphotericin B (Cat. No. 15290026 Gibco™, Paisley, UK) and 200 U/mL Collagenase II (Cat. No. 17101015 Gibco™, Paisley, UK) for 48 h. Then tissue with the medium was squeezed through 70 nm nylon mesh, to isolate cells from the extracellular matrix, centrifuged at 260g for 10 min. Cells were seeded on T75cm² culture dish and cultured at 37°C and 5% CO₂ atmosphere. After 24 h myxoma cell started attaching to dish bottom, cells were washed daily with PBS w/o Ca²⁺, Mg²⁺ (Cat. No. 10010015 Gibco™ Paisley, UK) to wash out present erythrocytes for 7 days. Upon that cells were passaged by washing flask three times with PBS w/o Ca²⁺, Mg²⁺, then incubated with 0.25% Trypsin – EDTA (Cat. No. 25200072 Gibco™ Paisley, UK) for 10 min, and removed from a flask with a cell

scraper, inactivated in medium with serum and transfer to a conical tube and centrifuged at 260g for 10 min. Pellet was then suspended in fresh medium, cells were counted with Trypan Blue dye by the Automatic Cell Counter LUNA II and seeded to flasks at an appropriate density. Myxoma cells grow very slowly, seeded at the density $2.5 \times 10^5 \text{ cells/cm}^2$, the lined reached 80% confluence after 50 days.

In Fig. 5.3 scheme presenting a workflow of myxoma cell culture isolation, and later PALS measurement is shown.

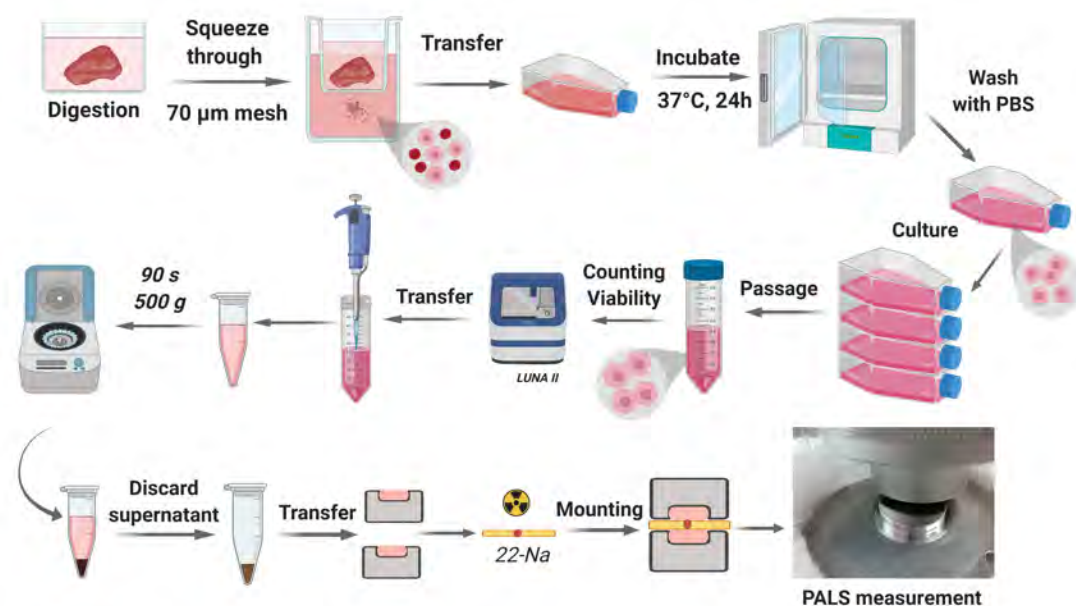


FIGURE 5.3: The workflow of myxoma cell culture isolation and PALS measurement. Created with BioRender.com

5.4 Cell lines preparation for PALS

5.4.1 Freeze-drying

Freeze-drying was done for three cell lines (HEMa-LP, WM115, WM266-4) to study the role of water on the positronium lifetime.

Cells were freeze-dried in five different media, including a standard freezing medium containing (DMSO) - dimethylsulfoxide (CAS. 67-68-5, Sigma Aldrich) and other cryoprotectants, such as D-trehalose (Cas. 6138-23-4, Sigma Aldrich) and (PROH) 1,2 -propanediol (CAS. 57-55-6, Sigma Aldrich), as a control PBS was used [114,115]. Formulation of used media was:

1. RPMI 1640/M254 + 20% FBS + 10% DMSO.
2. 10% DMSO in PBS w/o Ca^{2+} , Mg^{2+} .
3. PBS w/o Ca^{2+} , Mg^{2+} .
4. 1.5 M PROH + 0.5 M D-trehalose in PBS w/o Ca^{2+} , Mg^{2+} .
5. 0.25 M D-trehalose in PBS w/o Ca^{2+} , Mg^{2+} .

In Fig. 5.4 scheme presenting workflow of cells freeze-drying procedure and PALS measurement is shown.

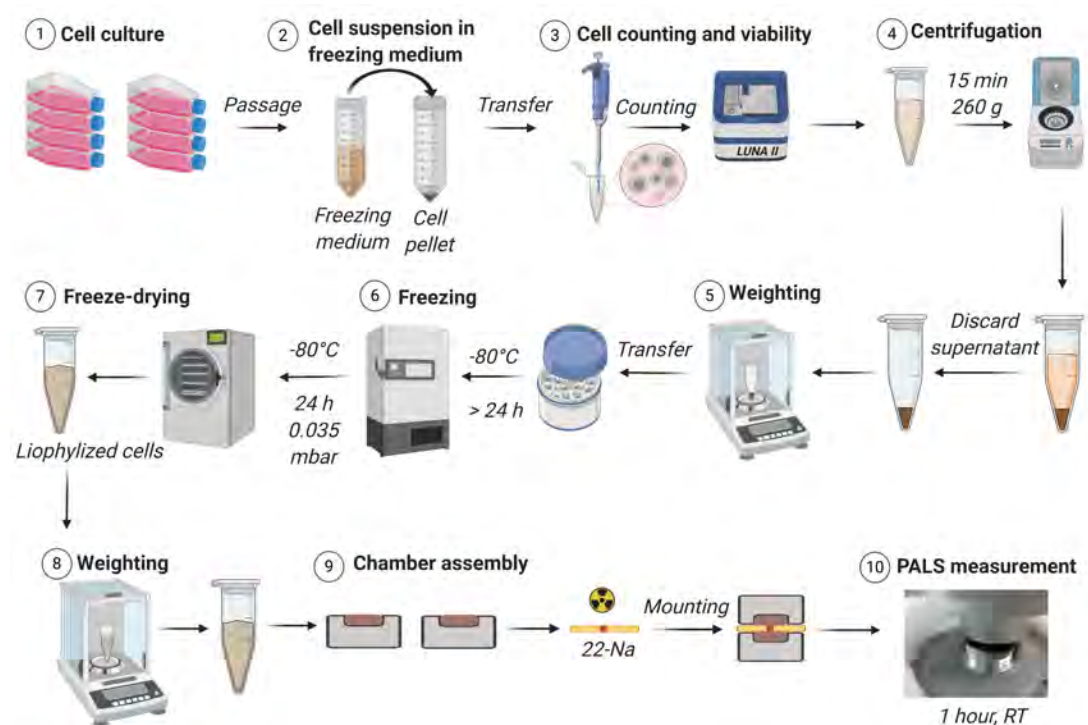


FIGURE 5.4: Scheme presenting workflow of cells freeze-drying procedure and PALS measurement.

For each sample, cells from six T75 cell culture flasks were harvested after reaching 90% of confluence, which resulted in around 60 mln cells for both melanoma lines, and 30 mln for melanocytes. Cells were resuspended in given freeze-drying medium and transferred to a 5 mL eppendorf vial, then spun down at 260g for 15 min. The supernatant was removed, and a cell pellet was firstly frozen at -80°C and then cell were freeze-dried for 24 h in vacuum conditions (0.0375 mbar) at -80°C using the Labconco FreeZone 2.5 freeze-drier. Each sample was weighted before and

after freeze-drying, in order to calculate water mass loss. Samples were sealed with parafilm and stored in a desiccator at 4°C prior and after the measurements.

5.4.2 Rehydration

In order to check the number of living cells, cells were rehydrated after completing measurements. Cells in eppendorf vial were taken out of a desiccator and warmed up to room temperature, before rehydration. Firstly, 50 μL of distilled water by 10 μL droplets was added, then 2 mL of culture medium for a given cell line warmed to 37°C. Cells were resuspended in culture medium and incubated for 5 min. After incubation, viability was tested with trypan blue, and compared with those calculated before freezing.

In Fig. 5.5 scheme presenting workflow of rehydration procedure is shown.

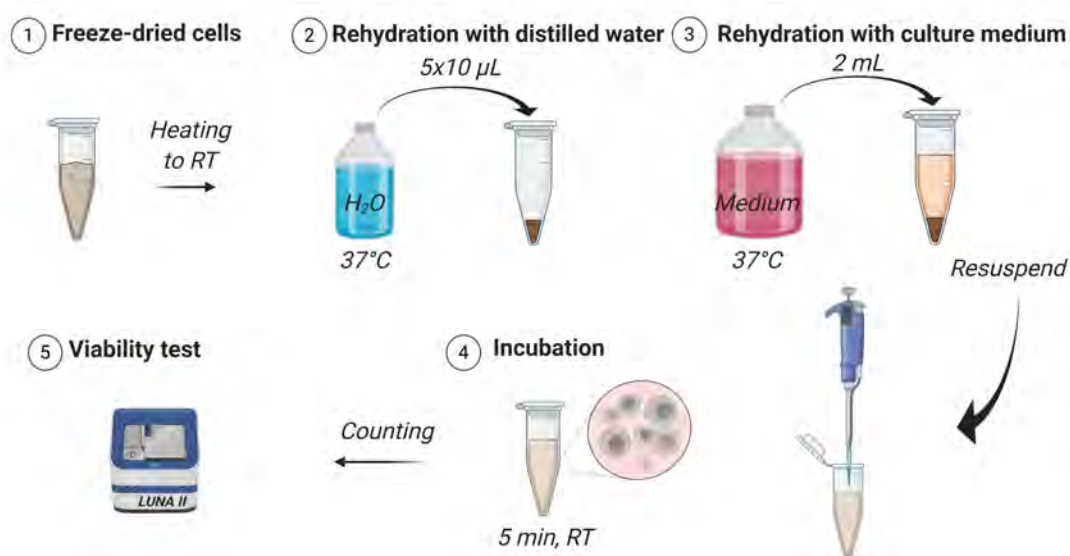


FIGURE 5.5: Scheme presenting workflow of rehydration procedure. Created with BioRender.com

5.4.3 Living cells preparation

PALS measurement was performed on living cells, harvest upon reaching > 90% confluence from eight T75 cell culture flasks, which resulted in around 100 mln cells for both melanoma lines and around 75 mln for melanocyte. Cells were passaged in a standard way after centrifugation cells were resuspended in medium, counted, and its viability was determined with trypan blue assay. Next cell suspension was

transferred to 1.5 mL eppendorf tubes and centrifuged at 500g for 90 s. The supernatant was discarded, and a cell pellet was transferred to a given measurement chamber with a spatula. Viability test was done before and after each measurement to confirm, whether setup conditions and cells handling were appropriate for the culture, and not influenced the results by the high percentage of dead cells.

In Fig. 5.6 scheme presenting workflow of living cell preparation procedure and PALS measurement is shown.

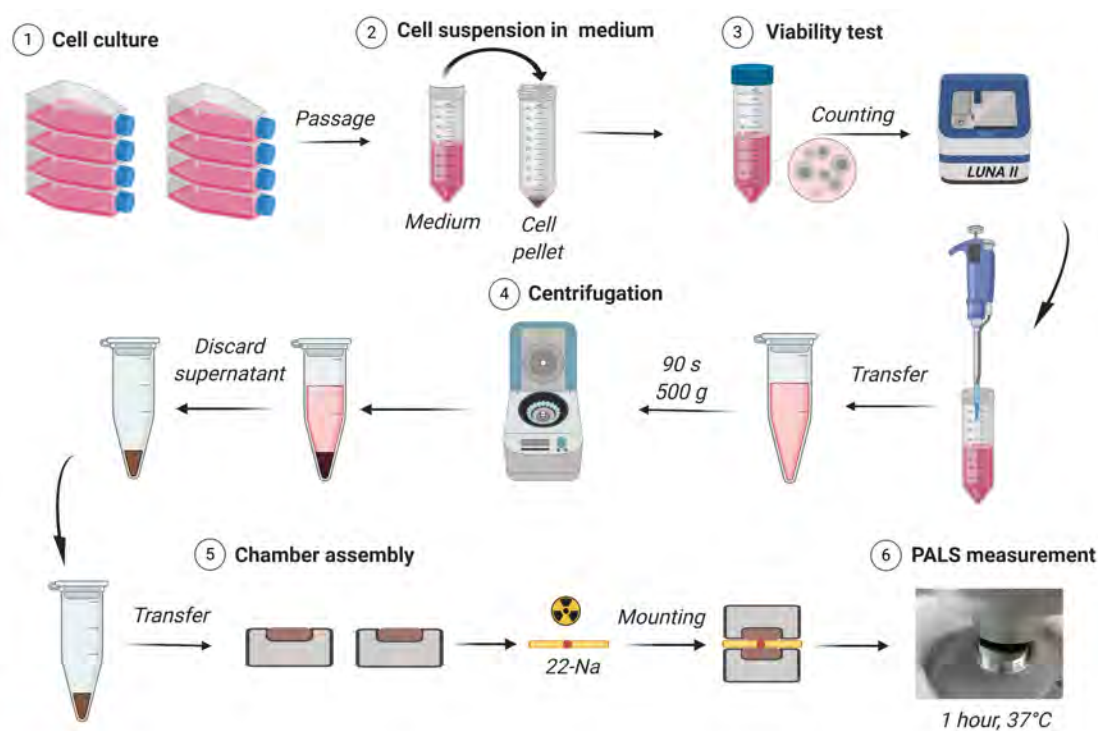


FIGURE 5.6: Scheme presenting workflow of living cell preparation procedure and PALS measurement. Created with BioRender.com

5.5 Optical and confocal microscopy

Cell morphology was checked daily employing Nikon Eclipse TS100 inverted optical microscope, photos presented in this thesis were taken with camera Nikon DS-Fi1c and were processed with Nikon NIS-Elements - Imaging Software.

Confocal microscopy studies for cardiac myxoma cell culture were performed on Zeiss Axio Observer Z.1 with LSM 710 confocal module for cells stained with DAPI (Cat. No. 62248 Pierce™ Paisley, UK) for nucleus and Alexa Fluor™ 647 Phalloidin (Cat. No. S32357 Invitrogen™ Paisley, UK) for F-Actin. Immunofluorescence

staining was done with VE-cadherin (BV9) Antibody (Cat. No. sc-52751, Santa Cruz Biotechnology, Inc.'s, US) and as a secondary antibody goat anti-mouse IgG-FITC: (Cat. No. sc-2010, Santa Cruz Biotechnology, Inc.'s, US) with fluorescein isothiocyanate.

In Fig. 5.7 scheme presenting workflow of myxoma cell culture staining for confocal microscopy is presented.

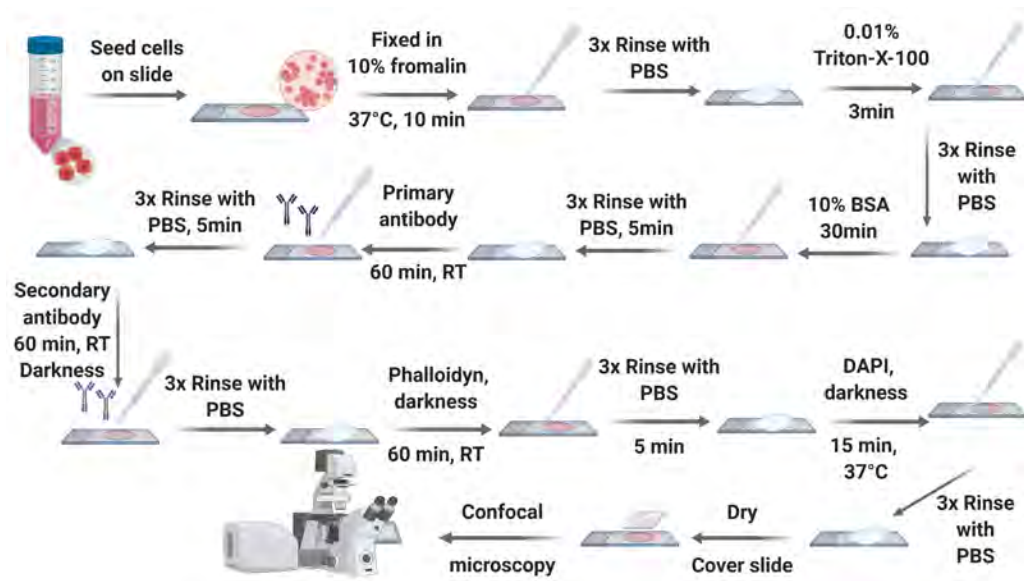


FIGURE 5.7: Workflow of myxoma cell culture staining for confocal microscopy. Created with BioRender.com

Before staining, cells were fixed in 10% formalin for 10 min at 37°C and rinsed 3x with cold PBS w/o Ca^{2+} , Mg^{2+} after each step of staining, and then incubated with 0.01% Triton X-100 solution for 3 min, rinsed with PBS again 3 times. Staining cells for cadherins was done by incubation for 60 min in the primary antibody, at a concentration of 5 $\mu\text{g}/\text{mL}$ VE-cadherin (BV9) in 1.5% BSA. Incubation with secondary antibody was performed in the same concentration as a primary antibody.

Secondly, F-actin was stained with phalloidin in concentration 5 μL per 200 μL of PBS and 10% of BSA and incubated for 60 min in room temperature in the dark. At last, cells were stained in 300 μM DAPI solution. Obtained images were processed with ZEN lite software.

5.6 Nuclear Magnetic Resonance

Hydration of freeze-dried in different media cell lines was studied by means of Nuclear Magnetic Resonance (NMR). 1H – NMR spectra were acquired using a Bruker Avance III 300 spectrometer (Bruker Biospin), operating at the resonance frequency 300MHz for protons (at $B_0 = 7 T$), with the transmitter power, equal to 400W ($\frac{\pi}{2} = 1.5 \mu s$, dead time 7.5 μs , repetition time 2 s) in the frequency domain and signals were acquired by TopSpin 3.5pl7 software. Forty acquisitions were made, and the resulting spectrum was a Fourier transform of the measured signal. The total measurement time was about 2 min. All measurements were conducted at room temperature, lyophilised samples were placed in thin glass capillary with 5 mm diameter. Obtained spectra were analysed with Origin 8.0 software.

In Fig. 5.8 scheme workflow of NMR measurement and freeze-dried WM266-4 cells in capillary are presented.



FIGURE 5.8: Scheme presenting workflow of NMR measurement. Freeze-dried WM266-4 cells in the capillary for NMR studies. The number on capillary denotes given freezing medium as in 5.4.1. Created with BioRender.com

5.7 Electron Paramagnetic Resonance

Melanin concentration in HEMa-LP, WM115 and WM266-4 cell line was determined by means of Electron Paramagnetic Resonance (EPR). Signals of melanins were obtained using Bruker EMX-AA spectrometer working in X-Band (9.5 GHz).

L-DOPA melanin synthesised by autooxidation of DOPA in a concentration equal to 0.575 mg/mL was used as reference material (standard), and PBS was used as a blank sample and later extracted from each spectrum as a background.

In Fig. 5.9 scheme presenting workflow of EPR studies is shown.

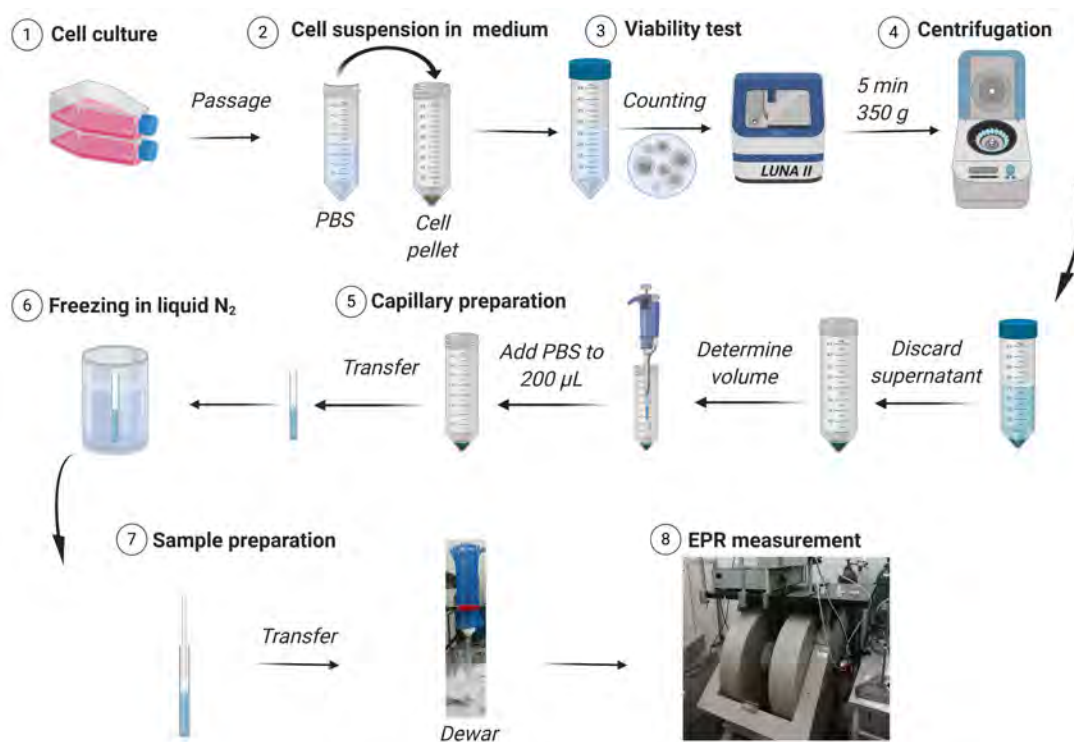


FIGURE 5.9: Scheme presenting workflow of EPR measurement and sample preparation. Created with BioRender.com

Two samples from each cell line with 7 and 14 mln cells/sample were prepared. Cells were harvested with standard procedure, counted by Hemocytometer, then given a number of cells suspended in PBS w/o Ca^{2+} , Mg^{2+} were transferred to conical tube and centrifuge at 350g for 5 min. The volume of cell pellet was determined by pipette, and PBS w/o Ca^{2+} , Mg^{2+} was added in a way that total sample volume was 200 μL . The cell suspension was transferred to a 4.9 mm diameter glass tube sealed with Parafilm at one end. Samples prepared in this way were slowly immersed in liquid nitrogen.

Just before EPR measurement, the tube was removed from liquid nitrogen, warmed gently in hands, so the frozen sample could be pushed out with a glass rod to a quartz dewar filled with liquid nitrogen. This vessel was placed in the cavity of the resonator and flushed with nitrogen to prevent water vapour condensation on the dewar.

Signal of melanin radical centres was recorded with the following parameters: magnetic field centre - 336.191 mT , microwave frequency - 9.45 GHz , microwave

power - $33 \mu W$, modulation amplitude - $0.305 mT$, conversion time - $41 ms$. Ten independent spectra for each sample was registered. Resultant one was obtained as an averaged from all measured, after subtracting the PBS spectrum as a background. Then double integral from the average spectrum was calculated. All operations from freezing samples, including measurements, were taken in twilight to avoid photoexcitation of melanin signal.

Part III

Experimental Results

Chapter 6

Cardiac Myxoma

6.1 Clinical characteristics of study group

Clinical characteristics of a study group are presented in Tab. 6.1. The group is consisted of 4 men and 6 women, in age over 50. The mean age at diagnosis, estimated as an average with standard deviation, was 67(12) for women and 60(2) for men. Also, given the age, most of the patients had multiple comorbidities, both metabolic and cardiovascular.

Micrograph showing exemplary histopathology finding of cardiac myxoma, for case 6 and 7, with haematoxylin and eosin stain is presented in Fig. 6.1. Myxoma cells - stained in purple (marked with blue arrow) - can be shaped as stellate (case 7) or globular (case 6), red/orange structures (marked with white arrow) are present blood vessels with erythrocytes, and surrounding myxoid matrix is stained in pink (marked with green arrow).

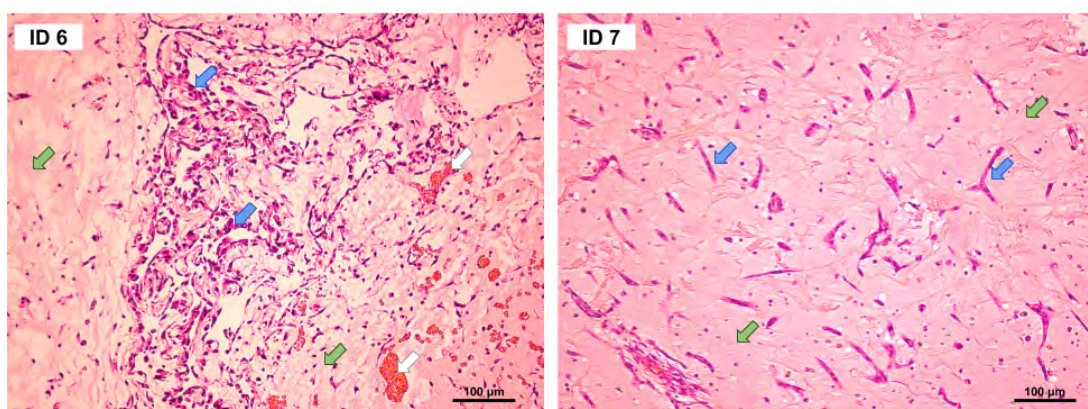


FIGURE 6.1: Micrograph showing histopathology finding of cardiac myxoma for case 6 and 7 with haematoxylin and eosin stain.

TABLE 6.1: Clinical characteristics of a study group.

Patient ID	Sex	Age	Metabolic disease	Cardiovascular disease	Diabetes
1	F	72	hypercholesterolaemia	hypertension	-
2	M	60	hypercholesterolaemia	Myocardial infarction, Raynaud's syndrome	-
3	M	58	hypercholesterolaemia	multilevel atherosclerosis	type II
4	F	54	hypercholesterolaemia	hypertension	type II
5	F	78	hyperlipidaemia	hypertension, Ischaemic heart disease, patent foramen ovale	-
6	M	57	extreme obesity	hypertension, paroxysmal atrial fibrillation	-
7	F	59	-	hypertension, Ischaemic heart disease	type II
8	F	84	hypercholesterolaemia, gout	hypertension, paroxysmal atrial fibrillation, varicose veins, ischaemic heart disease	-
9	F	52	-	-	-
10	M	64	hypercholesterolaemia, chronic renal failure	fixed atrial fibrillation, peripheral atherosclerosis, congestive heart failure	-

In Tab. 6.2 tumour characteristics and histopathology result is presented. In all cases, patients were diagnosed by transthoracic echocardiography (TTE). Therefore, the structure type was confirmed postoperatively through a histopathological examination of the specimen. For all patients, it was a single tumour: for 9 patients localized in the left atrium and for 1 in the right atrium. In 70% it occurs as a solid type and as a papillary in 30%.

TABLE 6.2: Histopathology results and tumour characteristic of a study group. TTE- transthoracic echocardiography.

Patient ID	Diagnosis method	Tumour localization	Tumour type	Tumour size [cm]	Histopathology
1	TTE	Left artium	solid	5x4	myxoma
2	TTE	Left artium	papillary	4x1.5	myxoma
3	TTE	Left artium	solid	5x2	myxoma
4	TTE	Right artium	solid	5x5	myxoma
5	TTE	Left artium	solid	3x3	myxoma
6	TTE	Left artium	papillary	8x3	myxoma
7	TTE	Left artium	papillary	6x5	myxoma
8	TTE	Left artium	solid	3.5x2.5	myxoma
9	TTE	Left artium	solid	3x2	myxoma
10	TTE	Left artium	solid	2x2	myxoma

6.2 Fixed tissues studies

The first part of the experiment was focused on studying fixed tissues, where the influence of tissue decomposition in time is not affecting results. Sectioned fixed tissues from four patients were measured by means of Positron Annihilation Lifetime Spectroscopy. Exemplary positron lifetime spectra for one of the samples with fitted model and components related to annihilation type are presented in Fig. 6.2.

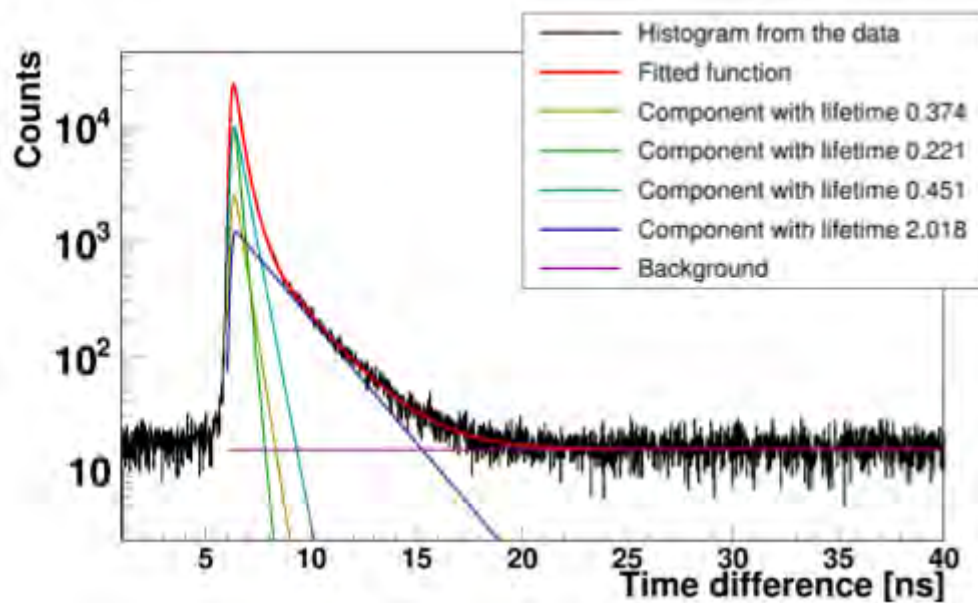


FIGURE 6.2: Exemplary PAL spectrum (obtained for patient no. 1, sample no. 5) for fixed myxoma sample. Superimposed lines indicate distributions of particular components resulting from the fit of Eq. 4.5. Green - para-Positronium, yellow - annihilation in the source material, turquoise - free positron annihilation, blue - ortho-Positronium, purple - background. The spectra do not start at zero because of the time offset between the detectors.

Results for all observed components with the average value calculated for sections of a given patient are presented in Tab. 6.3. For average value, uncertainty is calculated as standard deviation, while for a given component, it is noted as statistical uncertainty of the fit. The obtained mean lifetime of o-Ps is consistent between sections of one specimen as well as between tumours of different patients with an average value of 2.01(02) ns.

TABLE 6.3: Mean positronium lifetime and intensity values with average value calculated for sections of given patient for fixed myxoma tissues. For average value uncertainty is calculated as standard deviation, while for given component it is noted as statistical uncertainty of the fit. Patients and samples ID annotations are described in Tab. 5.1 and Tab. 6.1.

Patient ID	Sample ID	$\tau_1[ns]$	$I_1[\%]$	$\tau_2[ns]$	$I_2[\%]$	$\tau_3[ns]$	$I_3[\%]$
1	1	0.232(01)	31.4(1)	0.459(01)	48.1(1)	2.01(01)	20.5(1)
	2	0.232(01)	28.6(1)	0.446(01)	50.9(1)	1.99(1)	20.6(1)
	3	0.216(01)	24.9(1)	0.434(01)	53.6(1)	1.99(1)	21.5(1)
	4	0.242(01)	35.0(1)	0.454(01)	45.0(1)	2.00(1)	20.0(1)
	5	0.221(01)	31.9(1)	0.451(01)	48.3(1)	2.02(1)	19.8(1)
	6	0.213(01)	33.6(1)	0.458(01)	47.9(1)	2.03(1)	18.5(1)
	Average	0.258(12)	39.3(3.8)	0.477(12)	40.6(3.5)	2.01(02)	20.1(9)
2	7	0.245(10)	38.9(1)	0.476(01)	41.7(1)	2.01(01)	19.4(1)
3	8	0.208(01)	29.0(1)	0.440(01)	52.0(1)	2.02(1)	19.0(1)
	9	0.237(01)	34.4(1)	0.468(01)	45.8(1)	2.01(1)	19.9(1)
	10	0.226(01)	28.1(1)	0.443(01)	51.1(1)	1.98(1)	20.8(1)
	Average	0.255(17)	38.5(3.4)	0.476(16)	41.8(3.9)	2.01(01)	19.8(6)
4	11	0.258(01)	38.5(1)	0.486(1)	41.3(1)	2.02(1)	20.1(1)
	12	0.228(01)	29.4(1)	0.453(01)	50.1(1)	2.02(1)	20.4(1)
	13	0.230(01)	30.6(1)	0.453(01)	49.1(1)	2.02(1)	20.3(1)
	Average	0.270(17)	41.7(6.4)	0.497(32)	38.1(6.2)	2.02(01)	20.2(2)

Determined values of mean ortho-positronium lifetime and intensity are shown in Fig. 6.3.

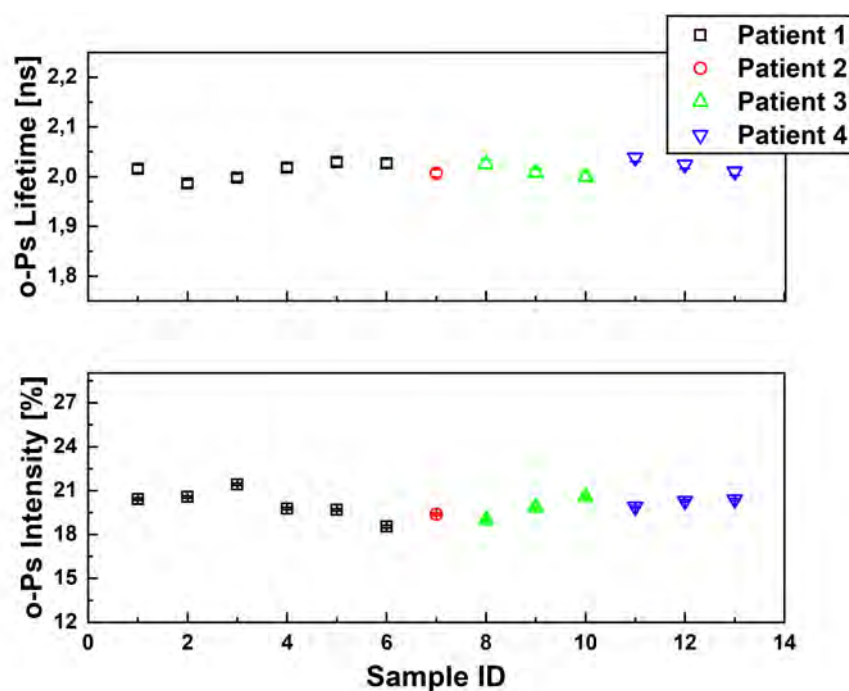


FIGURE 6.3: Ortho-positronium mean lifetime (upper) and intensity (lower panel) for sectioned cardiac myxoma fixed tissues. Patients and samples ID annotations are described in Tab. 5.1 and Tab. 6.1.

Slight differences between o-Ps intensity are observed between sections of a specimen, origination possibly from the heterogeneity of the tumour. Nevertheless, values are consistent from patient to patient with an average value of 2.01(01) ns 19.9(5)% for mean o-Ps lifetime and intensity, respectively. Since myxoma tumour does not have a homogeneous structure, possible differences between sections from one specimen as well as between specimens in different patients were studied.

6.3 Comparison of cardiac myxoma vs normal tissue

Comparison of positronium lifetime between cardiac myxoma and normal tissue is crucial for validation of positronium application as a novel biomarker. In this case, non-fixed specimens of cardiac myxoma, as a benign tumour, and mediastinal adipose tissue, as a control (normal tissue) sectioned from the same patient were studied by means of PALS. Samples were studied without fixation, to exclude formalin

impact on the positronium lifetime and immediately after surgery, to avoid the influence of tissue decomposition in time. Exemplary positron lifetime spectra for one of the samples with fitted model and components related to annihilation type are presented in Fig. 6.4.

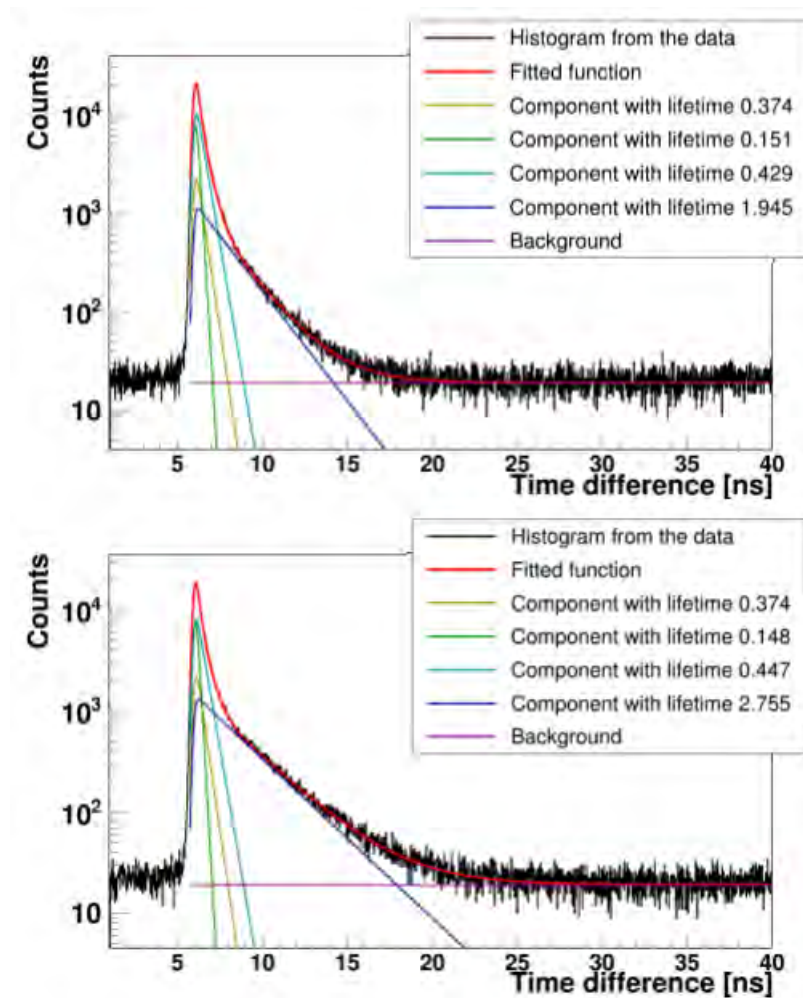


FIGURE 6.4: Exemplary PAL spectrum (obtained for patient no. 6) for non-fixed myxoma (upper) and adipose (lower). Superimposed lines indicate distributions of particular components resulting from the fit of Eq. 4.5. Green - para-Positronium, yellow - annihilation in the source material, turquoise - free positron annihilation, blue - ortho-Positronium, purple - background. The spectra do not start at zero because of the time offset between the detectors.

Results for all observed components with the average value calculated for myxoma and adipose specimens are presented in Tab. 6.4. For average value, uncertainty is calculated as standard deviation, while for the given component, it is noted as statistical uncertainty of the fit. Obtained mean lifetime and intensity of ortho-positronium are significantly different between myxoma and adipose tissue of the same patient with an average difference equal to 0.8 ns and 10.7%, respectively.

TABLE 6.4: Mean positronium lifetime and intensity values for non-fixed myxoma and adipose tissues. For average value, uncertainty is calculated as standard deviation, while for the given component it is noted as statistical uncertainty of the fit. Patients ID annotations are described in Tab. 6.1.

	Patient ID	$\tau_1[ns]$	$I_1[\%]$	$\tau_2[ns]$	$I_2[\%]$	$\tau_3[ns]$	$I_3[\%]$
Myxoma	5	0.180(01)	45.2(1)	0.441(02)	40.1(1)	1.89(1)	14.7(1)
	6	0.151(01)	25.1(1)	0.429(01)	55.5(1)	1.95(1)	19.4(1)
	7	0.157(02)	17.8(1)	0.415(01)	61.5(1)	1.89(1)	20.7(1)
	8	0.120(01)	18.0(1)	0.412(01)	61.9(1)	1.93(1)	20.2(1)
	9	0.135(01)	21.0(1)	0.407(01)	60.5(1)	1.95(1)	18.5(1)
	10	0.158(01)	26.2(1)	0.426(01)	56.6(1)	1.93(1)	17.1(1)
	Average	0.150(19)	25.6(9.3)	0.421(12)	56.0(7.5)	1.92(02)	18.4(2.0)
Adipose	5	0.187(02)	34.1(1)	0.477(2)	39.0(1)	2.63(1)	26.9(1)
	6	0.148(01)	24.4(1)	0.447(02)	44.7(1)	2.75(1)	30.9(1)
	7	0.181(01)	26.6(1)	0.451(02)	44.5(1)	2.68(1)	28.9(1)
	8	0.164(01)	26.2(1)	0.443(01)	45.3(1)	2.72(1)	28.5(1)
	9	0.172(01)	28.5(1)	0.453(02)	43.1(1)	2.74(1)	28.4(1)
	10	0.148(01)	22.1(1)	0.437(01)	46.7(1)	2.76(1)	31.2(1)
	Average	0.167(15)	27.0(3.8)	0.451(12)	43.9(2.4)	2.72(05)	29.1(1.5)

Simultaneously, ortho-Positronium mean lifetime for both myxoma, as well as, adipose tissue is consistent between different patients with an average value

of 1.92(02) ns and 2.72(05) ns, respectively. Slight differences between o-Ps intensity are observed between different patients, as it was in case of fixed tissues, with average values equal to 18.4(2.0)% and 29.1(1.5)% for myxoma and adipose tissue, respectively.

Determined values of mean ortho-positronium lifetime and intensity for myxoma and adipose tissue are presented in Fig. 6.5. Observed differences between two types of tissue, myxoma and adipose, are significantly higher, than differences in the same tissue type from patient to patient, both in case of fixed as non-fixed specimens. Demonstrating that variation of mean positronium lifetime and intensity, originating from the heterogeneous structure of tissue, or diversity in the study group is not significant for the result, and even so, allows to differentiate between tumour and normal tissue.

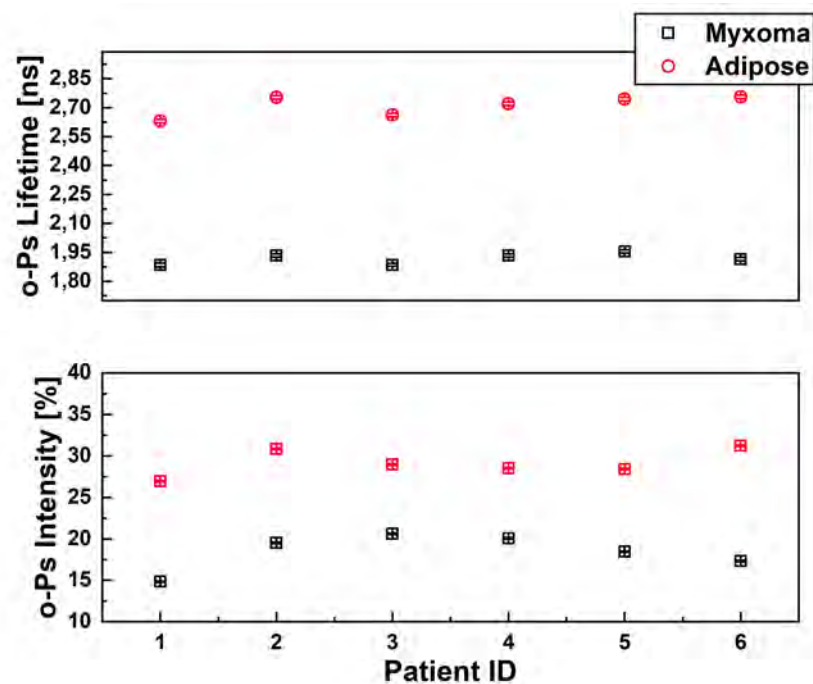


FIGURE 6.5: Ortho-positronium mean lifetime (upper) and intensity (lower) for non-fixed cardiac myxoma and adipose tissues. Patients ID annotations are described in Tab. 6.1.

6.4 Cardiac Myxoma cell culture

Primary myxoma cultures were established from two patients, to compare positronium lifetime between myxoma tissue and cells. Since tumour tissue consists not only

from myxoma cells but also matrix and blood vessels, it is important to examine, if they interfere with the resulting lifetime of positronium. Micrograph of isolated cell culture upon seeding, 24h later, 72 h later and secondary culture are presented in Fig. 6.6, for patients 6 and 7.

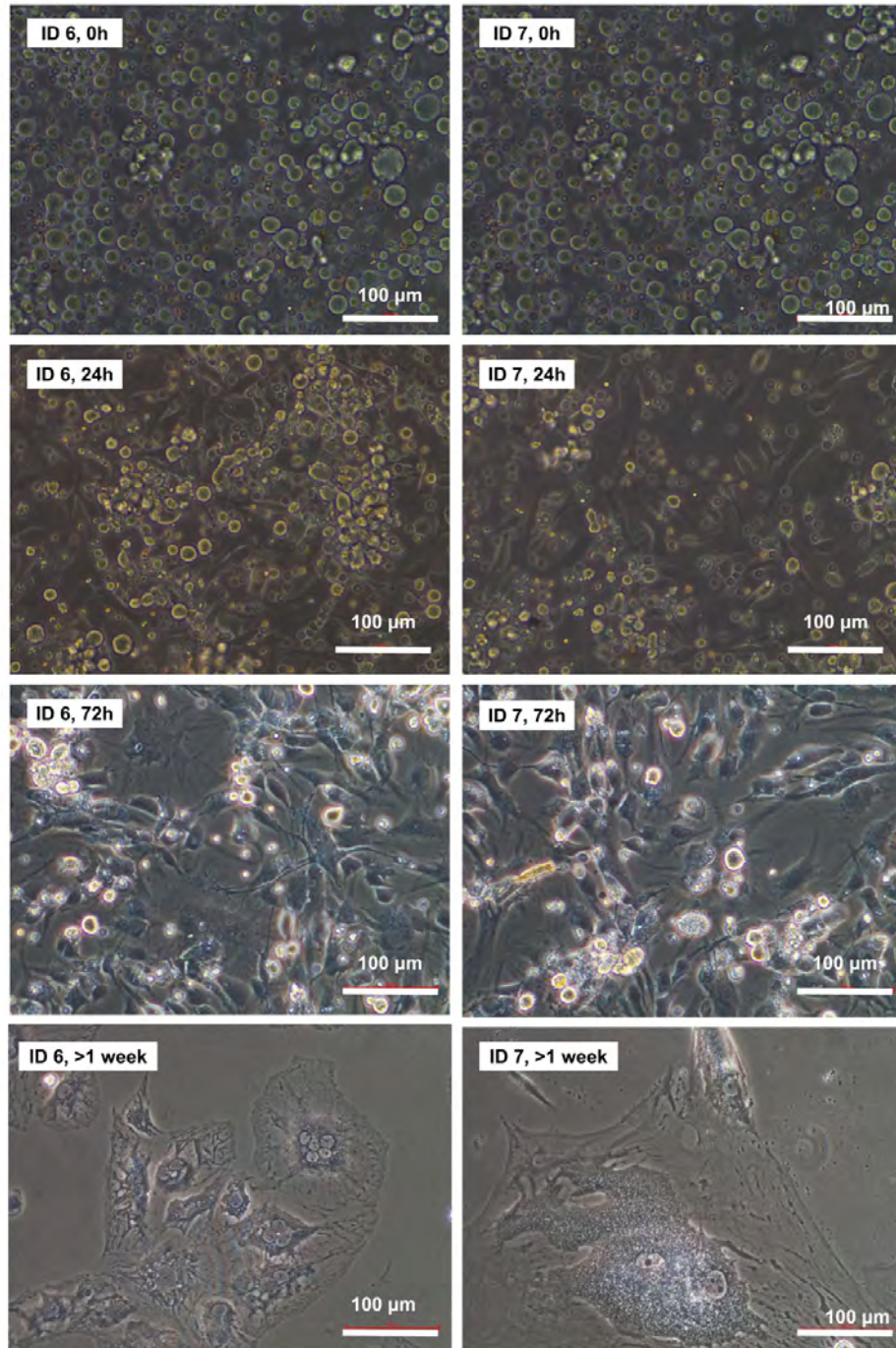


FIGURE 6.6: Primary culture of cells isolated from cardiac myxoma, upon seeding, 24h later, 72 h later with erythrocyte contamination. Secondary culture after 1st passage (lower) for case 6 and 7. Scale bar has 100 μm.

In the upper panel, floating cells (bigger ones) are observed together with present erythrocytes (smaller ones). Myxomas are adherent and relatively big cells with visible multiple nuclei, and one can observe that after attaching to the surface cells are significantly bigger than, floating spherical forms, since attached cells are flattening on the surface and its thickness can be even below a micrometre.

To determine whether isolated myxoma cells, are short of fibroblasts or other types of cells, confocal microscopy was performed. Micrographs for cells isolated from patients 6 and 7 are presented in Fig. 6.7.

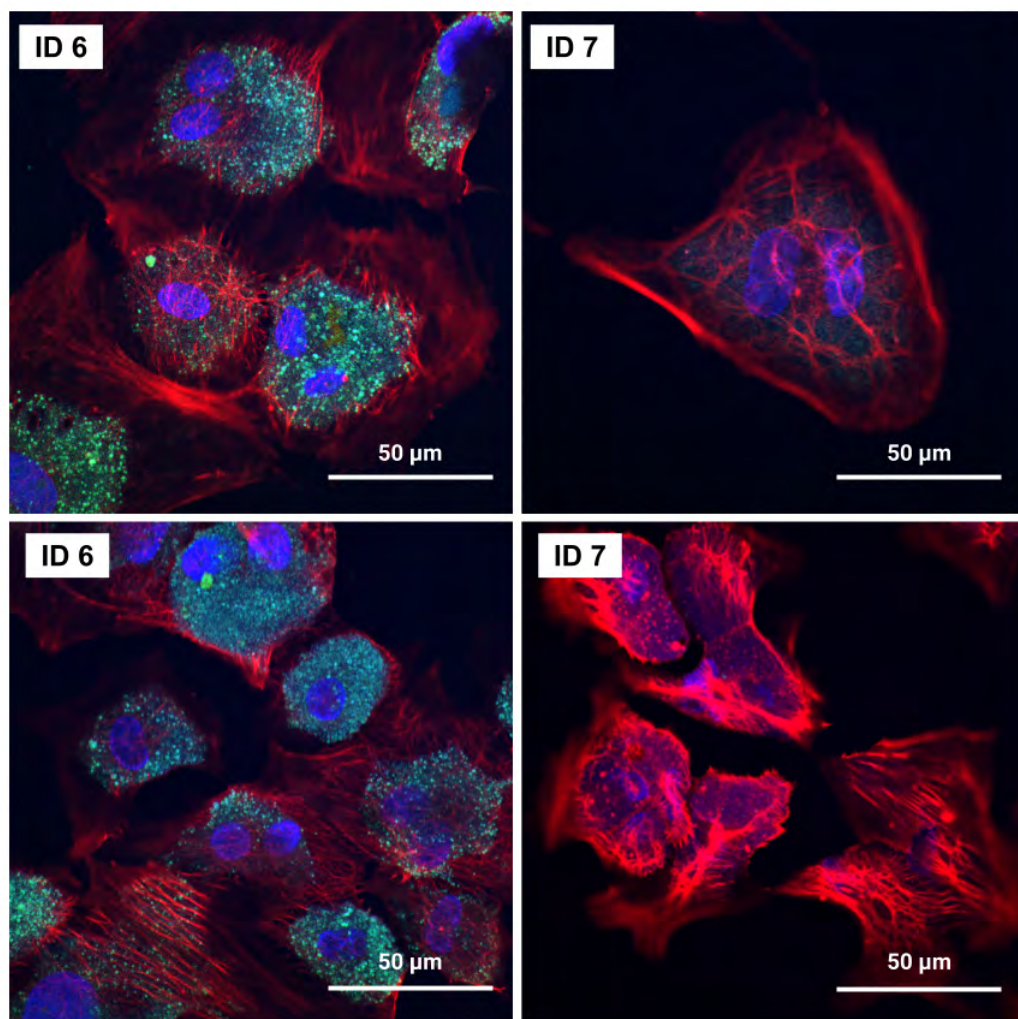


FIGURE 6.7: Confocal microscopy image with stained: actin (red), nucleus (blue) and VE-cadherin (green). Patients ID annotations are described in Tab. 6.1.

In both cases, the presence of multiple nuclei and morphology different from fibroblast confirm, that isolated cells are myxoma. Significant differences are observed in VE-cadherin expression. VE-cadherin is the major transmembrane protein

and plays a crucial role in proper vascular development and permeability. Absence of blood vessels in the tumour from the patient 7 (see Fig. 6.1), may be the reason for reduced VE-cadherin expression in cells isolated from this patient.

Isolated myxoma cells were studied employing PALS. Measurements were performed at 37°C for 1 hour, and each sample had around 20 mln of cells. Exemplary positron lifetime spectrum for one of the samples with fitted model and components related to the annihilation type are presented in Fig. 6.8. Viability of cells was checked before and after measurement, resulting in 10.0(2.3)% difference. Therefore the condition of measurement did not influence cell viability significantly.

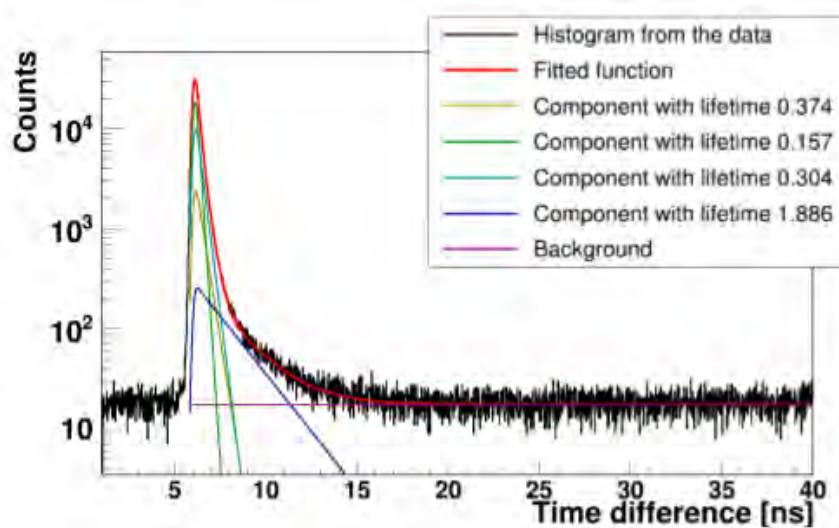


FIGURE 6.8: Exemplary PAL spectrum (obtained for the patient no. 6) for cardiac myxoma cell culture. Superimposed lines indicate distributions of particular components resulting from the fit of Eq. 4.5. Green - para-Positronium, yellow - annihilation in the source material, turquoise - free positron annihilation, blue - ortho-Positronium, purple - background. The spectra do not start at zero because of the time offset between the detectors.

Results for all observed components with a statistical uncertainty of the fit for myxoma cell culture are presented in Tab. 6.5. The obtained mean lifetime of ortho-positronium is slightly lower than for tissue (see Tab. 6.4), yet in both cases, this difference is equal to 0.06 ns, and correspond to the value of about 2σ only.

Determined values of mean ortho-positronium lifetime and intensity, for cardiac myxoma tissue and cell culture, isolated from the same patient, are presented in Fig. 6.9.

TABLE 6.5: Mean positronium lifetime and intensity values for cultured myxoma cells. Patients ID annotations are described in Tab. 6.1.

Patient ID	τ_1 [ns]	I_1 [%]	τ_2 [ns]	I_2 [%]	τ_3 [ns]	I_3 [%]
6	0.157(2)	55.2(1)	0.304(2)	40.7(1)	1.89(3)	4.1(1)
7	0.128(2)	37.4(1)	0.266(2)	58.8(1)	1.83(3)	3.8(1)

The significant difference in ortho-positronium intensity is due to the smaller volume of cells sample, in relation to the tissue size. Highest achievable number of cells were isolated from the sectioned specimen, given its size. Since myxoma cells grow very slowly, it was not possible to obtain more cells from these cultures. Therefore, an increase in the intensity of para-Positronium, which has a similar lifetime to aluminium - chamber material, is observed (Tab. 6.5). Due to detector resolution ($\sigma = 117$ ps), it is not possible, to distinguish aluminium from the para-Positronium component.

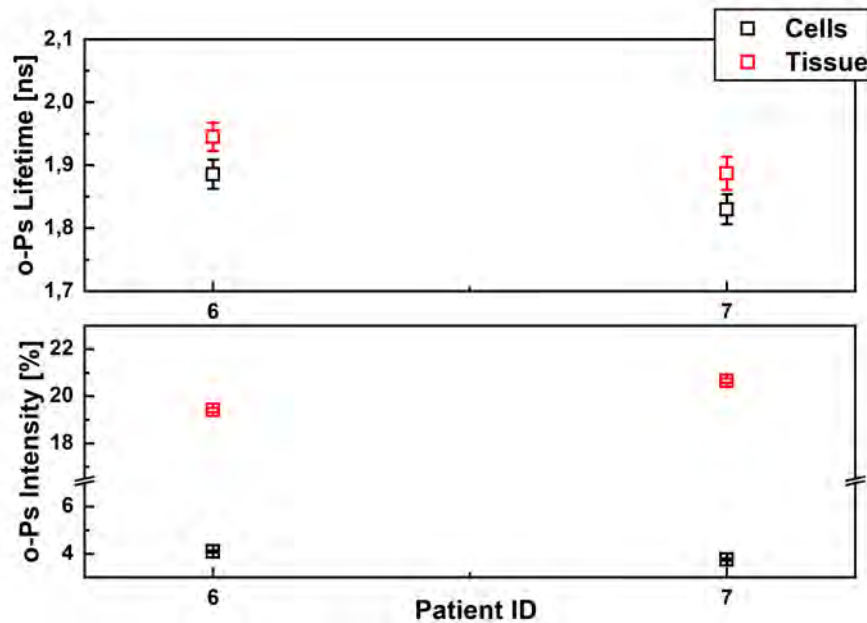


FIGURE 6.9: Ortho-positronium lifetime (upper) and intensity (lower panel) for cardiac myxoma tissue and cell culture isolated from the same patient. Patients ID annotations are described in Tab. 6.1.

Chapter 7

Melanocytes and melanoma cell culture

7.1 Freeze-dried cells

As an example of malignant neoplasm, two melanoma cell lines were chosen with melanocytes as a control. Firstly, experiments with cell lines freeze-dried in various media were performed, to rule out the influence of water, which gives a strong signal in this technique and could affect the results.

7.1.1 PALS

Freeze-dried cell lines of melanoma (WM266-4, WM115) and melanocytes (HEMa-LP) were measured using Positron Annihilation Lifetime Spectroscopy. Exemplary positron lifetime spectrum for freeze-dried in medium 1 melanocytes HEMa-LP (upper), melanoma WM115 (middle) and WM266-4 (lower panel) cell culture, with fitted model and components related to annihilation type are presented in Fig. 7.1.

Results for all observed components with a statistical uncertainty of the fit are presented in Tab. 7.1. Obtained mean lifetime and intensity of ortho-positronium, differs significantly between cell lines; however, they also depend on the used medium.

Differences are observed not only between normal and cancer cells, but also between two lines of melanoma, which allows to assume that positronium can be applied as a biomarker, and also provide information about the degree of malignancy of cancer.

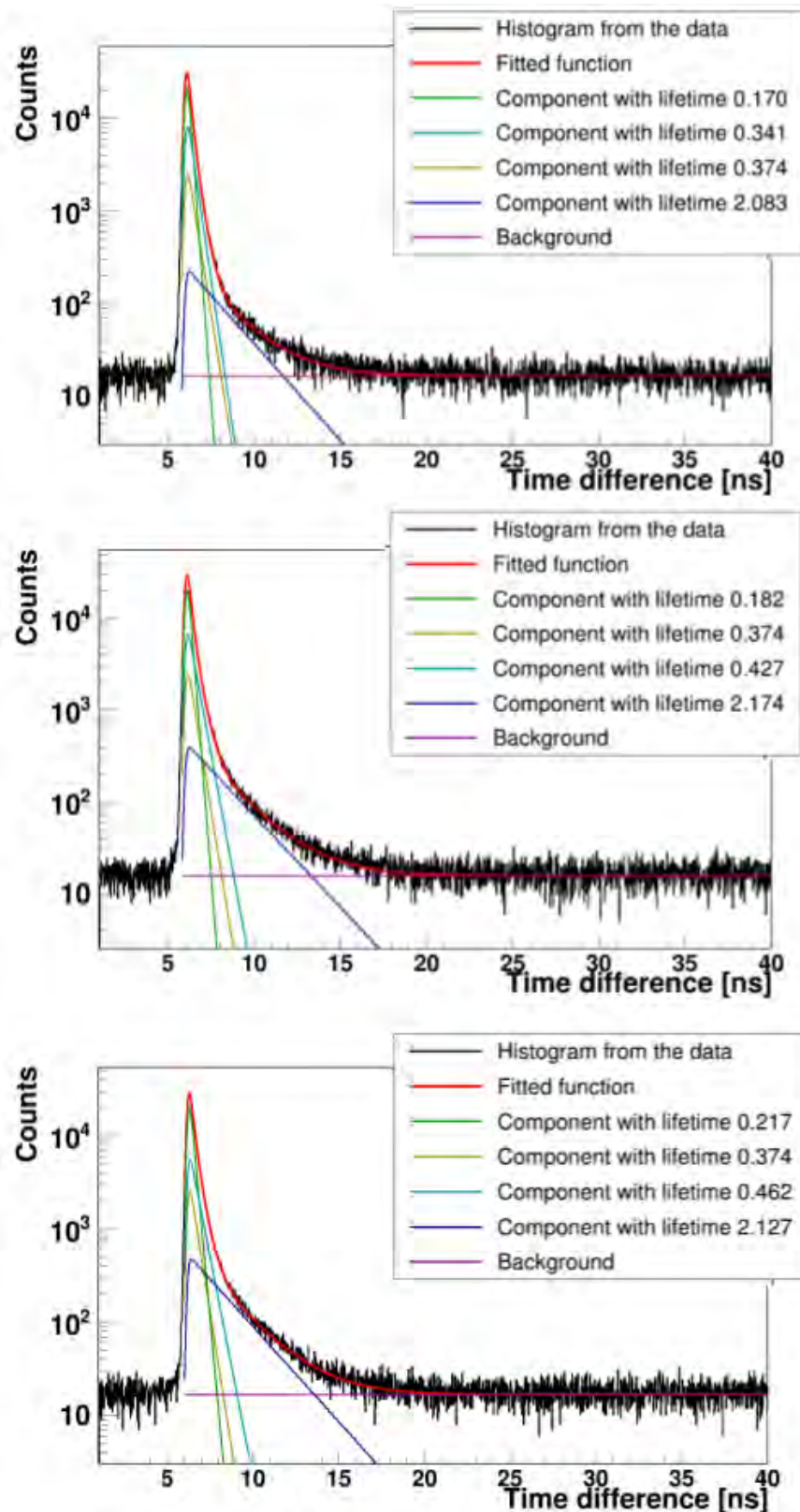


FIGURE 7.1: Exemplary PAL spectra for freeze-dried in medium 1 melanocytes HEMa-LP (upper), melanoma WM115 (middle) and WM266-4(bottom) cell culture. Superimposed lines indicate distributions of particular components resulting from the fit of Eq. 4.5. Green - para-Positronium, yellow - annihilation in source material, turquoise - free positron annihilation, blue - ortho-Positronium, purple - background. The spectra do not start at zero because of the time offset between the detectors.

TABLE 7.1: Mean positronium lifetime and intensity values for freeze-dried in different media melanocytes (HEMa-LP) and melanoma (WM115, WM266-4) cell culture. Medium: **1** - RPMI/M254+20%FBS+10%DMSO, **2** - 10% DMSO in PBS w/o Ca^{2+} , Mg^{2+} , **3** - PBS w/o Ca^{2+} , Mg^{2+} , **4** - 1.5 M PROH + 0.5 M D-trehalose in PBS w/o Ca^{2+} , Mg^{2+} , **5** - 0.25 M D-trehalose in PBS w/o Ca^{2+} , Mg^{2+} .

Cell line	Medium	$\tau_1[ns]$	$I_1[\%]$	$\tau_2[ns]$	$I_2[\%]$	$\tau_3[ns]$	$I_3[\%]$
HEMa-LP	1	0.170(1)	61.6(1)	0.341(1)	34.6(1)	2.08(3)	3.8(2)
	2	0.178(1)	74.0(1)	0.333(1)	24.2(1)	2.36(4)	1.8(3)
	3	0.165(1)	63.2(1)	0.302(1)	34.7(1)	2.31(3)	2.0(3)
	4	0.169(1)	65.3(1)	0.338(1)	30.4(1)	1.75(3)	4.3(2)
	5	0.171(1)	68.7(1)	0.344(1)	28.1(1)	1.81(4)	3.2(2)
WM115	1	0.182(1)	60.6(1)	0.427(1)	32.6(1)	2.17(1)	6.9(1)
	2	0.179(1)	54.2(1)	0.400(1)	37.8(1)	1.99(1)	8.1(1)
	3	0.179(1)	62.5(1)	0.421(1)	31.0(1)	1.98(1)	6.5(1)
	4	0.183(1)	59.1(1)	0.439(1)	30.9(1)	2.11(1)	10.0(1)
	5	0.173(1)	55.5(1)	0.410(1)	36.2(1)	1.85(1)	8.3(1)
WM2664	1	0.217(1)	63.9(1)	0.462(1)	27.9(1)	2.13(1)	8.2(1)
	2	0.222(1)	64.0(1)	0.475(1)	27.8(1)	2.29(1)	8.2(1)
	3	0.223(1)	76.9(1)	0.563(1)	16.5(1)	2.07(1)	6.6(1)
	4	0.229(1)	68.8(1)	0.585(1)	22.6(1)	1.99(1)	8.6(1)
	5	0.223(1)	66.4(1)	0.528(1)	24.3(1)	1.98(1)	9.2(1)

Determined values of mean ortho-positronium lifetime and intensity are shown in Fig. 7.2. Cells were freeze-dried in different media to investigate the influence of hydration level on PALS parameters. The observed differences for one cell line, preserved in given media can be related to a number of viable cells after the procedure, as well as a ratio of liquid to a solid fraction in the sample. Medium 1 containing FBS and DMSO, commonly used as a cryoprotectant, which prevents the formation of ice crystals and therefore cell damage, can increase the mean lifetime of positronium [116,117]. In medium 2, also DMSO was used, but without FBS, which increase cell recovery [118].

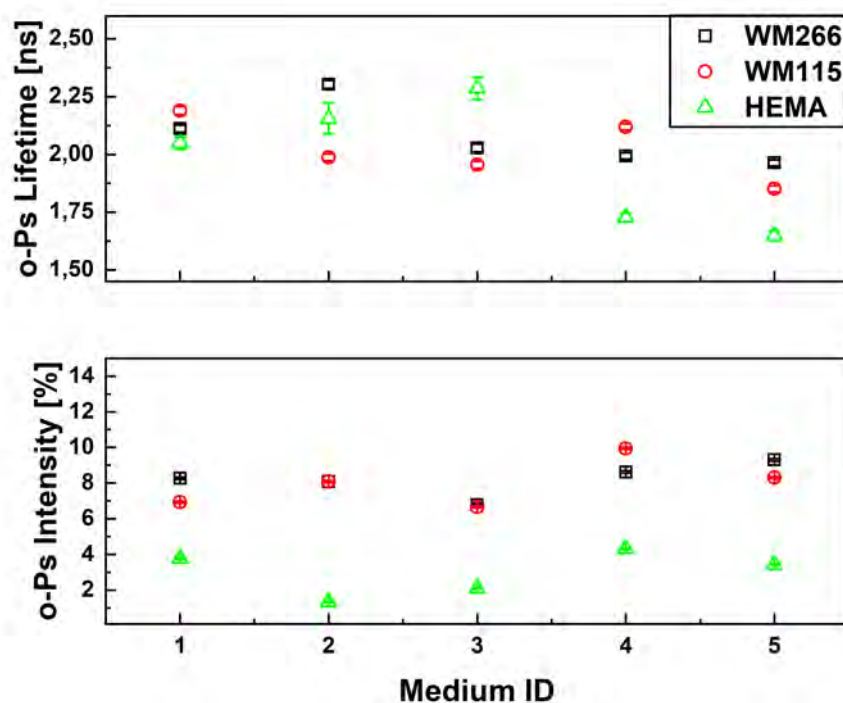


FIGURE 7.2: Mean ortho-positronium lifetime (upper) and intensity (lower panel) for freeze-dried in different mediums melanocytes (HEMa-LP) and melanoma (WM115, WM266-4) cell culture.

Medium 3 was PBS w/o Ca^{2+} , Mg^{2+} , which serves as a control since it does not contain any protecting reagents and does not bind water molecules, allowing for possibly the best dehydration of the sample, but also will implicate the least survival of cells. Medium 4 consist of propylene glycol, which is also a good cryoprotectant, and is not toxic as DMSO. D-Trehalose was also added as an additional protectant, which binds water molecules, increasing cell survival during freezing [118]. The last

medium - 5 - contained only D-Trehalose to check the water-binding abilities without any cryoprotectants. As it would allow studying, both amorphous and crystalline states, to show the correlation between the intermolecular voids and activated water diffusion [119].

7.1.2 Rehydration

In order to assess the impact of the freeze-drying medium on cell survival, rehydration of cells in culture medium was performed, and cell viability was assessed. Cells were also weighted before and after freeze-drying, to determine the percentage value of water loss. Results of viability and water mass loss are presented in Tab. 7.2.

Percentage water mass loss describe dehydration of sample during freeze-drying, the higher the value, the greater is water loss, and therefore sample dehydration. From the chosen media, these containing D-Trehalose results in the lowest mass loss, which is due to the ability of this compound to bind water molecules. In case of melanocytes and WM115 melanoma cell line, this difference is higher than in WM266-4 melanoma cell line. The highest water loss is observed in cells freeze-dried in medium 3 (only PBS w/o Ca^{2+} , Mg^{2+}), as it was expected since this buffer does not have water-binding properties. In Fig. 7.3 photograph of freeze-dried cells is presented, where the various level of hydration can be observed by eye, particularly in case of melanocytes and WM115 melanoma.

The highest viability post rehydration of cells can be observed in case of media 1 and 4 containing cryoprotectants. Cells freeze-dried in the third medium, demonstrating the highest dehydration level, also have the lowest viability after rehydration. Cells freeze-dried in medium 5, despite containing D-Trehalose, have very low viability after the procedure.

TABLE 7.2: Cell mass loss and viability before and after hydration for freeze-dried in different mediums melanocytes (HEMa-LP) and melanoma (WM115, WM266-4) cell culture.

Medium: **1** - RPMI/M254+20%FBS+10%DMSO,**2** - 10% DMSO in PBS w/o Ca^{2+} , Mg^{2+} ,**3** - PBS w/o Ca^{2+} , Mg^{2+} ,**4** - 1.5 M PROH + 0.5 M D-trehalose in PBS w/o Ca^{2+} , Mg^{2+} ,**5** - 0.25 M D-trehalose in PBS w/o Ca^{2+} , Mg^{2+} .

Cell line	Medium	Δm [mg]	waterloss[%]	Viability _{before} [%]	Viability _{after} [%]
HEMa-LP	1	117.8(1)	91.8(1)	82.2(2.0)	40.1(2.0)
	2	115.4(1)	92.4(1)	83.9(2.0)	45.2(2.0)
	3	109.0(1)	94.8(1)	74.4(2.0)	12.2(2.0)
	4	92.4(1)	68.3(1)	70.4(2.0)	48.4(2.0)
	5	111.8(1)	80.1(1)	73.7(2.0)	17.8(2.0)
WM115	1	426.1(1)	83.7(1)	86.0(2.0)	50.9(2.0)
	2	493.4(1)	86.1(1)	86.7(2.0)	41.3(2.0)
	3	516.3(1)	94.2(1)	87.5(2.0)	16.4(2.0)
	4	240.1(1)	52.7(1)	82.3(2.0)	44.8(2.0)
	5	286.2(1)	63.0(1)	79.5(2.0)	32.8(2.0)
WM266-4	1	378.2(1)	86.8(1)	92.0(2.0)	28.8(2.0)
	2	394.3(1)	86.5(1)	90.9(2.0)	13.6(2.0)
	3	442.9(1)	87.2(1)	89.4(2.0)	8.4(2.0)
	4	285.5(1)	72.7(1)	97.3(2.0)	51.1(2.0)
	5	316.4(1)	80.6(1)	97.2(2.0)	8.5(2.0)

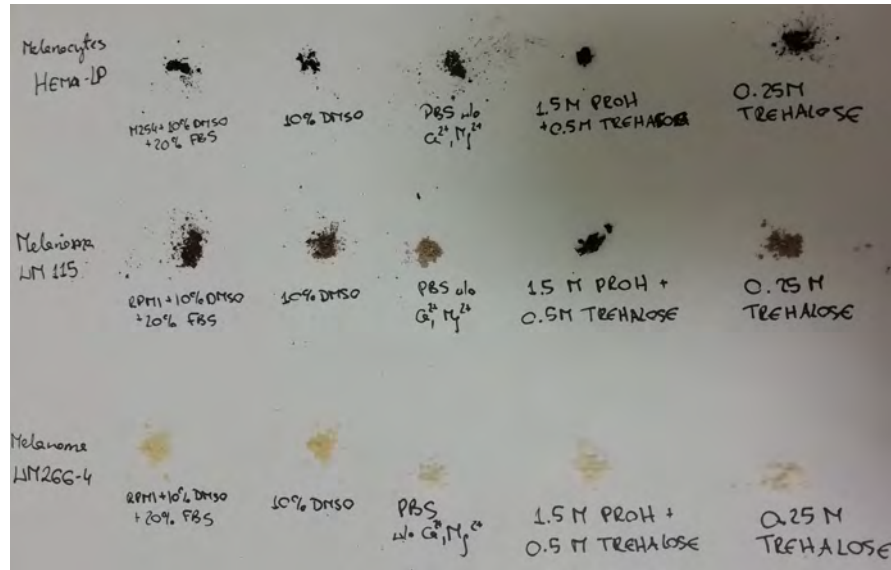


FIGURE 7.3: Photograph of freeze-dried in different media melanocytes (HEMa-LP) and melanoma (WM115, WM266-4) cell culture.

7.1.3 NMR - cells hydration

^1H – NMR spectroscopy was performed to determine the ratio of mobile protons (i.e. water molecules) to solid (immobilized) protons, and estimate hydration of freeze-dried cell lines. The frequency spectrum is described by a sum of Gaussian and of Lorentzian functions, which describe solid and aqueous fraction, respectively. In Fig. 7.4 resulting spectra for all investigated cell lines and all mediums used are presented. Besides the lower-left panel of Fig. 7.4 shows the exemplary spectrum with a superimposed result of the fit of Eq. 7.1:

$$G(\nu) = y_0 + \frac{S_G}{\sqrt{\pi \ln 2} \Delta \nu_G} \exp \left[-2 \left(\frac{\nu - \nu_G}{\sqrt{2 \ln 2} \Delta \nu_G} \right)^2 \right] + \frac{2S_L}{\pi} \left[\frac{\Delta \nu_L}{4(\nu - \nu_L)^2 + \Delta \nu_L^2} \right], \quad (7.1)$$

where: S_G, S_L - area under Gaussian and Lorentzian line, $\Delta \nu_G, \Delta \nu_L$ - full width at half maximum, ν_G, ν_L - mean value of distribution.

Hydration of sample can be estimated as a ratio of area under Lorentzian distribution, which corresponds to liquids protons closely and loosely bound, and area under Gaussian distribution, which corresponds to the solid fraction of samples. In case of all samples, one Gaussian and one Lorentzian component were fitted, describing the ratio of aqueous to solid fractions.

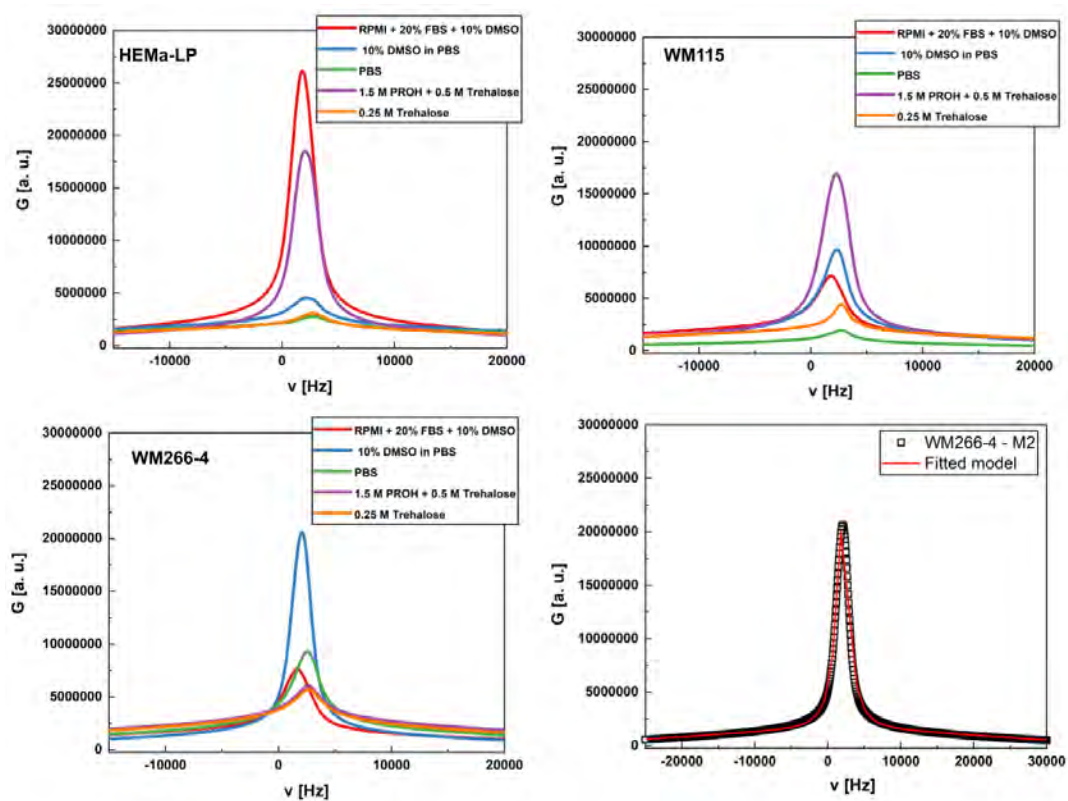


FIGURE 7.4: ^1H – NMR spectra for freeze-dried in different mediums (upper left) melanocytes (HEMa-LP) and melanomas: (upper right) WM115 and (lower left) WM266-4 cell culture. (lower right) Exemplary spectrum (WM266-4 cell line in the second medium) with the superimposed result of the fit of the model described by Eq. 7.1.

Ratios of mobile protons to solid (immobilized), which corresponds to hydration of freeze-dried in different mediums cell lines, are presented in Tab. 7.3. The higher the value, the higher the contribution of mobile protons (water molecules), and therefore higher the hydration of the sample. Full width at half maximum (FWHM) of the Lorentzian contribution to the spectrum corresponds to the level of loosely-to-tightly bound water, the higher the value, the more tightly water molecules are bound [120].

In case of all three cell lines, the highest level of hydration is observed in cells freeze-dried in the fourth medium, containing propylene glycol and D-Trehalose, with hydration ratio equal to 1.01(02), 0.90(02) and 0.98(02) for melanocytes, WM115 and WM266-4 melanoma cell lines, respectively.

TABLE 7.3: Ratio of mobile protons to solid (immobilized) of freeze-dried in different mediums melanocytes (HEMa-LP) and melanoma (WM115, WM266-4) cell culture.

Medium: **1** - RPMI/M254+20%FBS+10%DMSO,**2** - 10% DMSO in PBS w/o Ca^{2+} , Mg^{2+} ,**3** - PBS w/o Ca^{2+} , Mg^{2+} ,**4** - 1.5 M PROH + 0.5 M D-trehalose in PBS w/o Ca^{2+} , Mg^{2+} ,**5** - 0.25 M D-trehalose in PBS w/o Ca^{2+} , Mg^{2+} .

Cell line	Medium	$\Delta\nu_L$ [kHz]	$\Delta\nu_G$ [kHz]	S_L/S_G
HEMa-LP	1	2.40(02)	54.04(14)	0.83(02)
	2	7.19(06)	79.51(91)	0.24(02)
	3	4.60(14)	111.69(18)	0.09(02)
	4	2.57(02)	47.02(14)	1.01(02)
	5	4.28(09)	113.07(17)	0.14(02)
WM115	1	3.75(02)	59.63(20)	0.28(02)
	2	3.26(01)	49.10(13)	0.45(02)
	3	5.14(06)	64.28(19)	0.22(02)
	4	2.88(01)	48.21(13)	0.90(02)
	5	3.90(02)	63.84(16)	0.14(02)
WM2664	1	3.41(01)	60.88(16)	0.33(02)
	2	2.03(01)	47.73(17)	0.89(02)
	3	3.56(01)	54.15(13)	0.36(02)
	4	2.93(01)	46.90(09)	0.98(02)
	5	5.51(03)	55.99(11)	0.21(02)

Medium containing DMSO also had higher hydration level, while the lowest was observed in case of third medium containing PBS, which is consistent with determined water mass loss, during a freeze-drying procedure (see Tab. 7.2). Interestingly, cells in medium containing only D-Trehalose, are characterized by a very low hydration level, despite water-binding properties of this compound, and equal to 0.14(02), 0.14(02) and 0.21(02) for melanocytes, WM115 and WM266-4 melanoma cell lines, respectively. This can be the reason for low viability after hydration, for cells preserved in this medium.

Similarities can also be observed in FWHM values of the Lorentzian line, which are higher in case of less hydrated samples. In all cases, this value is higher than 2 kHz, which corresponds to tightly bound water. The same relationships can be observed for FWHM values of the Gaussian line.

7.2 Living cells measurements

7.2.1 Cell culture and viability

Positron Annihilation Lifetime Spectroscopy technique requires a significantly high number of cells, what was a challenge especially in case of melanocytes, which as normal cells are characterized by the limited number of divisions and do not proliferate indefinitely. In Fig. 7.5 micrographs of HEMa-LP, WM115 and WM266-4 cell lines cultures are presented for low, and high confluence - upon harvest for the experiment. Differences in cell morphology are observed according to cell type. Melanocytes are arranged in adherent monolayer, with observed contact inhibition in both locomotion, and proliferation. In case of both melanoma cell lines, WM115 and WM266-4, cells also growth adherently, while detachment from the surface can be observed during cell division additionally, as most cancer cells grow in multi-layer.

As it was mentioned before, a high number of cells was required for PALS experiment, as well as conditions during measurement had to be adjusted not to influence cell viability, which was checked before and after each test.

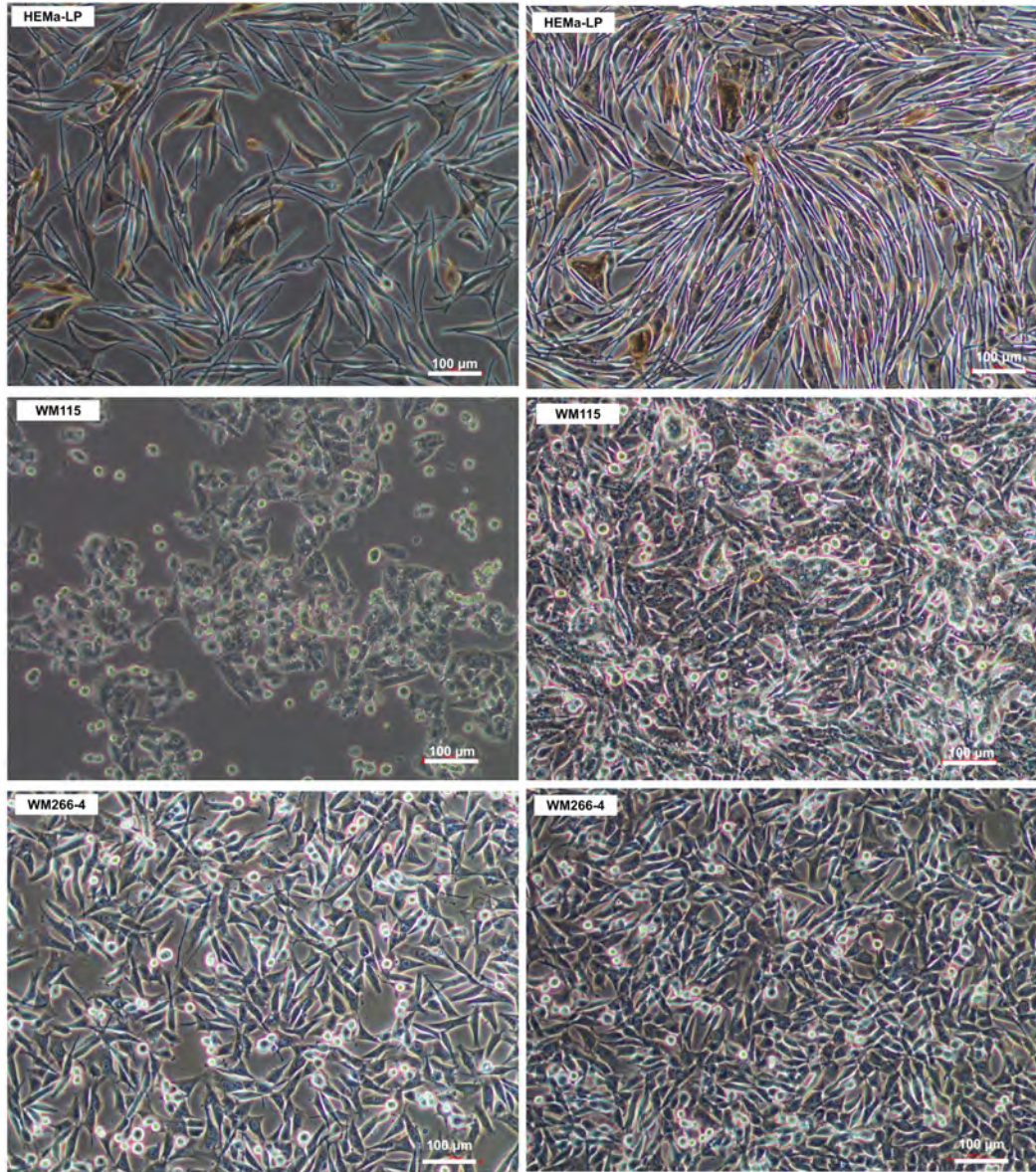


FIGURE 7.5: Micrograph showing culture of HEMa-LP, WM115 and WM266-4 cell lines in (left) low and (right) high - upon harvest - confluence. Scale bar has $100\mu m$.

Cells population doubling time was calculated using Eq. 7.2:

$$T_d = \frac{t * \ln(2)}{\ln(N_t) - \ln(N_0)} \quad (7.2)$$

where: t - time of culture, N_0 - initial number of viable cells, N_t - number of viable cells after time t .

Doubling time is equal to around 93 h for melanocytes, 63 h and 34 h for WM115 and WM266-4 melanoma cell lines, respectively. Proper conditions of the measurement, were assessed based on the difference in the viability of cells, before and after

measurement. Viability change is calculated as Eq. 7.3:

$$V_{ch} = 100\% * \frac{V_{before} - V_{after}}{V_{after}}, \quad (7.3)$$

where: V_{before} - viability of cells before measurement, V_{after} - viability of cells after measurement.

Results from these experiments are presented in Tab. 7.4, as a mean value with standard deviation, from three consecutive measurements. These results were taken into account in designing an optimal protocol for PALS experiment with living cells. Low viability change in case of all three cell lines, proves suitable conditions for measurements of biological samples, were created.

TABLE 7.4: Population doubling time, the number of cells and viability change of melanocytes (HEMa-LP) and melanoma (WM115, WM266-4) cell culture for PALS experiment.

Cell line	$T_d[h]$	No. of cells/measurement	$V_{ch}[\%]$
HEMa-LP	93(5)	3.54(88)E7	2.1(1.5)
WM115	63(4)	1.17(09)E8	5.2(1.2)
WM266-4	34(2)	1.32(14)E8	2.0(9)

7.2.2 PALS experiment

The protocol of the experiment was not only validated, taking into account the viability of cells but also repeatability was examined. Reproducibility was tested with the WM266-4 cell line since it has the shortest doubling time among the investigated cell lines, and thus allowed for the most effective, multiple repetitions of experiments.

In order to evaluate a protocol for PALS, seven consecutive measurements with WM266-4 melanoma cell line were performed. For six, measurement took 1 h, while in case of last one, an additional measurement for another hour was done, to check

the stability of the result in a longer time. Results for all observed components with a statistical uncertainty of the fit are presented in Tab. 7.5.

TABLE 7.5: Mean positronium lifetime and intensity values for consecutive measurement of alive melanoma WM266-4 cell culture.

No.	τ_1 [ns]	I_1 [%]	τ_2 [ns]	I_2 [%]	τ_3 [ns]	I_3 [%]
1	0.206(01)	36.6(1)	0.452(01)	47.2(1)	1.98(01)	16.7(1)
2	0.231(01)	38.2(1)	0.476(01)	43.5(1)	1.98(02)	18.3(1)
3	0.23(01)	40.2(1)	0.489(01)	42.6(1)	2.03(01)	17.2(1)
4	0.243(01)	43.5(1)	0.501(01)	39.1(1)	2.00(02)	17.3(1)
5	0.243(01)	46(1)	0.518(01)	37.2(1)	2.00(01)	16.8(1)
6	0.222(01)	39.8(1)	0.465(01)	43.3(1)	1.96(03)	16.8(1)
7	0.229(01)	36.6(1)	0.48(01)	45.5(1)	2.00(01)	17.9(1)
7_2h	0.243(01)	41.6(1)	0.502(01)	40.8(1)	2.01(01)	17.6(1)
Average(STD)	0.229(13)	40.1(3.5)	0.483(22)	42.6(3.5)	1.99(2)	17.2(7)

Obtained values of positronium lifetime and intensity are in agreement within statistical uncertainties. Also, for longer measurement, no significant differences were observed. Determined values of mean ortho-positronium lifetime and intensity for all repetitions are presented in Fig. 7.6. Stability of obtained results proved, that developed protocol for study is optimal. Even longer time of measurements does not result in any significant changes in mean lifetime and intensity. Hence, validated PALS protocol can be applied to study living cells.

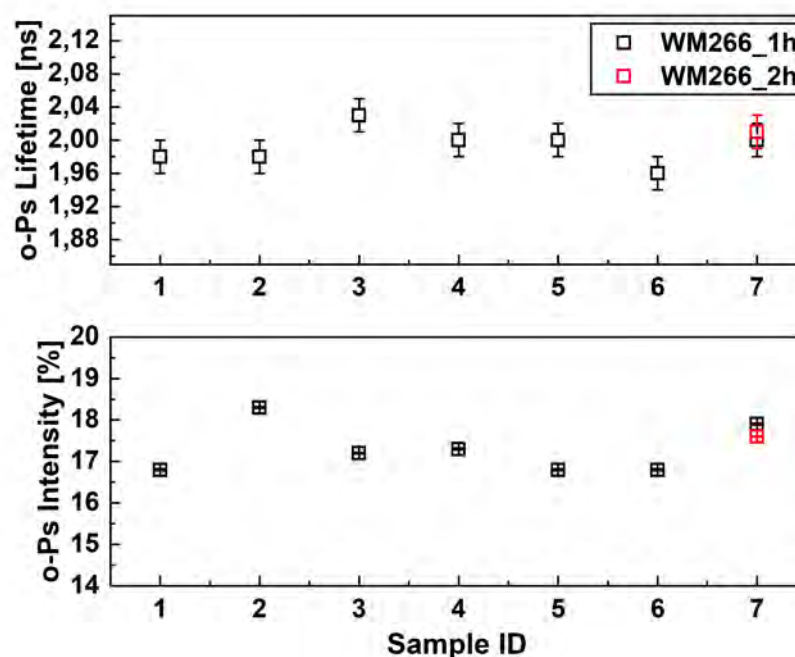


FIGURE 7.6: Mean ortho-positronium lifetime (upper) and intensity (lower panel) for alive melanoma WM266-4 cell culture from 7 consecutive measurements.

Comparison between normal and cancer cell lines was evaluated by PALS, to determine differences in proposed biomarker value. Exemplary positron lifetime spectrum for living melanocytes HEMa-LP (upper), melanoma WM115 (middle) and WM266-4 (lower panel) cell culture with a fitted model, and components related to annihilation type are presented in Fig. 7.7.

Results for all observed components are presented in Tab. 7.6. Each point is calculated as a mean value with a standard deviation of 3 consecutive measurements. Obtained results are significantly different between all these cell lines.

Determined values of mean ortho-positronium lifetime and intensity for living HEMa-LP melanocytes, WM115 and WM266-4 melanoma, are presented in Fig. 7.8 and are equal to 1.84(3) ns, 1.93(2) ns, 1.99(2) ns in lifetime and 12.7(1.8)%, 18.5(0.6)%, 17.0(0.8)% in intensity, respectively.

Differences are observed, not only between cancer and normal cells but also between two melanoma cell lines, with different degree of malignancy. This conclusion is the same, as it was drawn for freeze-dried cells, where also differences between these cell lines were observed in all studied cases.

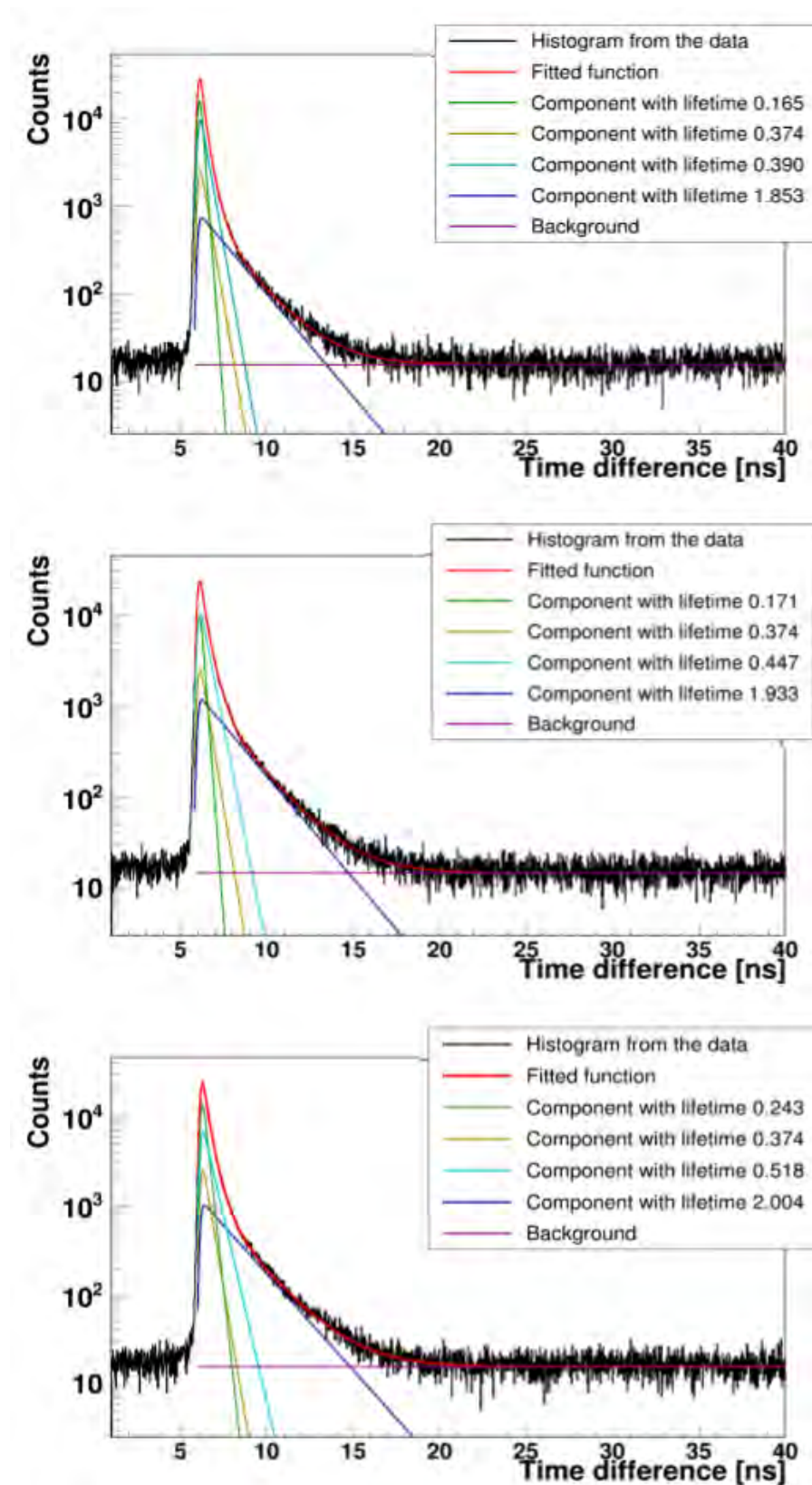


FIGURE 7.7: Exemplary PAL spectra for living melanocytes HEMa-LP (upper), melanoma WM115 (middle) and WM266-4(bottom) cell culture. Superimposed lines indicate distributions of particular components resulting from the fit of Eq. 4.5. Green - para-Positronium, yellow - annihilation in the source material, turquoise - free positron annihilation, blue - ortho-Positronium, purple - background. The spectra do not start at zero because of the time offset between the detectors.

TABLE 7.6: Mean positronium lifetime and intensity values for alive melanocytes (HEMa-LP) and melanoma (WM115, WM266-4) cell culture. Each value is calculated as an average and uncertainty as a standard deviation from 3 consecutive measurements.

Cell line	τ_1 [ns]	I_1 [%]	τ_2 [ns]	I_2 [%]	τ_3 [ns]	I_3 [%]
HEMa-LP	0.166(03)	41.7(4.2)	0.394(9)	45.5(2.4)	1.84(3)	12.7(1.8)
WM115	0.160(15)	27.2(3.6)	0.438(12)	54.3(3.1)	1.93(2)	18.5(0.6)
WM2664	0.228(12)	40.6(3.5)	0.482(21)	42.4(3.3)	1.99(2)	17.0(0.8)

These results prove that even with the presence of water, differentiating among living normal and cancer cells, is possible employing Positron Annihilation Spectroscopy. This indicates that positronium may serve as a novel biomarker, while factors responsible for observed differences need to be investigated.

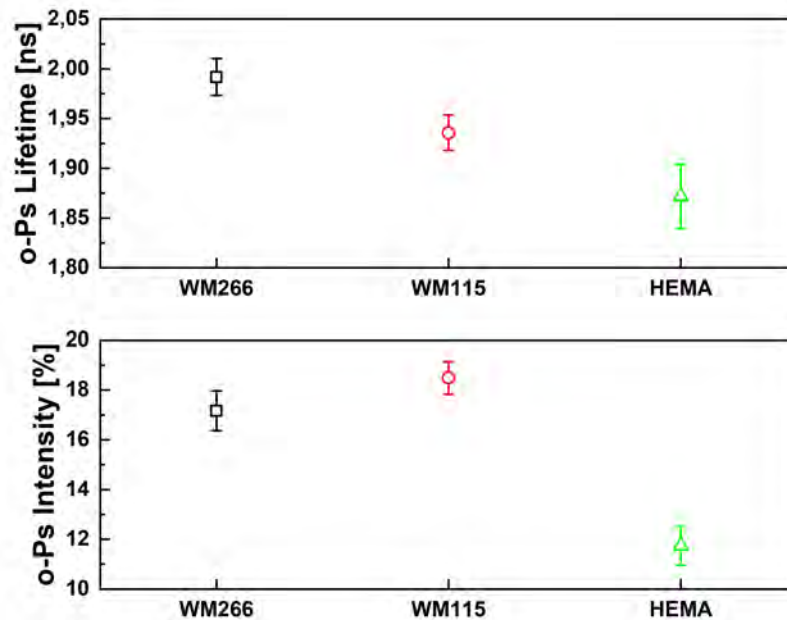


FIGURE 7.8: Mean ortho-positronium lifetime (upper) and intensity (bottom) for alive melanocytes (HEMa-LP) and melanoma (WM115, WM266-4) cell culture. Each point is calculated as an average and uncertainty as a standard deviation from 3 consecutive measurements.

7.2.3 EPR - melanin concentration

Melanocytes and melanoma cell lines are pigmented cells. Different pigmentation due to melanin concentration can be observed by eye, as presented in Fig. 7.9. Pigmentation is observed in melanocytes and WM115 melanoma cell pellet, while WM266-4 seems to be unpigmented.

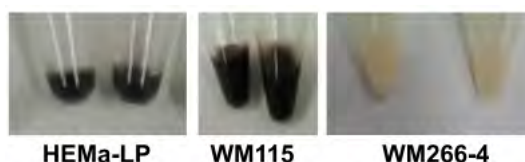


FIGURE 7.9: Photographs of melanocytes (HEMa-LP) and melanoma (WM115, WM266-4) cell pellet.

The concentration of melanin was determined using Electron Paramagnetic Resonance, in relation to standardized synthesized L-DOPA melanin. Measurement was performed for samples containing 7 and 14 mln cells. EPR spectra are presented in Fig. 7.10.

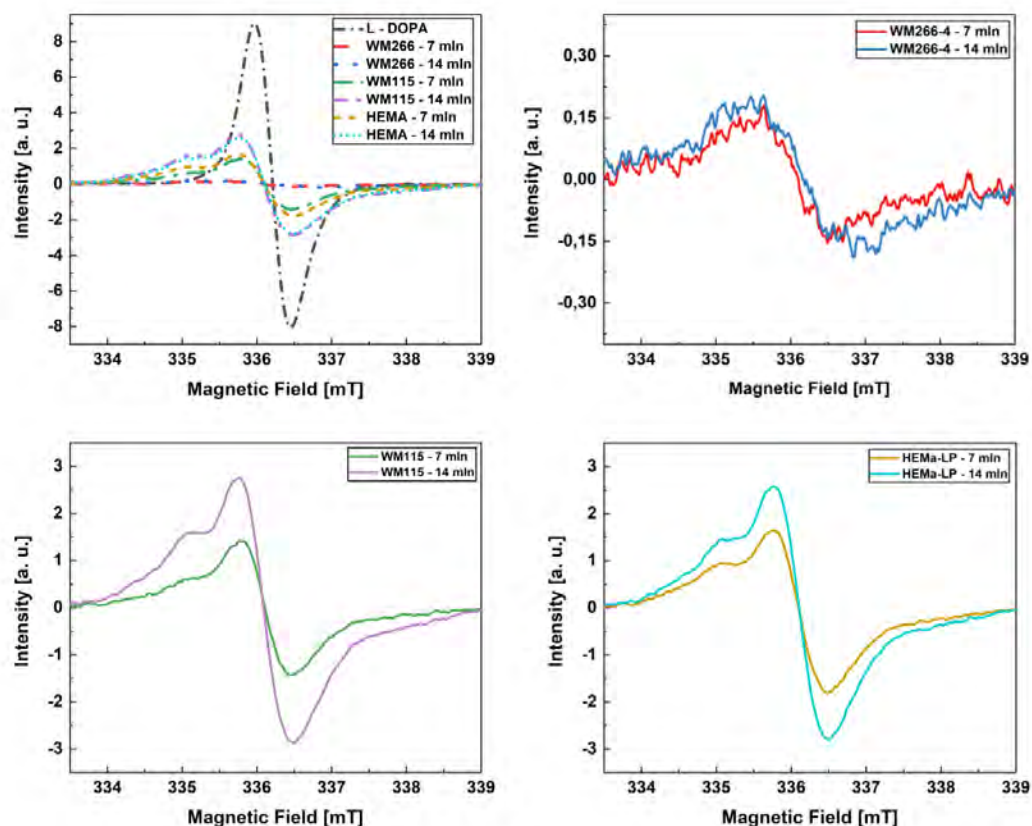


FIGURE 7.10: EPR spectra for alive melanocytes (HEMa-LP) and melanoma (WM115, WM266-4) cell culture.

In the upper left panel of Fig. 7.10 signals from all samples with synthetic melanin are presented. Other panels show a comparison, between results obtained for samples of the same cell line, but with different cells number. The intensity of melanin in a WM266-4 cell line is slight, in comparison to a standard L-DOPA. While for melanocytes and WM115 melanoma, melanin concentration is around six times higher than in WM266-4. Difference between these pigmented cell lines are small, yet higher melanin intensity can be observed in melanocytes. In both pigmented cell lines, components from both eumelanin and pheomelanin can be observed.

Determined melanin concentration per single cell is presented in Tab. 7.7. Obtained results confirm the difference in pigmentation due to total melanin concentration, and equals to 13.70(79) pg, 12.17(81) pg, 2.08(22) pg per single cell for HEMa-LP melanocytes, WM115 and WM266-4 melanoma, respectively.

TABLE 7.7: Melanin concentration per cell for alive melanocytes (HEMa-LP) and melanoma (WM115, WM266-4) cell culture. Each value is calculated as an average and uncertainty as a standard deviation from measurements for 7 and 14 mln of cells.

Cell line	Melanin concentration [pg/cell]
HEMa-LP	13.70(79)
WM115	12.17(81)
WM2664	2.08(22)

Melanin is a natural, free radicals scavenger [121, 122] in human cells, and can be accounted for observed differences in positronium lifetime, between studied cell lines. However, this hypothesis requires further investigation.

Part IV

Discussion

Chapter 8

Discussion

The results of research conducted on positronium being a prospect for the new biomarker for cancer diagnosis are presented in this thesis. Studies were performed on two models: sectioned tissues and cultured cell lines, representing benign and malignant tumours, respectively. In both cases, normal tissue and cell line were examined as a control.

8.1 Cardiac myxoma

Cardiac myxoma was studied as an example of benign tumour. In the light of discussed research, the group of 10 cases (4 male and 6 female, over 50 years old) was examined. Studied specimens have been confirmed as myxoma tumours by a histopathological examination done postoperatively. All patients had a single tumour (9 localized in the left atrium and 1 in the right), which manifested itself as a solid type in 70% of cases, and in 30% as a papillary. These facts are in agreement with the previously observed atrial myxoma profile [123].

The first part of the study was focused on myxoma tumours, cases 1-4, fixed in formalin (Tabs. 6.1, 6.2) to exclude the factor of tissue decomposition on positronium parameters. Additionally, since obtained perioperative tissues had heterogeneous structure observed by eye, each tumour from a given patient has been cut into few pieces of the same thickness (Tab. 5.1), to check for possible correlation between tumour type and structure and positronium parameters. Resulting mean positronium lifetime and its production intensity are presented in Tab. 6.3. Mean o-Ps lifetime is consistent between sections of one specimen as well as between tumours of different patients with an average value of 2.01(02) ns, and with slight differences

between o-Ps intensity. Average of the observed differences is around 20 ps and 1% in mean lifetime and intensity, respectively. It can originate from the heterogeneity of the tumour. However, the impact of this factor can be diminished, due to fixation and influence of formalin on the lifetime, as observed in case of uterus tissues studies [8,9]. Nevertheless, obtained values are consistent from patient to patient, and there are no significant differences based on tumour type or patient sex, age or comorbidities.

The second part of studies of cardiac myxoma was conducted to test the working hypothesis that positronium can be used as a novel biomarker and therefore, values of mean o-Ps lifetime and intensity obtained for cancer and normal tissue tissues were compared. The normal, mediastinal adipose tissue which has been used as a control, was obtained from the same patient as the tumour. Samples for cases 5-10 (Tab. 6.1), were studied without fixation, to exclude formalin impact on the positronium lifetime and within 4 hours after surgery, to avoid the influence of tissue decomposition in time. In case of both, mean o-Ps lifetime and intensity (Tab. 6.4), significant differences between myxoma and adipose tissue with an average difference equal to 0.8 ns and 10.7% respectively are observed. These differences are much higher than in other studies of normal and cancer tissues [4, 8, 124]. Simultaneously, the mean ortho-Positronium lifetime for the same tissue type, in both myxoma and adipose tissue is consistent between different patients, with an average value of 1.92(02) ns and 2.72(05) ns, respectively. Slight differences between o-Ps intensity of the same type of tissue are observed between different patients, with average values equal to 18.4(2.0)% and 29.1(1.5)% for myxoma and adipose tissue, respectively.

Results are in agreement with ones obtained for fixed tissues, where minor differences in positronium parameters are observed in the same tissue type from patient to patient. Nevertheless, the differences between normal and tumour tissues are, in all cases, significant, and differences in positronium lifetime and intensity originating from tissue heterogeneity or diversity in the study group do not influence the results. Therefore, positronium parameters allow differentiating between tumour and normal tissue, which in this case supports the research hypothesis.

Last part of studies of cardiac myxoma was dedicated to investigate the differences between tumour specimen and a derived cell line, to test the impact of extracellular matrix or present blood vessels on the positronium lifetime. In micrograph Fig. 6.6 obtained myxoma cell culture is presented. Cells were growing adherently in clusters and are relatively big, usually with multiple nuclei.

Cell cultures were not contaminated with fibroblasts which were confirmed by VE-cadherin staining (Fig. 6.7). For both cases in most cells, multiple nuclei were observed, generally, each cell had two. The cells were characterized by extensive structures of actin filaments, while significant differences were observed in VE-cadherin expression. VE-cadherin, as a major transmembrane protein, regulates endothelial cell adhesion, and as such directly participate in the formation of blood vessels and the maintenance of their structural integrity, regulates various cellular processes such as cell proliferation, apoptosis and modulates vascular endothelial growth factor receptor functions [125,126]. Reduced VE-cadherin expression in cells isolated from patient 7, may be the reason for the absence of blood vessels in the tumour from that patient (Fig. 6.1).

Isolated myxoma cells were studied by means of PALS. Cells were not-fixed, and measurement was performed at 37°C for 1 hour to ensure proper conditions, which will not influence cell viability significantly. Viability of cells was checked before and after measurement, resulting in 10.0(2.3)% difference. Therefore optimal conditions for the experiment were obtained. The obtained mean o-Ps lifetime of cells (Tab. 6.5) is slightly lower than for tissue (Tab. 6.4), yet in both cases, this difference is constant and equals 0.06 ns which corresponds to the value of about 2σ . This result shows that extracellular matrix and the presence of blood vessels, does not influence the mean lifetime of o-Ps significantly. In conclusion, the myxoma cells themselves contribute mostly to observed differences between tumour and normal tissue.

Although the significant difference in ortho-positronium intensity between cells and tissues were observed, it is due to the smaller volume of a cell sample in relation to tissue size, each sample had around 20 mln of cells, and that resulted in about 10 times smaller sample volume. Based on the specimen size, the highest possible number of cells were isolated. Since myxoma cells grow very slowly, it was not possible

to obtain more cells from these cultures. As a result, a layer of the studied sample was much smaller than 1 mm and most of positrons from the ^{22}Na were passing to the aluminium holder. This is also the reason for the increase in the intensity of para-positronium. Hence, it has a similar mean lifetime to aluminium, chamber material, and due to detector resolution ($\sigma = 117$ ps), it is not possible to distinguish between these two.

Nevertheless, all observed differences between the same type of tissue from patient to patient or cell isolated from tissue are an order of magnitude smaller than, ones observed between normal and tumour tissue. This is evidence, that positronium as a novel specific biomarker to be used in cancer diagnostic.

8.2 Melanoma and melanocytes

8.2.1 Freeze-dried cells - the influence of water on positronium lifetime

Two melanoma cell lines (WM115 and WM266-4) were chosen as an example of malignant neoplasm with melanocytes (HEMa-LP) as a control.

The first stage of the experiment was to investigate what is the influence of water on positronium lifetime, as it is known from the literature that it is a predominant factor, in highly hydrated systems, and can depend significantly on the concentration of present ions [127–129]. In order to examine this relation, cultured cells were freeze-dried in five media, which allowed to determine possible differences in positronium lifetime between cancer and normal cells, without the influence of water.

Obtained mean lifetime and intensity of o-Ps (Tab. 7.1) differed significantly between these cell lines freeze-dried in each medium. Differences were observed not only between normal and cancer cells but also between two lines of melanoma, which allows to assume that positronium can be applied to give information about the degree of malignancy of cancer. Nevertheless, depending on the medium, the same cell line has a various lifetime, and no correlation was observed, hence it depends on the freezing condition.

In order to understand these discrepancies and to investigate the cells viability as well as hydration influence on mean o-Ps lifetime, both rehydration and NMR spectroscopy experiments were performed.

Percentage of water mass loss describes dehydration of the sample during freeze-drying. The higher the value is, the more water evaporated during this process. The highest water loss was observed in cells freeze-dried in medium 3, containing only PBS w/o Ca^{2+} , Mg^{2+} , as it was expected since this buffer does not have cryoprotectant or water-binding properties. The lowest water loss was recorded in media containing D-Trehalose, which is due to the ability of this compound to bind water molecules. In case of melanocytes and WM115 melanoma cell line, this difference was higher than in WM266-4 melanoma cell line.

In case of viability after rehydration of cells, the highest one can be observed in the case of media 1 and 4 containing cryoprotectants. Cells freeze-dried in medium 3, demonstrated the highest water mass loss and the lowest viability after rehydration. Cells freeze-dried in medium 5, despite containing D-Trehalose also had very low viability, probably because the absence of cryoprotectants and higher water-binding properties result in ice crystals formation which damage cells structure. Freeze-drying in mediums 3 and 5 allowed the comparison between different hydration level, with similar viability values after rehydration of cells. In contrast, in mediums 1 and 4, the best cell survival rate can be observed.

1H – NMR spectroscopy was performed to determine the ratio of mobile protons (i.e. water molecules) to solid (immobilized) protons, and estimate hydration of freeze-dried cell lines. In case of all three cell lines, the highest level of hydration was observed in cells freeze-dried in medium 4, containing propylene glycol and D-Trehalose, with hydration ratio equal to 1.01(02), 0.90(02) and 0.98(02) for melanocytes, WM115 and WM266-4 melanoma cell lines, respectively. Medium 2 containing DMSO, also had a higher hydration level, while the lowest was observed in case of the third medium containing PBS only. These results are in agreement with determined mass loss during the freeze-dried procedure. Peculiarly interesting is, that cells in medium 5, containing only D-Trehalose manifest themselves by very low hydration level, despite water-binding properties of this compound, equal to 0.14(02), 0.14(02) and 0.21(02) for melanocytes, WM115 and WM266-4 melanoma

cell lines, respectively. If compared to mass loss differences between medium 4 and 5, such discrepancies were also observed, but not as high. Probably it can be related to the tightness of water-binding, described by higher values of the Lorentzian line width. The higher the FWHM, the more tightly water is bound, and in the most dehydrated samples, these parameters are the highest [130, 131].

Experiment with freeze-dried cells demonstrated that differences in positronium parameters were observed between all studied cell lines, normal and cancer ones, regardless of the freeze-drying medium and therefore water concentration or cell viability.

8.2.2 Positronium biomarker in living cells

Tests performed on living cultured cell lines in optimal conditions (without significant influence on cells viability), aimed to validate the hypothesis that positronium can be applied as a new cancer biomarker. Testing this was crucial for future in vivo applications, by coupling PALS with the J-PET scanner.

The most vital was to elaborate experiment protocol, which allows performing a stable measurement, without significant loss in cell viability, and achieving the highest possible number of cells per sample. The number of cells per sample was determined by the population doubling time, which is equal to around 93 h for melanocytes, 63 h and 34 h for WM115 and WM266-4 melanoma cell lines, respectively. Since the number of cell divisions for melanocytes was limited, these samples contained the least amount of cells in comparison to melanoma cell lines, while the initial cell number was similar for all lines. Proper conditions of the measurement were assessed based on the difference in the viability of cells before and after measurement. Low viability change in case of all three cell lines (Tab. 7.4), proves that suitable conditions, for measurements of living biological samples have been met.

In order to evaluate a protocol for PALS experiment, seven consecutive measurements with WM266-4 melanoma cell line were performed. Obtained values of mean positronium lifetime and intensity (Tab. 7.5) are in agreement within statistical uncertainties. Moreover, for a prolonged time of measurement, no significant differences were observed. Stability of obtained results proved that developed protocol for study is optimal. Hence, it can be applied to PALS study of living cell

cultures. Results of positronium parameters for all observed components (Tab. 7.6) are significantly different between each cell line. Determined values of mean ortho-positronium lifetime and intensity for living HEMa-LP melanocytes, WM115 and WM266-4 melanoma, are equal to 1.84(3) ns, 1.93(2) ns, 1.99(2) ns in lifetime and 12.7(1.8)%, 18.5(0.6)%, 17.0(0.8)% in intensity, respectively. Obtained results demonstrate that differences were observed not only between cancer and normal cells but also, between melanoma cell lines with different degree of malignancy. These results correspond to ones obtained for freeze-dried cells and indicate that even with the presence of water, differentiating between living normal and cancer cells is possible, with means of Positron Annihilation Spectroscopy. Hence, the application of positronium as a novel biomarker is valid.

There could be many factors responsible for observed discrepancies, such as free radicals level, primarily reactive oxygen species, which strongly influence mean o-Ps lifetime [132–134]. In case of chosen cells lines, ROS concentration among others is regulated by melanin, and its concentration can be related to observed differences.

Melanocytes and melanoma cell lines are pigmented. Differences in pigmentation can be observed (Fig. 7.9) depending on the melanin concentration, and were examined by means of EPR. The observed intensity of melanin signal in a WM266-4 cell line was negligible in comparison to standard (L-DOPA melanin), while for melanocytes and WM115 melanoma, melanin concentration was around six times higher than in WM266-4. In addition, between both pigmented cell lines differences were also observed, while higher melanin intensity was in melanocytes. In both pigmented cell lines components from both eumelanin and pheomelanin can be observed.

Determined melanin concentration per single cell is equal to 13.70(79) pg, 12.17(81) pg, 2.08(22) pg, for HEMa-LP melanocytes, WM115 and WM266-4 melanoma, respectively. Therefore, the highest concentration is in melanocytes and lowest in WM266-4 melanoma. As mentioned before, melanin is a natural, free radicals scavenger [121, 122], and therefore, can be accountable for observed differences in positronium lifetime, between studied cell lines. However, since free radicals activity is a complex issue, this hypothesis requires further investigation.

Chapter 9

Conclusions

In conclusion, results presented in this thesis confirm, that Positron Annihilation Lifetime Spectroscopy can detect differences in the molecular structure of cancer and normal cells and tissues. Obtained experiment outcomes, validate the working hypothesis that positronium can be applied as a novel biomarker in cancer diagnostics.

Based on the motivation for these studies, several main conclusion can be drawn:

1. It was shown, that PALS setup was calibrated and optimized, allowing studies of biological specimens, both fixed and living. It was done in a way, which ensures incorporation of analysis methods consistent with positronium imaging, by the J-PET scanner.
2. Elaborated protocol allowed to obtain stable and repeatable results, hence it can be applied for handling and PALS measurements of living cell cultures.
3. Results from studies of benign tumour, cardiac myxoma, demonstrated significant differences in both mean o-Ps lifetime and its production intensity, in comparison to normal adipose tissue. These differences are an order of magnitude larger, than ones observed between the same type of tissue from patient to patient, and between isolated cell culture and tumour specimen from the same patient.
4. Observation of positronium in freeze-dried cultured cell lines of malignant melanoma and normal melanocytes demonstrated that differences in mean o-Ps lifetime are observed between all studied cell lines, normal and cancer ones. Moreover, discrepancies are also observed between both melanoma cell

lines, with different degree of malignancy. Moreover, the differences in positronium mean lifetime are observed, in all cases, regardless of hydration level, due to different cryoprotectants and water-binding properties of freezing mediums.

5. Resulting positronium parameters in both living melanoma and melanocytes cell lines differ significantly for each line, not only between cancer and normal ones but also between two melanoma cell lines. These results correspond to ones obtained for freeze-dried cells. They indicate that even with the presence of water, distinguishing between living normal and cancer cells, as well as between cells with different degree of malignancy, is possible by means of Positron Annihilation Lifetime Spectroscopy.

Results described in this thesis proved that the application of positronium for cancer diagnostics is promising, yet further investigations are needed, in order to determine the factors responsible for observed differences.

Bibliography

- [1] Moskal P. et al. Patent No: US 9851456; PL 227658; PCT/EP2014/068374.
- [2] Moskal, P., Jasińska, B., Stepień, E. Bass, S. D. Positronium in medicine and biology. *Nat. Rev. Phys.* **1**, 527-529 (2019).
- [3] Jean, Y. C. Ache, H. J. Studies of Molecular Association in Biological Systems by Positron Annihilation Techniques. *J. Am. Chem. Soc.* **99**, 1623-1625 (1977).
- [4] Liu, G., Chen, H., Chakka, L., Gadzia, J. E. Jean, Y. C. Applications of positron annihilation to dermatology and skin cancer. *Physica Status Solidi (C) Current Topics in Solid State Physics* **4**, 3912-3915 (2007).
- [5] Jean, Y. C. et al. Applications of slow positrons to cancer research: Search for selectivity of positron annihilation to skin cancer. *Appl. Surf. Sci.* **252**, 3166-3171 (2006).
- [6] Jean, Y. C., Chen, H., Liu, G. Gadzia, J. E. Life science research using positron annihilation spectroscopy: UV-irradiated mouse skin. *Radiat. Phys. Chem.* **76**, 70-75 (2007).
- [7] Liu, G. et al. Further search for selectivity of positron annihilation in the skin and cancerous systems. *Appl. Surf. Sci.* **255**, 115-118 (2008).
- [8] Jasińska, B., ..., Kubicz, E. et al. Human tissues investigation using PALS technique. *Acta Phys. Pol. B* **48**, 1737-1747 (2017).
- [9] Jasiska, B., ..., Kubicz, E. et al. Human tissue investigations using PALS technique - Free radicals influence. *Acta Phys. Pol. A* **132**, 1556-1558 (2017).
- [10] Axpe, E. et al. Detection of atomic scale changes in the free volume void size of three-dimensional colorectal cancer cell culture using positron annihilation lifetime spectroscopy. *PLoS One* **9**, e83838 (2014).

- [11] Siles, S., Moya, G., Li, X. H., Kansy, J. Moser, P. Positron annihilation lifetime measurements in collagen biopolymer. *J. Radioanal. Nucl. Chem.* **240**, 529-530 (1999).
- [12] Hugenschmidt, C. Ceeh, H. The free volume in dried and H₂O-loaded biopolymers studied by positron lifetime measurements. *J. Phys. Chem. B* **118**, 9356-9360 (2014).
- [13] Sane, P. et al. Probing biomembranes with positrons. *J. Phys. Chem. B* **113**, 1810-1812 (2009).
- [14] Fong, C., Dong, A. W., Hill, A. J., Boyd, B. J. Drummond, C. J. Positron annihilation lifetime spectroscopy (PALS): A probe for molecular organisation in self-assembled biomimetic systems. *Phys. Chem. Chem. Phys.* **17**, 17527-17540 (2015).
- [15] Kubicz, E. et al. Studies of unicellular microorganisms *Saccharomyces cerevisiae* by means of positron annihilation lifetime spectroscopy. *Nukleonika* **60**, 749-753 (2015).
- [16] Moskal, P., ..., Kubicz, E. et al. A novel method for the line-of-response and time-of-flight reconstruction in TOF-PET detectors based on a library of synchronized model signals. *Nucl. Instruments Methods Phys. Res. Sect. A Accel. Spectrometers, Detect. Assoc. Equip.* **775**, 54-62 (2015).
- [17] Moskal, P., ..., Kubicz, E. et al. Time resolution of the plastic scintillator strips with matrix photomultiplier readout for J-PET tomograph. *Phys. Med. Biol.* **61**, 2025-2047 (2016).
- [18] Gajos, A., ..., Kubicz, E. et al. Trilateration-based reconstruction of ortho-positronium decays into three photons with the J-PET detector. *Nucl. Instruments Methods Phys. Res. Sect. A Accel. Spectrometers, Detect. Assoc. Equip.* **819**, 54-59 (2016).
- [19] Niedźwiecki, S., ..., Kubicz, E. et al. J-PET: A new technology for the whole-body PET imaging. *Acta Phys. Pol. B* **48**, 1567-1576 (2017).

- [20] Gajos, A., ..., Kubicz, E. et al. Feasibility Study of the Time Reversal Symmetry Tests in Decay of Metastable Positronium Atoms with the J-PET Detector. *Adv. High Energy Phys.* **2018**, 8271280 (2018).
- [21] Korcyl, G., ..., Kubicz, E. et al. Evaluation of Single-Chip, Real-Time Tomographic Data Processing on FPGA SoC Devices. *IEEE Trans. Med. Imaging* **37**, 2526-2535 (2018).
- [22] Kubicz, E. Potential for biomedical applications of positron annihilation lifetime spectroscopy (PALS). *AIP Conference Proceedings* **2182**, 050004 (2019).
- [23] Kamińska, D., ..., Kubicz, E. et al. A feasibility study of ortho-positronium decays measurement with the J-PET scanner based on plastic scintillators. *Eur. Phys. J. C* **76**, 445 (2016).
- [24] Moskal, P., ..., Kubicz, E. et al. Feasibility study of the positronium imaging with the J-PET tomograph. *Phys. Med. Biol.* **64**, 055017 (2019).
- [25] Moskal, P., ..., Kubicz, E. et al. Performance assessment of the 2 gamma positronium imaging with the total-body PET scanners. *EJNMMI Physics* **7**, 44 (2020).
- [26] Dulski, K., ..., Kubicz, E. et al. Commissioning of the J-PET detector in view of the positron annihilation lifetime spectroscopy. *Hyperfine Interact.* **239**, 40 (2018).
- [27] Charlton, M. Humberston, J. W. Introduction. in *Positron Physics*. Cambridge University Press, (2009).
- [28] Tao, S. J. The formation of positronium in molecular substances. *Appl. Phys.* **10**, 67-79 (1976).
- [29] Stepanov, S. V. Byakov, V. M. Electric field effect on positronium formation in liquids. *J. Chem. Phys.* **116**, 6178-6195 (2002).
- [30] Stepanov, S. V. et al. Positronium in a liquid phase: Formation, bubble state and chemical reactions. *Adv. Phys. Chem.* **116**, 431962 (2012).

- [31] Dryzek, J. Horodek, P. The distribution of slowing-down times of positrons emitted from ^{22}Na and $^{68}\text{Ge}/^{68}\text{Ga}$ isotopes into metals. *Mater. Sci. Forum* **666**, 10-14 (2011).
- [32] Procházka, I. Positron Annihilation Spectroscopy. *Mat. Struc.* **8**, 55-60 (2001).
- [33] Goworek, T. Positronium as a probe of small free volumes in crystals, polymers and porous media. *Ann. UMCS, Chem.* **69**, 1-110 (2014).
- [34] Cassidy, D. B. Experimental progress in positronium laser physics. *Eur. Phys. J. D* **72**, 53 (2018).
- [35] Consolati, G. Quasso, F. A positron annihilation study on the hydration of cement pastes. *Mater. Chem. Phys.* **101**, 264-268 (2007).
- [36] Vértés, A., Nagy, S., Klencsár, Z., Lovas, R. G. Rösch, F. Positron Annihilation Spectroscopies. in *Handbook of Nuclear Chemistry*. Springer US, (2011).
- [37] Consolati, G. Quasso, F. Ortho - para conversion of positronium in some rare-earth ion aqueous solutions. *Can. J. Phys.* **67**, 76-78 (1989).
- [38] Zgardzinska, B., Bialko, W. Jasinska, B. Ortho-para spin conversion of Ps by paramagnetic O₂ dissolved in organic compounds. *Nukleonika* **60**, 801-804 (2015).
- [39] Stepanov, P. S. et al. Interaction of positronium with dissolved oxygen in liquids. *Phys. Chem. Chem. Phys.* **22**, 5123-5131 (2020).
- [40] Tao, S. J. Positronium annihilation in molecular substances. *J. Chem. Phys.* **56**, 5499-5510 (1972).
- [41] Eldrup, M., Lightbody, D. Sherwood, J. N. The temperature dependence of positron lifetimes in solid pivalic acid. *Chem. Phys.* **63**, 51-58 (1981).
- [42] Jean, Y. C. Deng, Q. Direct measurement of free-volume hole distributions in polymers by using a positronium probe. *J. Polym. Sci. Part B Polym. Phys.* **30**, 1359-1364 (1992).
- [43] Zgardzińska, B. Can Tao-Eldrup Model Be Used at Short o-Ps Lifetime? *Acta Phys. Pol. A* **125**, 700-701 (2014).

- [44] Baba, A. I. Cătoi, C. Comparative Oncology. in *Comparative Oncology*, The Publishing House of the Romanian Academy, (2007).
- [45] Wild, C. P., Weiderpass, E. Stewart, B. W. World cancer report 2020. World Health Organization, *International Agency for Research on Cancer* (2020).
- [46] Grant, E. J. et al. Solid Cancer Incidence among the Life Span Study of Atomic Bomb Survivors: 1958-2009. *Radiat. Res.* **187**, 513-537 (2017).
- [47] Leuraud, K. et al. Ionising radiation and risk of death from leukaemia and lymphoma in radiation-monitored workers (INWORKS): an international cohort study. *The Lancet Haematology* **2**, e276-e281 (2015).
- [48] Arnold, M. et al. Global burden of cutaneous melanoma attributable to ultraviolet radiation in 2012. *Int. J. Cancer* **143**, 1305-1314 (2018).
- [49] Stanaway, J. D. et al. Global, regional, and national comparative risk assessment of 84 behavioural, environmental and occupational, and metabolic risks or clusters of risks for 195 countries and territories, 1990-2017: A systematic analysis for the Global Burden of Disease Study 2017. *Lancet* **392**, 1923-1994 (2018).
- [50] de Martel, C., Georges, D., Bray, F., Ferlay, J. Clifford, G. M. Global burden of cancer attributable to infections in 2018: a worldwide incidence analysis. *The Lancet Global Health* **8**, e180-e190 (2020).
- [51] Butel, J. S. Viral carcinogenesis: Revelation of molecular mechanisms and etiology of human disease. *Carcinogenesis* **21**, 405-426 (2000).
- [52] Muller, P. A. J. Vousden, K. H. P53 mutations in cancer. *Nature Cell Biology* **15**, 2-8 (2013).
- [53] Harding, S. M., Bristow, R. G. Harrington, L. Genomic Stability and DNA Repair. in *The Basic Science of Oncology*, 5th Ed. McGraw-Hill International Editions, (2013).

- [54] Bizzarri, M., Cucina, A., Conti, F. D'Anselmi, F. Beyond the oncogene paradigm: Understanding complexity in cancerogenesis. *Acta Biotheor.* **56**, 173-196 (2008).
- [55] King, R. J. B. Robins, M. W. Oncogenes, tumour suppressor genes and viruses. in *Cancer Biology*, 3rd Ed. Pearson Education, (2006).
- [56] Pezzella, F., Tavassoli, M., Kerr, D. J. How the cancer cell works. in *Oxford Textbook of Cancer Biology*, Oxford University Press, (2019).
- [57] Hanahan, D. Weinberg, R. A. The hallmarks of cancer. *Cell* **100**, 57-70 (2000).
- [58] Shay, J. W., Zou, Y., Hiyama, E. Wright, W. E. Telomerase and cancer. *Human Molecular Genetics* **10**, 677-685 (2001).
- [59] Prevarskaya, N., Skryma, R. Shuba, Y. Ion channels and the hallmarks of cancer. *Trends Mol. Med.* **16**, 107-121 (2010).
- [60] Pavlova, N. N. Thompson, C. B. The Emerging Hallmarks of Cancer Metabolism. *Cell Metab.* **23**, 27-47 (2016).
- [61] Cavallo, F., De Giovanni, C., Nanni, P., Forni, G. Lollini, P. L. 2011: The immune hallmarks of cancer. *Cancer Immunol. Immunother.* **60**, 319-326 (2011).
- [62] Coussens, L. M. Werb, Z. Inflammation and cancer. *Nature* **420**, 860-867 (2002).
- [63] Hanahan, D. Weinberg, R. A. Hallmarks of cancer: The next generation. *Cell* **144**, 646-674 (2011).
- [64] Pickup, M. W., Mouw, J. K. Weaver, V. M. The extracellular matrix modulates the hallmarks of cancer. *EMBO Rep.* **15**, 1243-1253 (2014).
- [65] Pietras, K. Östman, A. Hallmarks of cancer: Interactions with the tumor stroma. *Exp. Cell Res.* **316**, 1324-1331 (2010).
- [66] Han, L., Lam, E. W. F. Sun, Y. Extracellular vesicles in the tumor microenvironment: Old stories, but new tales. *Mol. Cancer* **18**, 59 (2019).
- [67] Baba, A. I. Cătoi, C. Tumour cell morphology. in *Comparative Oncology*, The Publishing House of the Romanian Academy, (2007).

- [68] Singh, K. K. Costello, L. C. The Role of Mitochondrial ROS in Carcinogenesis. in *Mitochondria and Cancer*, Springer New York, (2009).
- [69] Liberti, M. V. Locasale, J. W. The Warburg Effect: How Does it Benefit Cancer Cells? *Trends Biochem. Sci.* **41**, 211-218 (2016).
- [70] Moloney, J. N. Cotter, T. G. ROS signalling in the biology of cancer. *Semin. Cell Dev. Biol.* **80**, 50-64 (2018).
- [71] Prasad, S., Gupta, S. C. Tyagi, A. K. Reactive oxygen species (ROS) and cancer: Role of antioxidative nutraceuticals. *Cancer Lett.* **387**, 95-105 (2017).
- [72] Sabharwal, S. S. Schumacker, P. T. Mitochondrial ROS in cancer: Initiators, amplifiers or an Achilles' heel? *Nat. Rev. Cancer* **14**, 709-721 (2014).
- [73] Benhar, M., Engelberg, D. Levitzki, A. ROS, stress-activated kinases and stress signaling in cancer. *EMBO Reports* **3**, 420-425 (2002).
- [74] Spitz, D. R., Dornfeld, K. J., Krishnan, K. Gius, D. Oxidative stress and tumor response. in *Oxidative Stress in Cancer Biology and Therapy*, Springer New York, (2011).
- [75] Berko, S., Zuchelli, A. J. Free-Radical Quenching of Positron Lifetimes. *Phys. Rev.* **103**, 1905-1905 (1956).
- [76] Rzepka, Z., Buszman, E., Beberok, A. Wrześniok, D. From tyrosine to melanin: Signaling pathways and factors regulating melanogenesis. *Postepy Hig. Med. Dosw.* **70**, 695-708 (2016).
- [77] Bandarchi, B., Ma, L., Navab, R., Seth, A. Rasty, G. From melanocyte to metastatic malignant melanoma. *Dermatol. Res. Pract.* **2010**, 583748 (2010).
- [78] <http://smart.servier.com/>
- [79] Cichorek, M., Wachulska, M., Stasiewicz, A. Tymińska, A. Skin melanocytes: Biology and development. *Postep. Dermatologii i Alergol.* **30**, 30-41 (2013).
- [80] Videira, I. F. dos S., Moura, D. F. L. Magina, S. Mechanisms regulating melanogenesis*. *Anais Brasileiros de Dermatologia* **88**, 76-83 (2013).

- [81] Bertolotto, C. Melanoma: From Melanocyte to Genetic Alterations and Clinical Options. *Scientifica* **2013**, 635203 (2013).
- [82] Slominski, A. et al. Molecular pathology of malignant melanoma. *Am. J. Clin. Pathol.* **110**, 788-794 (1998).
- [83] Wróbel, S., Przybyło, M. Stępień, E. The Clinical Trial Landscape for Melanoma Therapies. *J. Clin. Med.* **8**, 368 (2019).
- [84] Dickson, P. V. Gershenwald, J. E. Staging and prognosis of cutaneous melanoma. *Surg. Oncol. Clin. N. Am.* **20**, 1-17 (2011).
- [85] Freedberg, I. M., Eisen, A. Z., Wolff, K., Austen, K. F., Goldsmith, L. A. Katz, S. Neoplasms: Cutaneous Melanoma. in *Fitzpatrick's Dermatology In General Medicine*, 6th Ed. McGraw-Hill (2003).
- [86] Acebo, E., Val-Bernal, J. F., Gómez-Román, J. J. Revuelta, J. M. Clinicopathologic study and DNA analysis of 37 cardiac myxomas: A 28-year experience. *Chest* **123**, 1379-1385 (2003).
- [87] Amano, J. et al. Cardiac myxoma: its origin and tumor characteristics. *Ann. Thorac. Cardiovasc. Surg.* **9**, 215-221 (2003).
- [88] Burke, A. P. Virmani, R. Cardiac myxoma: A clinicopathologic study. *American Journal of Clinical Pathology* **100**, 671-680 (1993).
- [89] Perek, B. et al. Early and long-term outcome of surgery for cardiac myxoma: Experience of a single cardiac surgical centre. *Kardiol. Pol.* **69**, 558-564 (2011).
- [90] Sakamoto, H. et al. Production of endothelin-1 and big endothelin-1 by human cardiac myxoma cells - Implications for the origin of myxomas. *Circ. J.* **68**, 1230-1232 (2004).
- [91] Travis, W. D., Brambilla, E., Müller-Hermelink, H. K. Harris, C. C. Pathology Genetics of Tumours of the Lung, Pleura, Thymus and Heart. *The International Agency for Research on Cancer. IARC/Press* (2004).
- [92] Reynen, K. Cardiac myxomas. *New England Journal of Medicine* **333**, 1610-1617 (1995).

- [93] Carney, J. A. Ferreiro, J. A. The epithelioid blue nevus: A multicentric familial tumor with important associations, including cardiac myxoma and psammomatous melanotic schwannoma. *American Journal of Surgical Pathology* **20**, 259-272 (1996).
- [94] Online Mendelian Inheritance in Man (OMIM) Carney Complex, type 1; CNC1 -160980.
- [95] Stratakis, C. A., Kirschner, L. S. Carney, J. A. Clinical and Molecular Features of the Carney Complex: Diagnostic Criteria and Recommendations for Patient Evaluation. *J. Clin. Endocrinol. Metab.* **86**, 4041-4046 (2001).
- [96] Stępień, E. et al. A new clonal chromosomal aberration (47, XY, +21) in atrial myxoma from an elderly male patient. *Cardiogenetics* **2**, 3 (2012).
- [97] Kasugai, T. et al. Sequential Malignant Transformation of Cardiac Myxoma. *Pathology International* **40**, 687-692 (1990).
- [98] Pinede, L., Duhaut, P. Loire, R. Clinical presentation of left atrial cardiac myxoma: A series of 112 consecutive cases. *Medicine* **80**, 159-172 (2001).
- [99] Wang, H., Li, Q., Xue, M., Zhao, P. Cui, J. Cardiac myxoma: A rare case series of 3 patients and a literature review. *J. Ultrasound Med.* **36**, 2361-2366 (2017).
- [100] Shinfeld, A., Katsumata, T. Westaby, S. Recurrent cardiac myxoma: Seeding or multifocal disease? *Ann. Thorac. Surg.* **66**, 285-288 (1998).
- [101] Dulski, K., ..., Kubicz, E. et al. Analysis procedure of the positronium lifetime spectra for the J-PET detector. *Acta Phys. Pol. A* **132**, 1637-1640 (2017).
- [102] National Nuclear Data Center, [http://http://www.nndc.bnl.gov](http://www.nndc.bnl.gov), accessed: 01.02.2020
- [103] Dulski, K. Assembly and calibration of apparatus for Positron Annihilation Lifetime Spectroscopy. Master Thesis (2016).
- [104] Jasińska, B., ..., Kubicz, E. et al. Determination of the 3γ fraction from positron annihilation in mesoporous materials for symmetry violation experiment with J-PET scanner. *Acta Phys. Pol. B* **47**, 453-460 (2016).

- [105] Bednarski, T. et al. Calibration of photomultipliers gain used in the J-PET detector. *Bio-Algorithms and Med-Systems* **10**, 13-17 (2014).
- [106] Tuomisto, F. Makkonen, I. Defect identification in semiconductors with positron annihilation: Experiment and theory. *Rev. Mod. Phys.* **85**, 1583-1631 (2013).
- [107] Sen, P. Sen, C. Effect of doping on positron lifetime in Si crystals. *Journal of Physics C: Solid State Physics* **7**, 2776-2780 (1974).
- [108] Dorikens, M., Dauwe, C. Dorikens-Vanpraet, L. Positron lifetime measurements in n- and p-type silicon. *Appl. Phys.* **4**, 271-272 (1974).
- [109] Fieschi, R., Gainotti, A., Ghezzi, C. Manfredi, M. Positron annihilation in semiconductors. *Physical Review* **175**, 383-388 (1968).
- [110] Lee, C. Y. Positron Annihilation Study of Vacancy Type Defects in Ti, Si, and BaSrFBr:Eu. *Appl. Sci. Conver. Technol.* **25**, 85-87 (2016).
- [111] Surman, M. et al. Human melanoma-derived ectosomes are enriched with specific glycan epitopes. *Life Sci.* **207**, 395-411 (2018).
- [112] Herlyn, M. et al. Primary melanoma cells of the vertical growth phase: similarities to metastatic cells. *J Natl Cancer Inst* **74**, 283-289 (1985).
- [113] Kolasińska, E., Przybyło, M., Janik, M. Lityńska, A. Towards understanding the role of sialylation in melanoma progression. *Acta Biochim. Pol.* **63**, 533-541 (2016).
- [114] Heo, Y. S. et al. 'Universal' vitrification of cells by ultra-fast cooling. *Technology* **03**, 64-71 (2015).
- [115] Natan, D., Nagler, A. Arav, A. Freeze-drying of mononuclear cells derived from umbilical cord blood followed by colony formation. *PLoS One* **4**, e5240 (2009).
- [116] Čechová, K. et al. Microstructural free volume and dynamics of cryoprotective DMSO-water mixtures at low DMSO concentration. *RSC Adv.* **9**, 34299-34310 (2019).

- [117] Jerie, K., Baranowski, A., Gliński, J. Jeżowska-Trzebiatowska, B. Positron Annihilation in and Compressibility of Water-Organic Solutions. The System Water-Pyridine. *Acta Phys. Pol. A* **82**, 471-479 (1991).
- [118] Kim, M. S., Lee, S. T., Lim, J. M. Gong, S. P. Medium composition for effective slow freezing of embryonic cell lines derived from marine medaka (*Oryzias dancena*). *Cytotechnology* **68**, 9-17 (2016).
- [119] Kilburn, D. et al. Organization and mobility of water in amorphous and crystalline trehalose. *Nat. Mater.* **5**, 632-635 (2006).
- [120] Derbyshire, W. et al. Fitting of the beat pattern observed in NMR free-induction decay signals of concentrated carbohydrate-water solutions. *J. Magn. Reson.* **168**, 278-283 (2004).
- [121] Rózanowska, M., Sarna, T., Land, E. J. Truscott, T. G. Free radical scavenging properties of melanin interaction of eu- and pheo-melanin models with reducing and oxidising radicals. *Free Radical Biology and Medicine* **26**, 518-525 (1999).
- [122] Herrling, T., Jung, K. Fuchs, J. The role of melanin as protector against free radicals in skin and its role as free radical indicator in hair. *Spectrochim. Acta - Part A Mol. Biomol. Spectrosc.* **69**, 1429-1435 (2008).
- [123] Wold, L. E. Lie, J. T. Cardiac myxomas. A clinicopathologic profile. *American Journal of Pathology* **101**, 219-240 (1980).
- [124] Yang, S. H., Ballmann, C. Quarles, C. A. Positron Spectroscopy Investigation of Normal Brain Section and Brain Section with Glioma Derived from a Rat Glioma Model. *AIP Conf. Proc.* **1099**, 948-951 (2009).
- [125] Blaschuk, O. W. Rowlands, T. M. Cadherins as modulators of angiogenesis and the structural integrity of blood vessels. *Cancer Metastasis Rev.* **19**, 1-5 (2000).
- [126] Vestweber, D. VE-cadherin: The major endothelial adhesion molecule controlling cellular junctions and blood vessel formation. *Arterioscler. Thromb. Vasc. Biol.* **28**, 223-232 (2008).

- [127] Liskay, L. et al. Positronium Interactions in Synthetic Zeolites: Effect of Adsorbed Water. *Mater. Sci. Forum* **363-365**, 377-379 (2001).
- [128] McGervey, J. DeBenedetti, S. Chemical reactions of positronium in aqueous solutions. *Phys. Rev.* **114**, 495-496 (1959).
- [129] Gustafson, D. R. Positronium Formation in Muscle: An Investigation of the Structure of Cell Water. *Biophys. J.* **10**, 316-322 (1970).
- [130] Nizioł, J. et al. Hydration effect on solid DNA-didecyldimethylammonium chloride complexes measured using ^1H -nuclear magnetic resonance spectroscopy. *J. Appl. Phys.* **114**, 1-8 (2013).
- [131] Lüsse, S. Arnold, K. Water binding of polysaccharides - NMR and ESR studies. *Macromolecules* **31**, 6891-6897 (1998).
- [132] Karbowski, A., Fedus, K., Służewski, K., Bruzdowska, J. Karwasz, G. Positronium formation in organic liquids. *Acta Phys. Pol. A* **132**, 1466-1469 (2017).
- [133] Consolati, G. Quasso, F. Positronium-oxygen interactions in polytrimethylsilylpropine membranes. *Applied Physics B: Lasers and Optics* **66**, 371-376 (1998).
- [134] Karbowski, A., Fedus, K. Karwasz, G. Positronium formation in molecular gases - From experiment to modeling. *Acta Phys. Pol. B* **48**, 1593-1599 (2017).